CRUSTAL STRUCTURE EVOLUTION IN MAGADI AREA, KENYA, USING 3D SEISMIC TOMOGRAPHY

BY:

BENSON NYAMBOGA ONGUSO

I56/70110/2011

A DISSERTATION SUBMITTED IN PARTIAL FULFILLMENT OF THE REQUIREMENTS FOR THE DEGREE OF MASTER OF SCIENCE IN GEOLOGY OF THE UNIVERSITY OF NAIROBI

DECLARATION

This is my creative effort and has not been presented for a degree in any other university.

Benson Nyamboga Onguso

I56/ 70110 /2011

Signature ……Date……

This study has been presented for examination with my approval as a University Supervisor

Professor Justus Obiko Barongo

Professor, Department of Geology, CBPS, University of Nairobi

Signature …… Date ……..

This study has been presented for examination with my approval as a University Supervisor

Ms. Gladys Karegi Kianji

Lecturer, Department of Geology, CBPS, University of Nairobi

Signature …….. Date…….

DEDICATION

I dedicate this dissertation to the Almighty God for His blessings and His Grace which enabled me carry out this work.

AKNOWLEDGEMENT

I am thankful to God for His strength and support throughout the period of this work. I am grateful to my supervisors, Prof. Justus Barongo and Ms. Gladys Kianji who supported this work by all means possible. I wish to also thank the technical staff in the Department of Geology for their support. I thank my fellow postgraduate Master of Science students and colleagues. I also wish to acknowledge my dear parents for their support and encouragement. Finally, I extend my gratitude to Geology Department and the University of Nairobi for offering me the University of Nairobi scholarship. The Department of Geology also provided conducive study environment and the necessary support to complete this work.

ABSTRACT

In this study, the seismicity, hypocenter distribution, Magadi crustal structure evolution and short term crustal structure changes were explored in order to examine its crustal structure changes using refraction seismic method. Short term crustal structure changes in Magadi have not been studied earlier on. Also, update on seismicity of Magadi area in order to incorporate new events has not been done. The new events were located and relocated using sub sets of seismic data from crafti project for period January 2013 up to December 2014, supplemented by the existing seismic data sub set recorded by Ibs-von Seht et al. for period November 1997 up to June 1998. The combined events were visualized in form of epicenters and hypocenters using GIS and tomo3d softwares respectively. Travel times data was extracted from the two data sub sets. These travel times were used to develop 1D inversion model for Magadi area using velest routine, a seismic technique, in seisan. The 1D inversion model was used as input into 3D inversion process using seismic tomography technique (tomo3d) software package in order to aid in understanding the Magadi crustal structure evolution and short term crustal structure changes.

The surface visualization of the combined events revealed clustering of events on the north eastern part of Lake Magadi unlike the northern, north western, western, south western, southern, south eastern and eastern parts of this lake where no clustering of events was evident. These events had a modal maximum depth of 27 kilometers with uneven distribution of hypocenters. The underground components of the examined structures exposed an increment of velocity with constant velocity in between the increasing velocities, except at about 3 kilometers to about 7 kilometers of the final 1D inversion model for this work. Here, there was a decline instead of increment of velocity believed to be a small magma chamber or zone of partial melt due to small magma injection.

The final 3D inversion results revealed an oval shaped high velocity zone (6.5 to about 9.0 kilometers per second) representing mafic intrusive body. This high velocity intrusive body is located at 35.6^0 E to 36.2^0 E and 2.1^0 S to 1.7^0 S and at depths of about 3 kilometers to about 15 kilometers. It later broke, changed or deformed into three smaller oval shaped high velocity

bodies (6.5 to about 8.0 kilometers per second) with a low velocity zone (believed to be small magma chamber, or zone of partial melt due to the intruding magma) in between them with velocity value of about 3.0 kilometers per second. These oval bodies are located at 36^0 E to 36.6^0 E and depths of about 3 kilometers to about 16 kilometers. The low velocity zones have values of about 3 kilometers per second up to a maximum of 4 kilometers per second unlike the smaller high velocity oval bodies whose velocity values range from about 6.5 kilometers per second to 8 kilometers per second. The oval shapes change to globular or sausage-like shapes as one moves north to south. These changes stand for varying geometry of the intruding magma conduits.

Therefore, in summary, the study concludes that there exist high velocity zones (6.5 to 9.0 kilometers per second) within the Magadi area through which small pockets of magma has intruded forming low velocity zones (about 3 kilometers per second). These low velocity zones are fed by deep seated magma repository chamber. This repository chamber is located at the bottom of Magadi crust (about 47 kilometers deep). It extends to the top of the mantle layer. This supports the fact that Magadi is undergoing continuous crustal structure changes through small scale magmatic and tectonic movements. The faulting process occurring in this area has played a key role in forming conduits through which magma moves upwards through the Magadi crust. This confirms continuous short term small crustal structure changes of the Magadi basin through small magmatic intrusion and tectonism within the Magadi crust.

.

Keywords: L. Magadi, Seismicity, Epicenters, Hypocenters, Inversion and Seismic Tomography

TABLE OF CONTENTS

List of Figures

List of Tables

Abbreviations and Definitions

EARV-East Africa Rift Valley

SRVL-Southern Rift Valley Lakes

KRISP85-Kenya Rift International Seismological Program 1985

KRISP94-Kenya Rift International Seismological Program 1994

E-W -East to West

NW-SE -North-west to South-east

N-S -North to South

Kms -Kilometers

Q GIS -Quontum Geographical Information System software

Hz -hertz

DOS -Disk Operating System

RMS -Root Mean Square

P-Primary wave

S-Secondary wave

Nsp-number of phases

Hyp -hypocenter

GIS -Geographical information System

1D-is a representation of the earth in one direction only either x only, y only or z (depth) only.

2D-is a representation of the earth in two directions only either x and y, x and z or y and z (depth).

3D-is a representation of the earth in three directions, that is, x, y and z (depth).

FMM-Fast Marching Method

Km^2 – kilometer squared

V_0-velocity at initial layer of crust near earth-surface

x-distance

t-time

X_c-critical distance

i_c-critical angle

X_{cr}-crossover distance

CD-change directory

Dir-directory

MS-DOS-Microsoft Disk Operated System

LVL-Low Velocity Layer

AVEL-Averaged Velocity

V_p-Primary-wave velocity

V_s-Secondary-wave velocity

KRISP-Kenya Rift International Seismological Program

GMT-Generic Mapping Tool

Crustal model-is a representation of the causative factors of the subsurface for the observed data.

Crustal structure-it is layering in spherical shells like an onion with varying chemical and rheological property.

Resonance-it is the reinforcement or prolongation of energy by reflection from a surface (interface).

Geology-it means the study of rocks.

Seismology- refers to the study of natural waves propagating through the surface and subsurface of the earth.

Epicenter- means the point on the surface of the earth directly above the origin of an earthquake.

Hypocenter- means the origin of an earthquake.

Receiver- refers to a device which is used to record earthquakes.

Lithology-it is the description of the physical characteristics of a rock unit.

Quarternary- refers to the geological time scale period which ranges from 2.6 – 0.0 million years.

Holocene- refers to the geological time scale epoch which ranges from 0.01 – 0.0 million years.

Riverines-are vegetations along the bank of river channel (course) from river source to its end.

Nomads-are people who move from one place to another in search of water and grass for their animals.

Physiography-is the systematic description of nature (landforms and processes involved) in general.

MAKEREA-is a command in Seisan which assists in automatic production of both REA and WAV subdirectories.

WAV-is waveforms subdirectory.

REA-is support subdirectory in Seisan.

AUTOREG-is a command in Seisan which automatically registers waveforms.

DIRF-is a command in Seisan which lists waveforms.

MULTPLT-is a command in Seisan which aids in displaying a large number of waveforms.

LOCAT-is a command in Seisan software which helps in locating events.

Geophone- it is the device which is used to record earthquakes on the earth surface.

Ray-path-is a route followed by propagating seismic energy in the subsurface.

Inversion model-is an image of the subsurface which displays the causal factors for the observed data.

Residuals-it is the difference between the observed and predicted (calculated) data.

Objective function-it is the function which characterizes the data misfits in geophysical inversion.

Evolution -changes that the crustal structure has undergone within a given period of time.

1. INTRODUCTION

1.1 Background Information

Earthquakes have been occurring and have caused destruction for a long time in the history of mankind. Such destruction includes damage to property and deaths. Good example of destructive earthquakes is the one which occurred in China in January 23rd, 1556. It killed 830,000 people as per the historical records. Such earthquake occurrences are huge risks to the lives of people. Scientists started studying the causes of such earthquakes and places where they are likely to happen. These earthquake studies once initiated were later referred to as seismology. From the time when it was initiated, great strides have been achieved in subsurface seismic tomography, (Bath, 1979, Agnew, 2002). The latest advancement is the use of seismic tomography to understand the subsurface structures. All these observations, however, carry information not only on the crustal structure, but also on the in-homogeneity along the seismic rays. The aim of seismic tomography is to determine this velocity contrast distribution in a region spanned by the different sources and receivers. First pioneered in the mid 1970s, (Aki, 1974), originally under the name of "inversion", one dimensional seismic inversion is nowadays a well recognized procedure used in both comprehensive study of the shallowest crust and in structural modeling of the earth as input data for "three dimensional inversion". Seismic tomography technique was approved in the 1980s from medical investigation along with the estimated solvers for hefty matrices used in the different forms of medical tomography, for example, X-ray imaging and Nuclear Magnetic Resonance (Aki, 1974). The two kinds of tomography, seismic and medical, are often considered to be almost identical due to a very similar mathematical formulation. However, the two methods are, in fact, very different in one basic aspect. Whereas the absorption of, for example, X-rays in radiological imaging has the advantage of being a linear problem, in the sense that the rays remain straight lines and the absorption does not depend on the direction of spread, seismic tomography is highly non-linear. In this study, times were used to calculate the seismic velocities in the initial and final models. The linearity effect was achieved through approximate estimations of the outputs of inversion processes through linearized Algorithm. The coupling between travel time anomalies and seismic velocities depended on the seismic velocity structure.

1.2 Problem statement

Research works has been carried out in Magadi area focusing on seismic analysis on long term crustal structure changes beneath the Magadi crust. Nevertheless, less has been done on analysis on comparison of the crustal structure changes occurring to the Magadi crust over short term intervals to decipher the short term crustal structure changes. Research need to now aim at short term crustal structure changes monitoring to establish the short term crustal dynamics and relate them to rifting process. Earlier studies have shown dynamic long term crustal changes in Lake Magadi, southern Kenya rift (Ibs-von Seht et al., 2001). The long term crustal structure studies around Lake Magadi were intended to characterize the crustal structure using 3D seismic tomography (Ibs-von Seht et al., 2001); but their short term changes, particularly short term crustal structure changes within a period of less than four years in the area have not been investigated. In Lake Magadi region, the occurrence of fluid-packed elevated fractures in the shallow crust was suggested by Ibs-von Seht et al. (2001) by means of seismic technique. This was deduced from the low velocity anomaly encountered in the lower part of Lake Magadi including surface manifestations via hot springs. Also, active seismicity of Lake Magadi area has been suggested by Ibs-von seht et al. (2001) and Kianji (2001) by means of seismic techniques. But the continuous update on seismicity in the area has not been done too. Hence, this study utilized the use of 3D seismic tomography technique to understand the short term crustal structure changes for four years (1997, 1998, 2013 and 2014) around Lake Magadi region. The study was based on available data sub sets for 1997, 1998, 2013 and 2014 which was recorded due to the rifting activity which is on-going both in Magadi and Natron areas. In addition, it also worked on seismicity of the area by updating previous seismicity works with a view of incorporating the new events.

1.3 Scope and Location

The study determined the crustal structure changes beneath Magadi area. This was possible by use of the subsurface travel-time parameters. Observed travel-times are inverted and then final velocity compared. The slices were along N-S and then E-W at 2.1^0 S due to small area of overlap between Ibs-von Seht et al., (2001) and my current investigations compared to work by Roecker (2017). Magadi trough, (fig. 1.1), is located about 120 km to the south of Nairobi city. It falls within the Tertiary Rift of Kenya which is part of the larger East Africa Rift Valley (EARV).

The region, (fig. 1.1), is bounded by latitudes 1^0 40'S and 2^0 10'S and longitudes 36^0 00'E and 36^0 30'E. It is part of the active continental rift evidenced by the recent volcanic activities in the lower region within the country's Gregory Fissure which begins from Lake Turkana and stretches southwards to Lakes Natron-Magadi trench in the northern part of Tanzania.

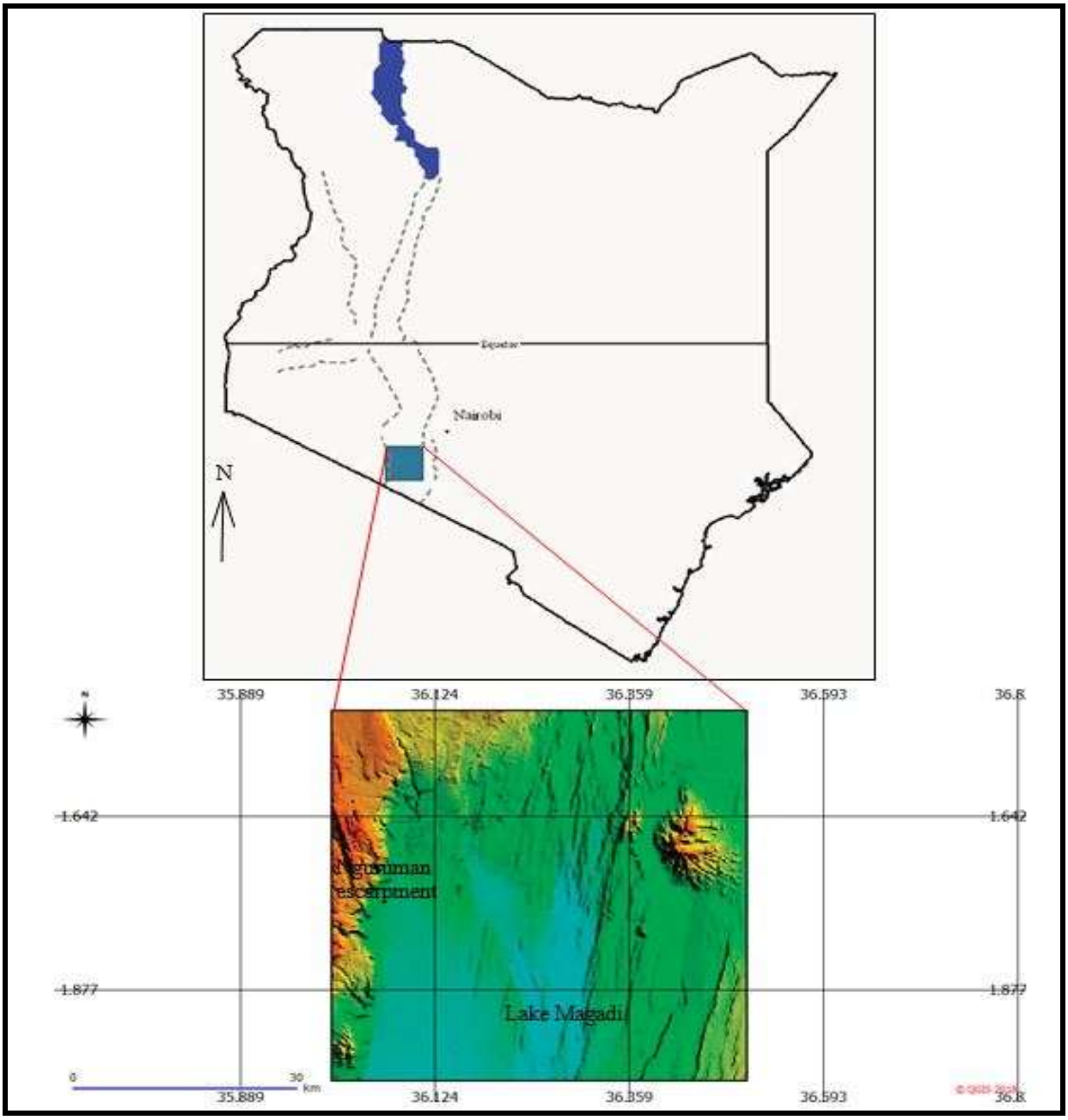

Figure 1.1: Location of Magadi area

1.4 General setting

The general setting entails the following: (1) physical setting, (2) climate, (3) vegetation, (4) land use and land resources, (5) physiography and drainage, (6) soils, and (7) surface and groundwater resources. In order to expound on the general setting, its sub-sections have been discussed and given below as follows:

1.4.1 Physical setting

Lake Magadi area is one of the Southern Rift Valley Lakes (SRVL) existing in the lower EARV rift. It is a salty lake unlike Lake Naivasha which is a fresh lake farther north. The case of the latter is explained by the fact that its location is at the apex of the rift valley floor, about 1885 m above sea level provoking the outflow of the groundwater. Consequently, the outflow refreshes this fresh water lake and prevents accumulation of salts unlike Lake Magadi where the opposite is true. In Magadi, the lake has an elevation of about 550m above sea level and acts as an absolute sink of water and solutes. This is evident as manifested by the thick soda deposits on most of the lake surface. The surface water inflow into Lake Magadi is limited and the main recharge comes from a series of springs. Some of the perennial rivers originate from the western flanks of the rift valley.

1.4.2 Climate

Magadi area has a hot and dry climate. This is supported by the fact that it receives high day-time temperatures, (fig. 1.2), low rainfalls, (fig. 1.3) and cool nights. Nevertheless, it is pleasant along the plains stretching to the foot of the mountains where humidity is low. Much of the rain is received during the rainy seasons between March and April and also in December. It is one of the deepest rift valley bottoms. It is semi arid with average rainfall of 470 mm per year. The open water evaporation is in the order of 1700-2500 mm per year. In order to replenish water deficit, the lake is nourished by groundwater. The area experiences strong winds mainly from east and north east. Very little rainfall, elevated daily temperatures and the character of the prevailing lava substratum combine to produce a semi-arid to arid landscape.

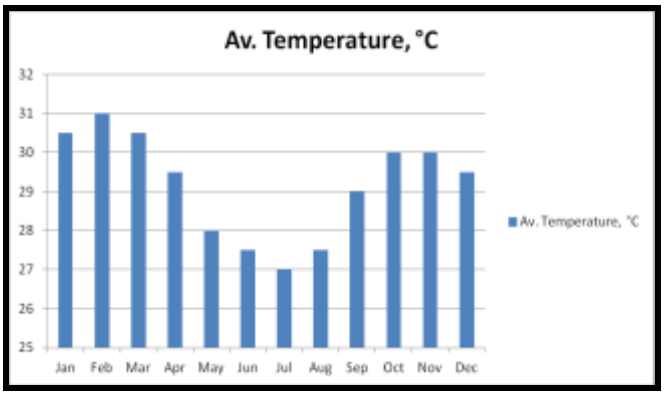

Figure 1.2: Monthly average temperature

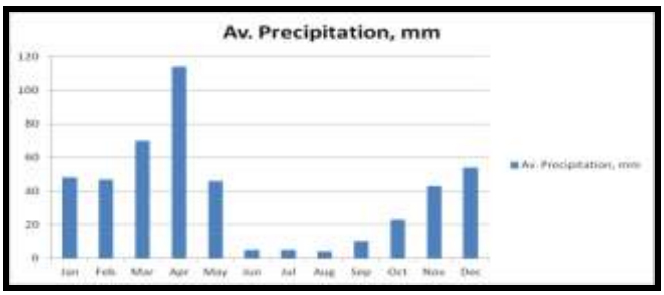

Figure 1.3: Monthly average rainfall

1.4.3 Vegetation

Underdeveloped thorny bushes and tiny patches of grass are evident in the area with riverines mostly composed of secluded trees. There are different types and forms of acacia trees with much of this vegetation along the lake, hills and hill-tops. Little vegetation cover is apparent along the river courses like along Ensonorua and Ewaso Nyiro rivers and around the lake (Plate 1.1). Much of the vegetation cover is utilized for construction, herbal medicine, animal feeds and also for wood fuel.

Plate 1.1: Vegetation found along Lake Magadi (Murhead et al., 2016)

Plate 1.2: Springs (Murhead et al., 2016)

1.4.4 Land use and land resources

A greater part of the study area is utilized by the nomads to feed livestock. The land is owned by the community living in this region. Other forms of ownership include: land trusts and private owners. Crop farming is done along the perennial rivers like Entasopia and Oloibortoto through

irrigation fields. Some portions of the land are leased by the Magadi Soda Company to carry out small scale irrigation. In general, approximately 4% of the area support energetic and evergreen vegetation (Plate 1.3) and the rest is semi-arid to arid.

Plate 1.3: Vegetation surrounding Magadi Soda Company (Murhead et al., 2016)

1.4.5 Physiography and Drainage

In terms of Physiography, Magadi area, (fig. 1.4), consists of plains, mountains, horsts and grabens. The area has different rock types of varying composition. The major rock types are basalts and the alkali trachyte. The landscape is characterized by troughs, faulted rocky escarpments and platforms, a majority of which are due to intense faulting. This region is a zone of the fissure basin floor.

The valley floor slopes southwards at a rate of about fifteen meters per kilometer. This includes the tilting of grabens and horsts. Some of the troughs in this area include Kordiya, Ewaso Nyiro Valley, Magadi, Krenia and Koora plains. The major river in the area is Ewaso Nyiro. It originates from the south-west side of the Mau range and transports a substantial volume of water in rainy seasons. The perennial tributaries of this river include Oloibortoto, Entasopia and

Longitoto rivers. The area is characterized by gorges, falls and rapids along the river courses. Most of the rivers are seasonal and do feed the Ewaso Nyiro river during the dry spell.

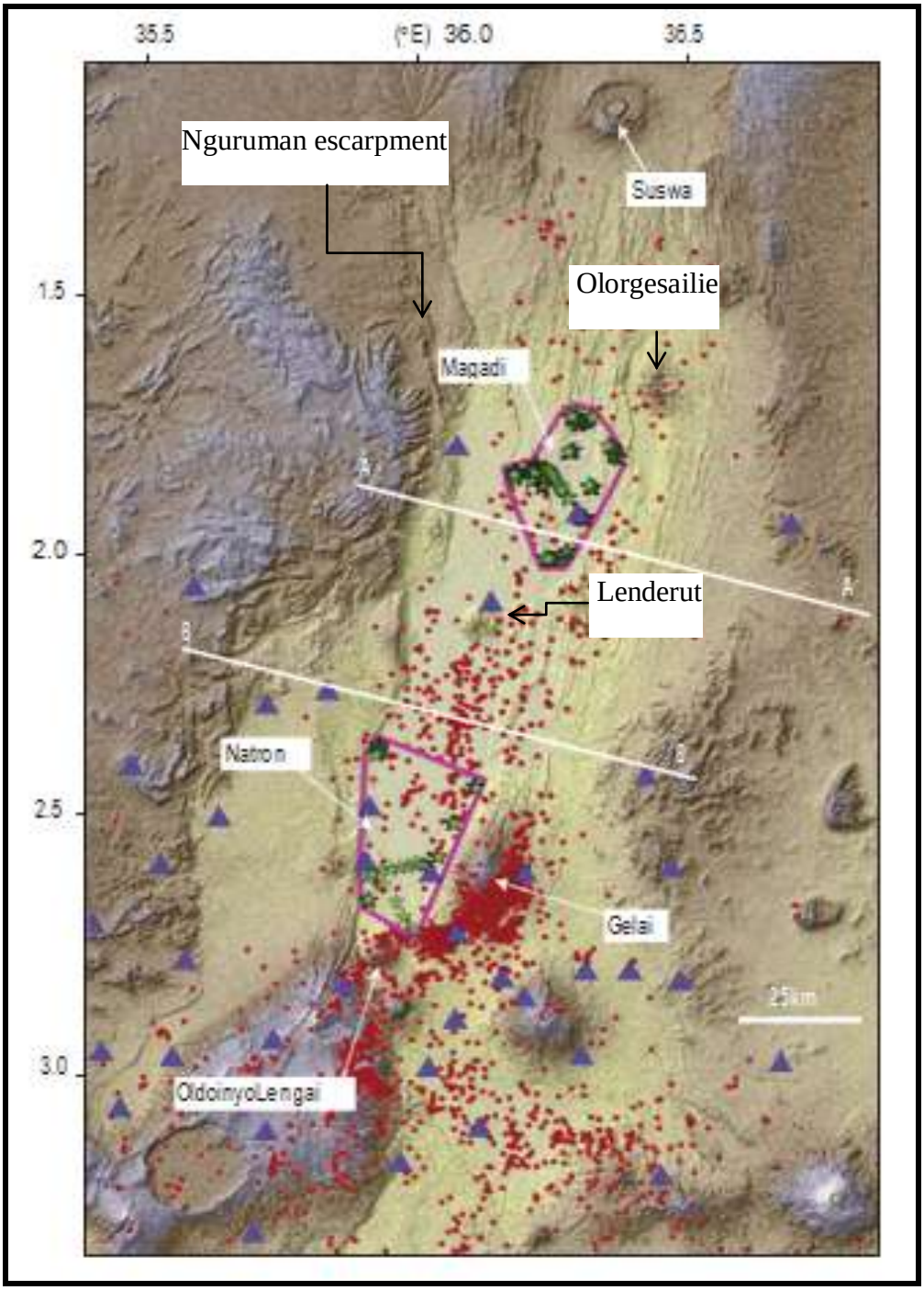

Figure 1.4: Physiography, seismicity (red), and crafti project seismic stations (blue) (Muirhead et al., 2016)

1.4.6 Soils

Some parts of Magadi area have rich brown soils (plate 1.4a&b) which incorporate fine sediments. Due to the richness of such soil, flourishing vegetation becomes evident during the wet season and partly throughout the dry months. This type of soil is found in areas such as Ewaso Nyiro, Kwenia swamp, east of Oldoinyo Nyiro and along the Koora plains. It cracks or shows cracks during the dry spell. The trough which was as a result of faulting contains most of the deposited sediments which are alluvial, silty or clayish in nature. Boulders and rocky surfaces are also evident in this area with a thin layer of yellowish brown silty soil. There are recent alluvial soils to the north of Magadi, sands to the south of Njoro Sindio and clays in swamps.

a)

b)

Plate 1.4: a) Brown to grey Soils, b) Fine soil particles (Muirhead et al., 2016)

1.4.7 Surface and groundwater resources

The surface water is mainly apparent through both permanent and seasonal rivers, swamps and other wetlands like the Lake Magadi itself. The rivers include Ewaso Nyiro, Oloibortoto, Endosapia and Longitoto. The subsurface water is very saline in nature and is recharged by the rivers like Oloibortoto, Entasopia, Longitoto and the major river, Ewaso Nyiro. The Ewaso Nyiro and other rivers lose water through infiltration and percolation.

1.5 Justification

Understanding the Magadi subsurface crust and its crustal structure changes over time will be of great benefit in many ways: Firstly, it will enhance hazard preparedness within the country by the availability of information got through continuous monitoring of crustal structure changes interpretations. Secondly, monitoring this crust continuously will be of good use because natural resources depletion or replenishment can be accurately deduced and accurate decision made on reliability and future trends.

1.6 Significance

The study is important to both communities living around the area, future researchers and policy makers in many ways. To begin with, this research was able to quantify possible hazardous zones by determining location of epicenters and hypocenters of local events within the Magadi area for public awareness and policy making guidelines in case of future development needs. In addition, this study was able to identify magmatic injections occurrence at different depths. This magmatic injection may continue up to near surface crust, hence, continued research will help identify other near surface magma pockets. And lastly, but, not least, continued research will enable piecing together our country's crustal history for use by future researchers who will advance further this science for the benefit of the public and country as a whole.

1.7 Aim and specific objectives

1.7.1 Aim

The aim of this study is to locate and relocate local earthquakes, update seismicity map, carry out 3D seismic inversion using Fast Marching method (FMM) and then establish Magadi crustal

structure changes for the period 1997-1998 and 2013-2014 by comparing current investigations to work done by Ibs-von Seht et al., (2001) & Roecker (2017).

1.7.2 Specific objectives

i. To locate, relocate and combine Ibs-von Seht et al. and crafti data sub-sets; 1997, 1998, 2013 and 2014 in order to incorporate the recent seismic activities not availed in older seismicity studies of Magadi area.

ii. To carry out 3D travel-time seismic tomography inversion in order to infer the nature of Magadi crustal structure and deformation geometry.

iii. To create north-south and east-west 2D slices from 3D travel-time seismic tomography inversion to aid in visualizing the 3D image of the subsurface of Magadi crust. Visualizing 3D Voxel block for this research is not possible because tomo3d software does not have 3D plotting scripts option but only 2D plotting scripts, slicing subroutine.

iv. To evaluate and compare the Magadi crustal structure between the year 1997 and 1998 (Ibs-von Seht et al., 2001 & this work) and 2013-2014 (Roecker 2017 & this work) in order to deduce the changes that have occurred over time at latitude 36.2^0 E and 2.1^0 S.

1.7.3 Outputs

i. Updated seismicity map of Magadi area by combining two data sub-sets; 1997, 1998, 2013 and 2014 in order to incorporate the recent seismic activities not availed in older seismicity studies of Magadi area.

ii. 3D travel-time seismic tomography inversion result. It was used to infer the nature of Magadi crustal structure developed in (iii) in form of 2D slices from final 3D model.

iii. Produced E-W and N-S 2D slices from the final 3D travel-time seismic tomography inversion model using gmtslice sub-routine in FMM software and plotted E-W & N-S 2D slices using GMT plotting scripts. 2D slices of the final 3D model; 1997-1998 (this work) & (Ibs-von Seht et al., 2001) and 2013-2014 (this work) & (Roecker 2017). The 3D Voxel block was not possible for this research due to lack of 3D plotting script.

iv. Evaluated and compared Magadi crustal structure between this work (1997-1998 & 2013-2014) with work by Ibs-von Seht et al., (2001) & Roecker (2017) and ascertained if anything different was evident.

2. LITERATURE REVIEW

Velocity variation is the disparity of the velocities in the underground. Such velocity contrast in the subsurface insinuates that various structures like faults and joints do exist and physical properties of rock units vary laterally and vertically in the subsurface. Investigations have been down in the study area to understand the different aspects of subsurface rock units. To begin with, efforts on 3D velocity determination beneath California paved way for more developments in 3D travel-time seismic tomography (Aki and Lee, 1976). Here, evaluation of suitability of inversion convergence is done by approximation of model covariance and resolution. Presupposed straight ray paths are used to get a damped least squares approach solution. Around the same year, Dziewonski et al uses travel residuals to get velocity contrast sections of the earth's mantle through spherical harmonic parameterization with a major limiting factor being the computing power at that time (Dziewonski et al., 1977).

In southern Norway, Aki (1974) uses travel-time seismic tomography, and teleseismic earthquakes, to get velocity contrast sections beneath Norwegian Seismic Array (Aki et al., 1977). Ray paths area allowed to curve unlike 1976 work where ray paths were presumed to be straight. Nevertheless, since path geometry is not kept posted to account for resolved heterogeneity, inversion is still linear. Another approach to 3D seismic tomography is by use of active source seismic studies. Here, borehole to borehole active source seismic imaging is used to evaluate Lacq oil field of southwest France. Explosives are put down one hole and then exploded. The resultant energy is propagated and finally documented by geophones positioned in different holes. Travel-time obtained from the resultant seismograms are inverted for the 2D velocity structure of the region disconnecting the two holes. A regular grid of nodes is used together with interpolation that guarantees continuity of velocity field and its initial derivative at every point. In order to resolve observed and model traveltimes Bois et al. (1971) and Hole (1992) use shooting technique of ray tracing that completely accounts for isotropic heterogeneity alongside iterative non-linear inversion (Bois et al., 1971; McMechan, 1983, 1987; Hole, 1992 and Bregman et al., 1989).

Medical imaging technique in form of back projection inversion methods were advanced and were popularly used in the crustal imaging works in-disfavor of gradient based with greater

invention coming in form of diffraction and wave equation tomography for recorded waveform (Pratt & Shipp, 1999; Song et al., 1995; Pratt & Goulty, 1991 and Pratt & Worthington, 1988). Bishop et al., (1985), Williamson, (1990) and Farra & Madariaga, (1988) combine beam spurting and slope based inversion methods to limit 2D models which are parameterized using steady speed slope blocks and cubic spline interfaces. Other forms include full waveform tomography, reflection (de Hoop et al., 2006; Zelt & White, 1995 and Hicks & Pratt, 2001) and wide-angle inversion (McCaughey & Singh, 1997; Kanasewich et al., 1994 and Wang & Braile, 1996) and traveltime-to-amplitude inversion (Wang et al., 2000; Clowes et al., 1995; Riahi & Juhlin, 1994 and Wang & Pratt, 1997). Broad-angle tomography is like reflection tomography. However, the origin-receiver separation in the former tends to be much higher than the later so that refracted beams are detectable from deeper depths. This makes seismic inversions a key component in resolving the earth's crustal structure (Staples et al., 1997; Darbyshire et al., 1998; Louden & Fan, 1998; Mjelde et al., 1998; Korenaga et al., 2000 and Bleibinhaus & Gebrande, 2006).

On the other hand, seismic tomography has been used widely to delineate the content of the existing outer section of the globe and lithosphere in three dimensions (Oncescu et al., 1984; Humphreys & Clayton, 1990; Benz et al., 1992; Glahn & Granet, 1993; Achauer, 1994; Saltzer & Humphreys, 1997; Graeber et al., 2002; Rawlinson et al. 2006b and Rawlinson & Kennett, 2008). Nearly every long distance seismological tomography currently applies iterative non-linear inversion combined with three dimensions beam tracing or wavefront trailing (VanDecar & Snieder, 1994; Steck et al., 1998; Morgan et al., 2000 and Rawlinson et al., 2006b). Many times, long distance seismological tomography is dependent on the recuperation of isotropic speed representations from onset duration residuals, while trials are accomplished to regain anisotropy (Plomerova et al., 2008; Morozov et al., 1998 and Zelt et al., 2001, 2006). Detailed local studies of the globe's surface have also been carried out using data from surface waves. In zones with short intervals configuration of broadband sensors, inter-sensor records (Friederich & Wielandt, 1995; Forsyth & Li, 2005 and Pedersen et al., 2003) are applied in approximating entire small scale spreading distinctiveness within the region of concern. The whole of these techniques have been used in many places to generate comprehensive tomographic representations of both the lithospheric mantle and earth's crust (Darbyshire & Lebedev, 2009; Weeraratne et al., 2003; Bruneton et al., 2004 and Li & Burke, 2006).

In the local scene, according to Kuria (2011) and Kianji (2002, 2004), it is considered that Magadi area has experienced high geodynamic activities and high rate of seismicity on the south of Lake Magadi showing that faulting activity is high in the south than in the northern side. Fault zones in the upper part of Lake Magadi signify high resistivity. This supports accumulation of stress hence setting a possible origin point of seismic activity. The fault on the southern part contains fluids which act as a lubricant that reduces stress build up which in turn reduces seismicity in the southern part (Ibs-von Seht et al., 2001; Tongue et al., 1992, 1994 and Kianji, 2002, 2004). Akinola (2010) suggested that fault compositions in the lower region of Lake Magadi serves as the water and gas channels which allow gushing of hydrothermal water and gas. This has more support from recent works done in this area (Lee et al., 2016 and Roecker et al., 2017).

Researchers have confirmed reliably the exterior fractures enlarge to a depth of 7,500 meters into the ground. Fractures and faults are highly associated with brittle rocks within the crust and normally occur when the stress applied on the brittle rocks due to tectonics surpasses the expandable constrains of the rocks. The tectonic occur due to the extruding molten rock into the exterior exerting stress on the rocks (Lerner & Cengage, 2003 and Akinola, 2010). Other workers (Molnar & Aggarwal, 1971; Ibs-von Seht et al., 2001; Akinola, 2010 and Kuria et al., 2010) accept the fact that parallel faults in the investigated portion bound the graben to the western and the eastern parts. Magadi Curie depth point at a depth of 12,100 meters marks the changeover point between ductile and brittle crust. Hence, the existence of surface manifestation of hot springs and high heat flow around Lake Magadi. Geodynamic activities in this region are as a result of association of thermal source, ground movements and their origins. The systems of faults in Magadi area are as a result of the area being subjected to various tectonic activities (Jones et al., 1977; Lambiase & Bosworth, 1995 and Maguire & Long, 1976). A structural survey done in a small part of the study region within the Kenya Marble Quarries enabled postulations that materials of the basement type were crinkled about axes trending ENE-to-WSW. Majority of the minor structures are aligned along this orientation but foliation and bedding strike NNW-to-SSE. From the time when geophysical studies were first accomplished in the Gregory Rift using various techniques which included seismic method, Magadi has proved over time to be

active. Throughout various micro-earthquake surveys in the country, workers (Aggarwal & Molnar, 1971) established the study area fissure to be having activity in the most dynamic region within and along Gregorian fissure. The KRISP 91-94 project archived several such local micro-earthquakes (Hollnack and Stangl, 1998) and had a great contribution in understanding the nature of crustal structures in Magadi area.

And lastly, later on between 1997 and 1998, work by other researchers (Ibs-von Seht et al., 2001) set up a seismology recording system within an area which consisted of 15 seismic station sites and operated for a period of eight months from November nineteen ninety seven to June nineteen ninety eight. At least 10 events were recorded daily during the exercise and established to be uniformly disseminated on the rift ground. In addition to background movements, clustered events having a frequency of above three hundred earthquakes were recorded daily. The crustal structure of the Magadi crust was investigated by Ibs-von Seht et al., (2001). He found out that there were escalated speeds in some sections and diminished speeds in other sections. The escalated speeds could be elucidated by dark rocks that had encroached into the earth surface. The diminished speeds were due to exceedingly broken rocks. Other works (Tongue, 1990) confirmed that the middle region of the fissure basin in the country along the Lake Bogoria area is characterized by escalated speeds to the East. Diminished speeds were evident to the west due to the presence of Bogoria-Emsos-Legisianana fault scarp. This fault scarp divides the area into diminished speeds within west and soaring speeds within east. Additional work by other scientists (Roecker et al., 2017) shows major crustal structure changes by introduction of low velocity pockets (small magma chambers). These low velocity zones have been introduced into regions initially thought to be high velocity zones (Ibs-von Seht et al., 2001). Magma injection from the main magma repository existing between near the surface of the earth and deeper earth regions into other areas is the main driving force.

3. GEOLOGY AND STRUCTURES

3.1 Aspects Summary

The geology of the study area is closely related to other aspects of both geo-chemistry, morphological and environmental. Different aspects like: geochemistry, tectonic changes, geological aspect and the structural setting are discussed as follows.

3.2 Geology and Geological setting

Early scientists (Baker, 1958, 1963; Baker & Wohlenberg 1971; Baker et al., 1972; Baker and Mitchell 1976) state that the geology of Lake Magadi region is characterized by the Precambrian Metamorphic rocks; it has the Holocene-Recent lacustrine fluviatile sediments and Pliocene to Pleistocene volcanic rocks. The Precambrian metamorphic does lie beneath the Olivine basalts of the Kilikiti podium. They extruded about 2.8 Ma and down-faulted to the rift floor at the Nguruman escarpment. Furthermore, work by Crossley (Crossley, 1979), and Crossley & Knight (1981) supports the fact that the volcanic action in this region transpired about 1.05 Ma with the formation of Magadi plateau trachyte sequences. It is probable that the last geological developments of the Lake Magadi region relates to the lacustrine fluviatile sediments, which include lake beds and river beds sediments found in Lake Magadi and Ewaso Ngiro basin. The movement of this lithology is balanced by the new NW-SE fault (Kuria, 2011).

In terms of detailed geology, firstly, in the surrounding area, the Tanzania craton falls under the granite greenstone terrain dated about 2.85 Geological years encompassed of the older Nyanzian group with overlying younger Kavirondian group (Davies & Mathu, 1996). Metavolcanics of the Nyanzian group, range from tholeitic basalts to calcic-alkaline andesite, dacites, rhyolites, pyroclastic agglomerates, tuffs and ashes (Opiyo-Akech & Muhongo, 1999; Ichangi & Maclean, 1991, Nyambok, 1992 and Mathu & Nyambok, 1993). Secondly, work by Matheson (Matheson, 1966) supposes that the Geology of the study area is composed of the basement system like the metamorphosed calcareous, psammitic, politic to semi-pelitic sediments, migmatites, anatectic and palingenetic rocks. The tertiary rocks include: Kapiti phonolite, upper athi tuffs, mbagathi trachyte, olorgesailie trachytes, Augite basalts, Agglomerates, Olorgesailie biotite phonolite, Olorgesailie phonolitic Nephelinite, Ol Doinyo Narok Agglomerate and Kirichwa valley Tuff, Ol

Esayeiti Lower Trachyte, Oligoclase Tephrite, Phonolite, Upper Trachyte, Ol Esayeiti Agglomerate, Ol Keju Nero Basalts. And finally, it has been confirmed that the Pleistocene Volcanic rocks in the area compose of Alkali Trachytes and Orthophyre-Trachyte. The Olorgesailie Lake Beds and Recent Deposits are the major part of Superficial Deposits in Magadi region.

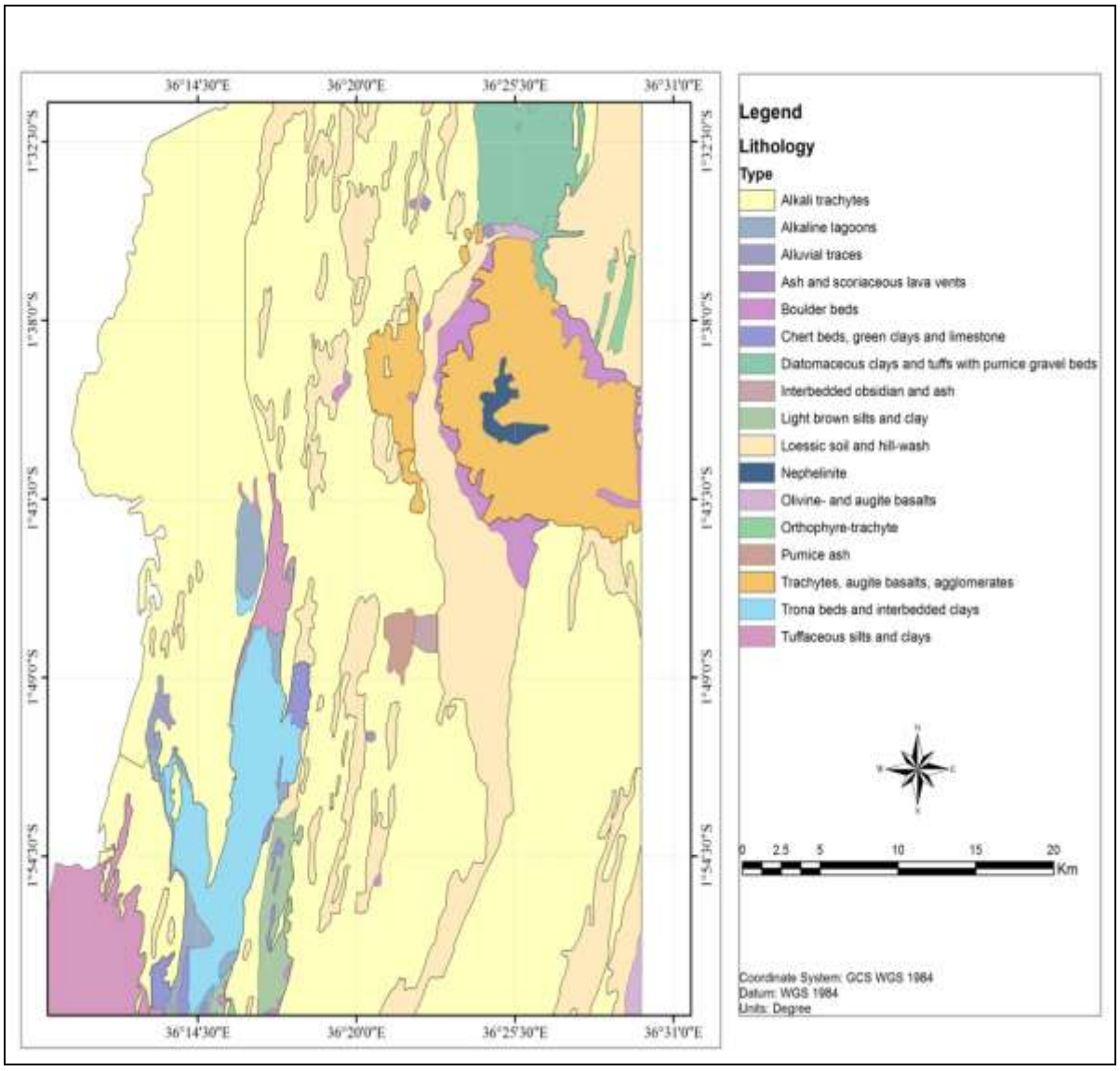

Figure 3.1: Geological map of Magadi area

From the figure 3.1 above, the Northern part is composed of alkali trachytes, Loessic soil and hill-wash. Loessic soil, hill-wash, alkali trachytes, diatomaceous clays, tuffs with pumice gravel

beds, othophyre-trachyte, light brown silts, clay, Augite basalt and agglomerates are found to the North Eastern region. The Eastern area has boulder beds, trachytes, Augite basalts, agglomerates, alkali trachytes, loessic soil and hill wash and Nephelinite. Furthermore, there are olivine and Augite basalts, alkali trachytes, Loessic soil and hill-wash to the South Eastern piece. The Southern expanse possess alkali trachyte, loessic soil with hill-wash, light brown silts and clays. Distinctively, the South western part has tuffaceous silts, clays, and trona beds interbedded with clays, alkali trachytes, alkali lagoons and alluvial traces. And finally, the Western and the North western have alkali trachyte, trona, alkali lagoon sand alkali trachytes, and Loessic soils with clays respectively. According to the findings of Ngecu (Ngecu, 1993) the Kavirondian (younger group) comprises of the basal conglomerates, grey-wackes and sandstones with shale and mudstones that transpire at the top. The Mozambique belt, a Neoproterozoic mobile belt dating about 0.75 Geological years, comprises of medium to high grade metamorphic rocks, that is, schists, gneisses, migmatites, granulites, granitoid gneisses and granites. Most of these rocks are re-worked. Others (Mathu & Davies, 1996) state that other common rock types within the belt include: amphibolites, serpentinites, quartzites and marble but the diorites, gabbros and ultramafics are more widely scattered. An important structural feature in the NW-SE trending zone of ductile shear is known as Anza-Nandi-Loita (ANL) thrusting in the underlying Precambrian basement (Smith & Mosley, 1993). The local scale faulting is evident in the area. The New NW-SE trending fault brings counter-balance to the Old NE-SW fault in Magadi (Kuria, 2011). The geological implication of the shear zone is the distribution of the strongly alkaline carbonatitic volcanism along the Craton margin (Smith, 1994).

3.3 Chemical elements of Magadi Rocks

On the other hand, in terms of geochemistry, most of the rocks are composed of sulphides, chlorides, silicates, oxides and carbonates with varying proportions of the metal cations like calcium (Ca), magnesium (Mg), aluminum (Al), sodium (Na), and potassium (K).

Table 3.1: Geology of Magadi (modified from Baker, 1963)

Period	Appr Time 10^6	Geological period	Kind of process	

	years						
Quarternary			Tectonic activity	Volcanism	Sedimentation	Erosion	
		Recent			Sedimentation		Evaporite series, trona
						Erosion	Erosion
	0.1	Upper Pleistocene			Sedimentation		High Magadi beds and Ewaso nyiro alluvium
			Tectonic activity			Erosion	Minor faulting and erosion
	0.4	Middle Pleistocene			Sedimentation		Olorgisailie lake beds and Cherts
	0.6		Tectonic activity			Erosion	Gritfaulting and erosion
					Sedimentation		Oloronga lake bed
				Volcanism			Volcanic vents, ashes, scoria. Ol Doinyo Nyegi
				Volcanism			Plateau trachyte

	1	Lower Pleistocene		Volcanism			Trachyte
Tertiary	2	Upper Pliocene	Tectonic activity			Erosion	Nguruman fault ll and erosion
				Volcanism			Trachyte
				Volcanism			Kirikiti basalt
				Volcanism			Ologorsaile, Shompole and Lenderut Volcanics
	20	Middle/Lower Miocene	Tectonic activity			Erosion	Nguruman fault l and erosion
						Erosion	Erosion
Precambrian							Basement

3.4 Tectonic Changes

The area has undergone a myriad of tectonic events. The events range from normal faulting and down-warping, Depositional Period and further down-warping. Such events involve the movement of plates. The plates move seemingly independently, which indicates that affected zones are dynamic. The regional stresses in the crust generate deformation systems with characteristic geometry, attitudes and organisation. The fundamental structure subsystem in the Magadi area is the extension system. In this subsystem, horizontal extension on normal faults implies that the smallest deviatoric stress is applied in one horizontal direction. In respect to the study area, the major tectonic events and deposition has been further described as following:

3.4.1 Normal faulting and down-warping

There existed a stable slab which later experienced tensional forces. This led to the development of a diverging boundary on the continent where two parts split apart. The middle portion sunk to create a graben with escarpments existing on both sides. The sinking process can also be referred to as down-warping process. This process produces faults which are grouped into three types. These types include rift faults, grid faults and minor faults. Of the rift faults those at the bottom of the Nguruman escarpment are the most significant.

The structure of the Nguruman escarpment implies that it was initially developed by faulting prior to the eruption of rift valley lavas. The earliest structure was a fault. It had about 950 meters throw, cutting through basement system rocks, down-throwing eastwards. It can be trailed along the bottom of the Nguruman escarpment in its southern region. This fault passes below the Kirikiti basalts north-north-west of the Oloibortoto river gorge. It is hidden from sight by lavas and boulder beds except in the Oloibortoto river segment. Judging by the stage of dissection attained by the escarpment, this fault is the oldest in the area and is probably of middle or early Tertiary age. It probably could be regarded as the fault instigating the rift valley subsidence in the area. From analysis of its fracture-zone it appears to be of normal tensional nature.

3.4.2 Depositional period

When materials like sand, various clays, boulders and organic materials were and now are still being deposited in the graben which acts as the depocenters along the rifting zone. This process has been slow in Magadi area such that structural elements of geology are still clearly visible. This is because of the short geological history of majority of the rocks. These rocks, apart from the basement system rocks, range from late Tertiary to Recent in age. Consequently, erosion has not been adequate to level off features of tectonic origin. Here, faulting is the major factor in the structure. It determines not only the geological lines but also the topography of the study area.

3.4.3 Further down-warping

When the overlying matter increases with time, the slab which sunk reaches a point where it cannot bear the weight. This leads to a further sinking to levels which are lower than before. This creates a graben which is much deeper than the initial one. This is the case for the study area. In that later movements along the southern region of the Nguruman fault and subsequent formation

of new faults north of Endosapia River after eruption of Kirikiti basalts, deepened the rift valley by an additional 350 meters, consequently giving rise to Kirikiti platform. The Kirikiti fault separates into two major and two minor faults east of Naimithigiria plateau. They trend north-eastwards and unite with Lengitoto fault. It (Lengitoto fault) is the offset continuation of Kirikiti fault and is situated along the gorge of upper Ewaso Nyiro. The sections of Kirikiti fault down fault lava blocks tilted to the east.

The upper Ewaso Nyiro depression is margined on the west by step faults. In the east, there is no clear-cut boundary. The ground slopes gently to the river from the scarp north of Ol Doinyo Nyiro. The age of the rejuvenation of the faulting along the Nguruman escarpment is not precisely known, but it must be considerably younger than the earlier fault. This is due to the fact that the edge of Kirikiti platform is comparatively un-eroded. The fault may, hence, be end-Tertiary or early Pleistocene in age.

The eastern edge of the rift valley is not as precipitous as the west. Thus, the impression given is that the main rift faults are in the west and that the valley floor sloped westwards throughout most of its history. The grid faults, which occur across the rift valley within the study area, are entirely lower middle Pleistocene in age. They cut the level surface formed by the plateau trachytes. The fault pattern in the grid-faulted area indicates that the general structure is that of quite extensive, raised and often tilted fault-blocks, traversed by marginal relatively shallow narrow fault-troughs.

3.5 Structural and tectonic setting

Early workers confirm that the faulting (fig. 3.2) during the Pleistocene to the Recent dissecting the rift floor is elevated in Magadi area in comparison with other sections of the Kenya Rift, that is, the Baringo-Turkana and Aberdere detachment. Hence, Magadi-Natron, a broad half graben depression, becomes a submeridian that is traversed by major antithetic and tilted blocks of late Miocene to early Pliocene (Baker & Mitchell, 1976 and Bosworth et al.,1986) with Suswa and Gelai volcanoes to the north and south respectively.

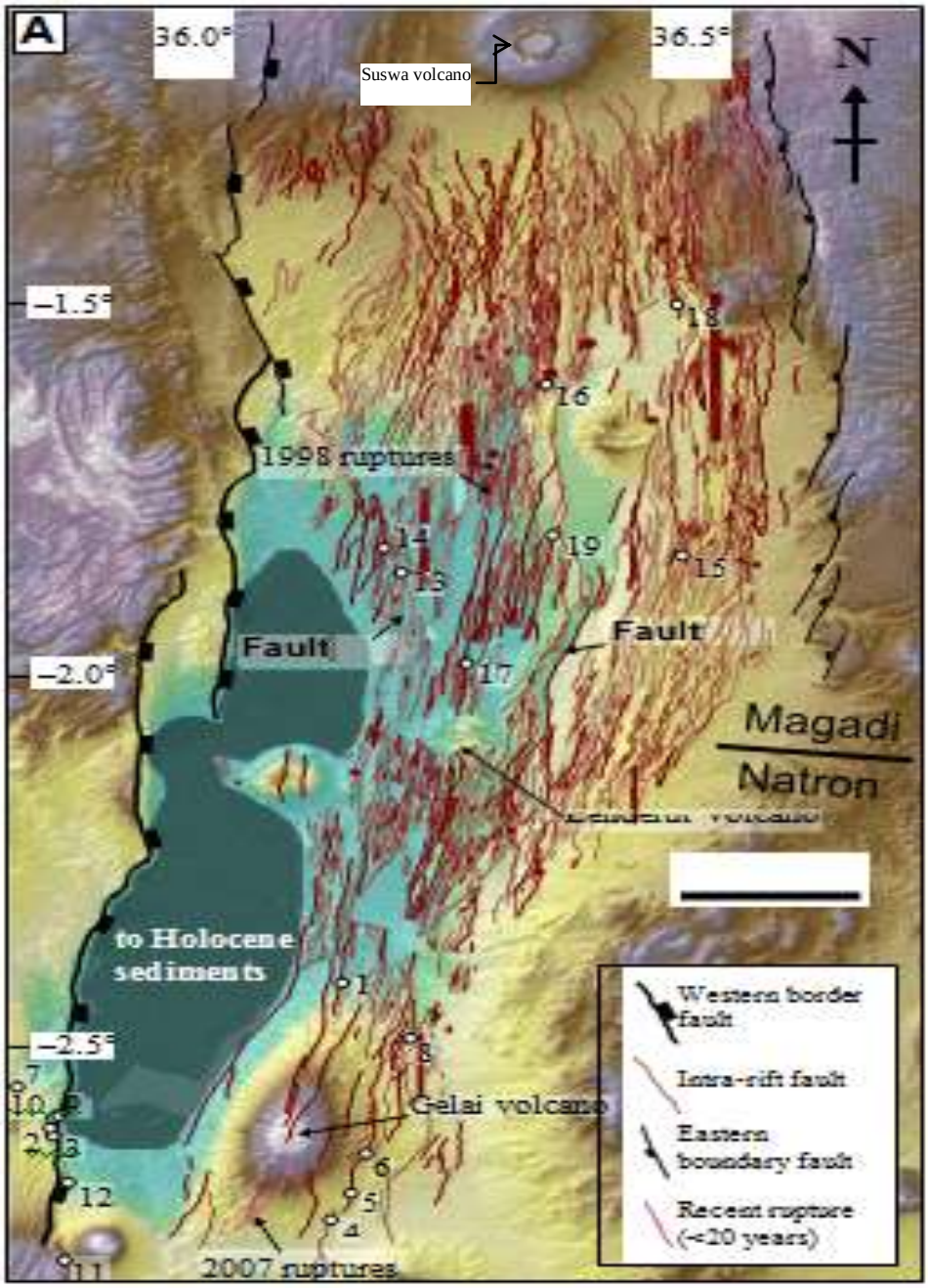

Figure 3.2: Magadi-Natron structures 1.1 degrees south to 2.2 degrees south and 35.5 degrees east to 36.8 degrees east (Muirhead et al., 2016)

In 1990, Magadi was investigated using geophysical techniques such as magnetic, gravity and wide-angle seismic refraction: KRISP85, along the rift axis from L.Baringo to L.Magadi and KRISP94, across the Kenya Rift through Lake Magadi (Prodehl et al., 1994, 1997b). The rift at the depression at the L. Magadi in the Kenya Paleogene Rift valley follows a marked sub-

meridian trend controlled by Proterozoic structures, along the margins between the Tanzanian Craton and Precambrian Mozambique belt. The submeridian structures are separated by the tranverse fault structures inferred to have developed along areas of weaker crust caused by E-W regional extension on the major escarpments. It sub-divided the Kenya rift into three sections: northern Baringo-Turkana, Aberdere detachment and southern Magadi-Natron, which are separated by a major NW-SE trending ductile shear zones in the underlying Precambrian basement (Smith & Mosley, 1993 and Mathu & Davies, 1996). Furthermore, according to Lee Gall (Lee Gall et al., 2000, 2008) the northern limit of the Lake Magadi-Natron trough is characterized by a major NW-SE trending ductile shear zone in the underlying Precambrian basement and to the south; the rift evolves from asymmetrical graben to the east facing half graben bounded to the west by a double system of normal faults. Work by Baker and others (Baker et al., 1972 and Smith, 1994) scrutinized the fact that with time, there was a north to south rift propagation and a shift in volcanism from the rift margins towards the axial part of the rift floor.

In addition, the mantle structure, constrained from geophysical survey, is marked by a narrow and linear N-S steep-sided low-velocity channel occurring at an average depth of 150kms, and between 80kms to 200kms, connoting local lithospheric thinning (Achauer, 1991). As per the work of Smith (Smith, 1994) it is confirmed that the southern section, which corresponds to L. Magadi region extending to Tanzania, is supposed to have developed on a Craton type lithosphere that has been obscured by imbricated thrust slices and gravitationally collapsed nappes of the Tanzanian Craton and the Mozambique belt.

4. THEORETICAL FRAMEWORK

4.1 Earthquake location theory - Seisan

In the seisan software (Ottemoller, 2008-11) earthquakes are located using the LOCATE sub-routine. The hypocenter and origin time calculation is done automatically by the seisan software. Mathematically, the calculated arrival time t_i^c at the station is given as:-

$$t_i^c=T(x_i,y_i,z_i,x_o,y_o,z_o)+t_o \qquad 4.1.$$

Here, T being move-out instance, and t_o is the source instance. In order to determine the origin times and hypocenters, arrival time observations from three or more stations are used. According to Ottemoller (2008-11), for every n observation, there are n equations leading to an overdetermined problem, hence, residuals or misfits have to be minimized to solve such a problem. In seisan software, the residual r_i is given as follows:-

$$r_i=t_i^o-t_i^c \qquad 4.2.$$

In the above case, t_i^o is the practical influx duration and t_i^c is the predicted onset duration. Ottemoller (2008-11) concurs with the fact that the move-out duration function T is a nonsequential function of the representation constraints. Hence, it is impossible to solve equation 4.1. Since, the nonlinearity of T significantly obscures the process of inverting for the preeminent focal values. The nonlinearity is manifested in both hypocenter and epicenter determinations. In epicenter resolution, the move-out duration t_i from a position (x, y) to a location (x_i, y_i) is given as follows:-

$$t_i=((x-x_i)^2+(y-y_i)^2)^{0.5}/v \qquad 4.3.$$

In equation 4.3 above, v is the speed and t_i is the move-out duration. When the arrival time t_i in equation 4.3 is taken to consideration, it clearly reveals that travel time does not scale linearly with either y or x. Hence, it is impossible to use linear equations to solve equation 4.3. Similarly,

in hypocenter determination, the move-out duration t_i from a position (x, y, z) to a location (x_i, y_i, z_i) is given as follows:-

$$t_i=((x-x_i)^2+(y-y_i)^2+(z-z_i)^2)^{0.5}/v \qquad 4.4.$$

Also, in equation 4.4, it is clearly revealed that travel time does not scale linearly with z. This means it is also impossible to use linear equations to solve equation 4.4 with respect to z component.

This implies that provided that there is adequate move-out duration, there is no easy means of getting acceptable and at the same time unique solution. To solve the problem, the nonlinear inversion problem ought to be linearized. To begin with, a guess of hypocenter location and origin time (x_o, y_o, z_o, t_o) are made. In the simplest form, that is, in the case of local earthquakes close to or in the vicinity of a station network, it is done using location close to the station with the first move-out duration and assigning that move-out duration as t_o. It is then presupposed that the correct focus is adequately close to the deduced values so that move-out duration residual at the test focus is a linear function of the improvement to be made in focal distance. As given in equation 4.2, travel time residuals are assumed to exist because of the inaccuracy in the test resolution and necessary adjustment (Δx, Δy and Δz) are required to make them nil. In case the adjustments are minimal, calculation of the resultant adjustments in move-out duration is done by estimating the move-out duration function using the first term of Taylor series. Such corrections approximation is given as follows:-

$$r_i=(\partial T/\partial x_i)*\Delta x+(\partial T/\partial y_i)*\Delta y+(\partial T/\partial z_i)*\Delta z+\Delta t \qquad 4.5.$$

Here, r_i, are the residuals.

In the matrix form, equation 4.5 above is rewritten as follows:-

$$r=G*X \qquad 4.6.$$

In equation 4.6 above, r is the residual vector, G is the matrix of the fractional derivatives with origin duration rectification term in the last column and X is the unknown adjustment vector in position and source duration. Here, there is a set of linear equations with n unknowns (corrections to hypocenter and source duration), with normally one equation for each one of the observed duration. In case there are lots of additional equations than unknowns, that is, m stations with p phases, then each would give m*p equations.

The solution to equation 4.5 or 4.6 is found using the least squares method. The initial test solution is adjusted with the outcome of equation 4.5 or 4.6 and new solution is then applied as test solution for the subsequent iteration. The iteration procedure is then sustained until a predefined breakpoint, either the smallest residuum r, or, a final repetition providing insignificant hypocentral parameter variations than a set basis, or, entire amount of iteration, is reached. If the first estimate is very near the mathematically preeminent and unique result, the iterative process converges rapidly. Very large residuals after converge of iterative process would mean that the result converges to a small scale least and not the anticipated global smallest.

4.2 Fast Marching theory – FMM

4.2.1 Forward Problem theory for Fm3d-3D Eikonal Equation

According to Nicholas and co-workers (Nicholas, 1996; Officer, 1958; Vidale, 1988 and Podvin & Lacomte, 1991) when a flat function P(x, y, z) is considered together with a spatially changeable amplitude P_0(x, y, z) including spatially changeable move-out duration T(x, y, z) entirely subsequent eikonal equation can be written as follows:-

$$P(x, y, z) = P_0(x, y, z)\exp\{-iw[t-T(x, y, z)]\} \qquad 4.7.$$

Assuming for an instant that whole energy amplitude P_0(x, y, z) does not fluctuate spatially, nevertheless that it is a constant. Thus, whole plane-wave result of our type of equation 4.7 gratifies whole scalar wave equation 4.8. Replacement of equation 4.6 into equation 4.7 produces equation 4.8 which is given as follows:-

$$\partial^2 P \partial x^2 + \partial^2 P \partial y^2 + \partial^2 P \partial z^2 = 1 v^2(x, y, z) \partial^2 P \partial t^2 \quad 4.7.$$

$$(\partial T \partial x)^2 + (\partial T \partial y)^2 + (\partial T \partial z)^2 = 1 v^2(x, y, z) \quad 4.8.$$

Equation 4.8 above is referred to as the eikonal equation; a beam hypothetical estimation to the scalar wave equation 4.7. Even as entire result of nondirectional wave equation 4.7 stands for the wave-field P(x, y, z) on the position at space (x, y, z). At a moment of duration t, the result of the eikonal equation 4.8 stands for the move-out duration T(x, y, z) for a beam going via a position (x, y, z) at a substance having speed v(x, y, z). Purposely, T(x, y, z) = invariable, stands for whole wavefront of invariable phase at a moment of duration. Entire wave should be transmitted from one wavefront to the subsequent one by means of ray-paths, which are at right angles to the wavefronts.

When the medium velocity is not constant but is an arbitrary function of space variables v(x, y, z). And wave amplitude $P_0(x, y, z)$ is not constant but also varies spatially, then the traveltime function T(x, y, z) of equation 4.6 is not a solution to the eikonal equation 4.7. In favor of the wave function, such as that given by equation 4.6, with spatially varying amplitudes, the eikonal equation is an excellent estimation to the wave equation only at a high frequency limit. The elevated frequency limit is comparable to short wavelengths. The estimation is applicable provided that partial adjustment in the velocity gradient is much less than the wave frequency. Thus, it implies that the eikonal equation can be applied to work out move-out duration provided that the velocity-depth representation does not hold large velocity gradients. The result to nondirectional wave equation is devised by applying either fast marching technique or a finite difference method. Similarly, the eikonal equation 4.7 is worked out using either FMM technique or a finite difference technique.

Consider a 3-D computation mesh sketch (fig. 4.1). We would like to work out the move-out duration T by eikonal equation at grid position $(x+\Delta x, y, z+\Delta z)$ applying the conventional move-out duration on grid positions (x, y, z), $(x+\Delta x, y, z)$ and $(x+\Delta x, y+\Delta y, z)$.

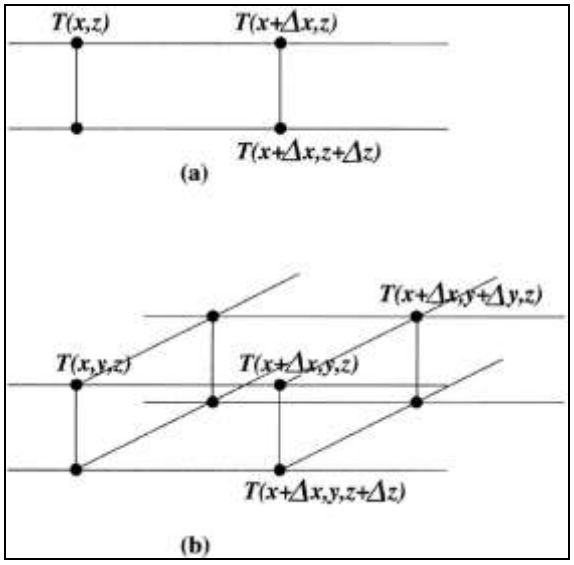

Figure 4.1: Finite difference mesh used for (a) 2D and 3D solution to the eikonal equation (Podvin & Lacomte, 1991).

Working out move-out duration at depth z+Δz from the one at depth z implies extrapolating T in the vertical direction (z-axis). Modifying equation 4.8 in the type of an extrapolation equation, the resultant equation is as given here-below:-

$$v\partial T\partial z=1-(v\partial T\partial x)^2-(v\partial T\partial y)^2 \qquad 4.9.$$

Thus, the 3D eikonal equation 4.9 can be worked out for the move-out duration parameters T(x, y, z). This is meant to favor the transmitting wavefront via a speed field v(x, y, z) in entire underground. The process is possible by applying either finite disparity or fast marching method. Figure 4.3 shows the move-out duration contours via similar velocity-depth representation as in figure 4.4 worked out by applying the eikonal equation. These may be considered as wavefronts expanding from a source at the surface located at 3 km from the origin. Note that the shape of the traveltime contours honors the boundaries with velocity contrast. On the other hand, the move-out duration contours cannot demonstrate the abrupt velocity variation as would be the case at a boundary. Such a boundary entails salt-sediment interface which has sharp velocity contrast.

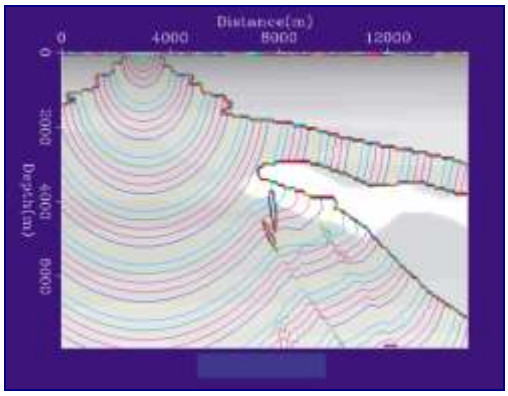

Figure 4.2: Move-out duration curves generated by ray trailing via the speed-depth representation which incorporates a salt sill signified by a white portion (Podvin & Lacomte, 1991).

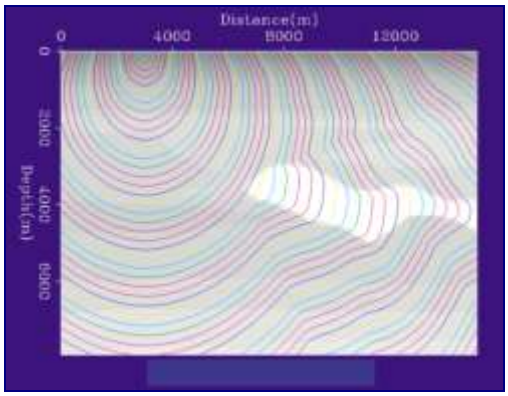

Figure 4.3: Move-out duration curves generated by a result of eikonal equation via the speed-depth representation which incorporates the salt sill symbolized by a white portion (Podvin & Lacomte, 1991).

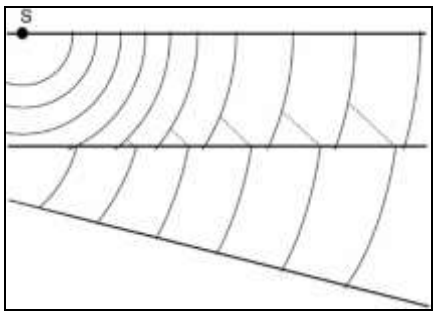

Figure 4.4: Geometry of a spreading energy beginning at origin positioned on earth's exterior position S. A section over second horizontal line possesses the lesser speed unlike a section beneath. These spotted outlines show then wavefronts linked with energy. This energy is refracted at critical angle (Podvin & Lacomte, 1991).

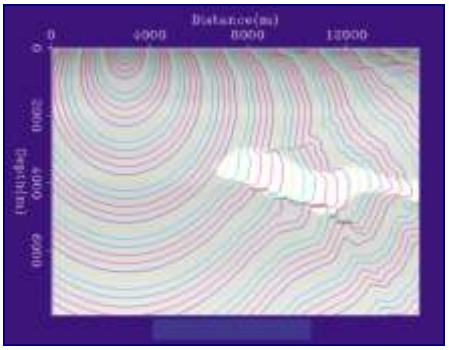

Figure 4.5: Move-out duration curves generated by a result of eikonal equation which does not incorporate the chief energy, but incorporates the salt sill symbolized by a white portion (Podvin & Lacomte, 1991)

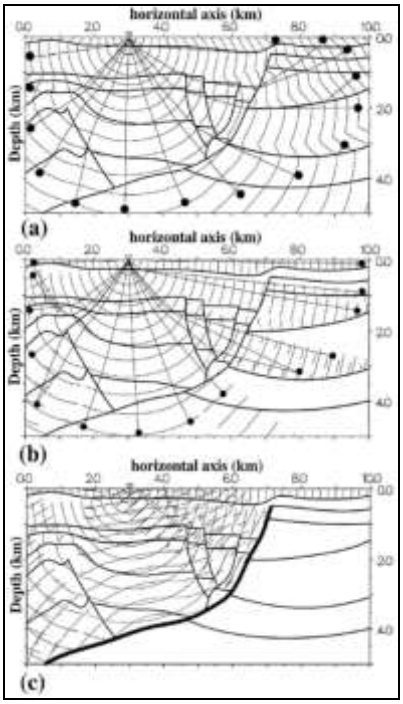

Figure 4.6: Move-out duration curves generated (a) by finite difference result to eikonal equation, (c) spreading energy creation (Podvin & Lacomte, 1991)

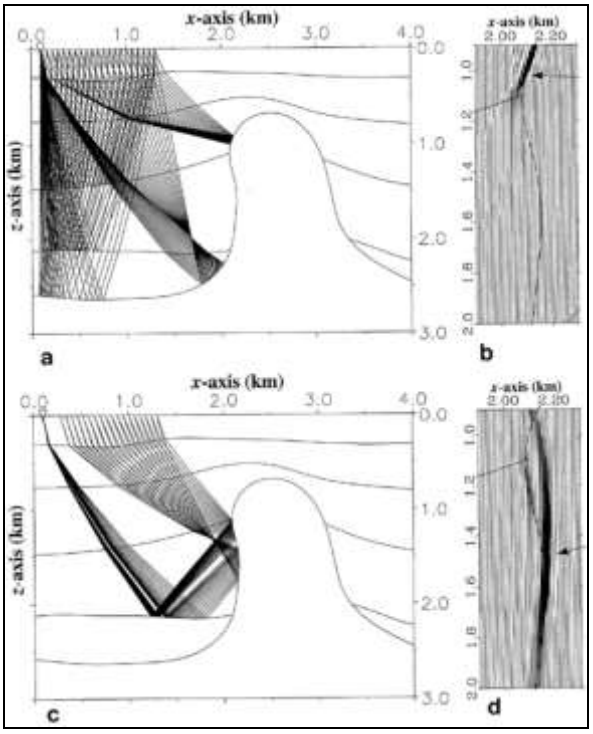

Figure 4.7: Two dissimilar elucidations of a salt flank by the sole origin plus beams linked by (a) main reflections that produce a picture of this salt edge in (b), (c) reflections that first bounce off a deeper section margin (Podvin & Lacomte, 1991)

To clarify the even manner of the move-out duration contours on section margins on figure 4.3, we refer to figure 4.4 of a spreading wavefront via a horizontal interface with a huge speed disparity. On the critical angle of refraction, waves propagate by the side of the section margin with the quicker speed of the beneath section. Ultimately, these waves bend back into the upper section. They are documented in the type of initial onsets. As a result, they are frequently referred to as head waves. Being aware that the wavefront linked with the head waves have a tendency of smoothing out the sharp variation in the spreading wavefront as it traverses above the section margin with the speed disparity. It is these outcomes that they observe in figure 4.3. Here, the move-out duration contours create an even shift out of the mechanically disintegrated deposit to the salt sill section. Preferably, the move-out duration contours would enunciate the sharp section margins. Despite the fact that most of the results to the eikonal equation incorporate the head waves shown in figure 4.3, the rest keeps out the head waves. Figure 4.5 demonstrates the move-out duration contours obtained from the entire result of the whole eikonal equation that has kept out the chief waves. Note the sharp changes in the move-out duration

contours. At some locations, they appear to coincide nicely with the salt-sediment layer boundary. Nevertheless, the match is not consistent at all locations. The move-out duration contours show rapid fluctuations that are not physically plausible.

Figure 4.6a illustrates move-out duration contours that were worked out applying the finite-disparity result to the eikonal equation. The speed-depth representation consists of sections having speeds fluctuation beginning at one thousand five hundred meters per second to four thousand meters per second. Be aware that the eikonal results, even if they are related merely among the fastest onset, constantly produce a raypath beginning at an origin on entire exterior to the position on the entire deeper ground via a gridded speed-depth representation. Most of entire raypaths can be signified via trajectories which possess the solid circle in the entire last part. The even nature of the whole move-out duration contours can be connected to the entire head wave which frequently is the initial onset. On the contrary to entire eikonal result, whole wavefront structure produces manifold onsets as given in figure 4.6b. Again, a few of the whole raypaths can be shown via trajectories which possess the solid circle on the last part. Be aware of manifold raypaths connected via the one position on the entire ground. Wherever the head wave or diffraction build up, entire wavefront structure creates an incomplete move-out duration contour. In wavefront structure, on the contrary, one is allowed to be discriminatory on entire form of beams which one would like to incorporate on entire summation of the amplitudes. Figure 4.6c illustrates move-out duration contours linked to whole reflecting margin signified via the wide arc. For sure, the whole result from wavefront structure on these aspects incorporates onsets linked to reflected wave including the entire transmitted waves. Our eikonal result cannot essentially produce expected highest energy alongside entire single-onset raypath. On wavefront development, on the other hand, amplitudes linked to manifold onsets are then incorporated into final summation. Hence, the likelihood of capturing entire maximum-energy onset enhances, though this escalates work out cost. Through incorporating several onsets into entire summation, whole chance of obtaining a complete picture of a complex composition as well is enhanced. Figure 4.7a illustrates raypaths beginning at one origin on entire exterior which elucidates sections of entire sharp edge of the salt dome. Through applying entire onsets linked to the raypaths, merely, on Kirchoff summation, entire consequential partial picture given on figure 4.7b is attained. By including in the summation the onsets linked to the reflections off the salt

flank, as well as the onsets linked to the reflections off the salt flank and those linked to the reflections from a deeper interface that bounce off the salt flank, figure 4.7c, a more complete picture is attained, as given in figure 4.7d. All these wavefronts are trailed by eikonal solvers. The 3D eikonal solver's wavefront tracking Fast Marching scheme is discussed as follows.

Fast Marching technique, FMM, (Sethian, 1999 and Sethian & Popovici, 1999) indirectly trails the entire development of initial onset wavefronts through incorporating the contributory narrow-band progression system having an upwind entropy-gratifying finite disparity result of entire eikonal equation. Consequently, wavefronts could be trailed beginning at origin and sensor to the interface. Fermat's Principle of stationary duration is used to set reflection positions (Podvin & Lacomte, 1991 and Riahi & Juhlin, 1994). Also, three dimensions scheme can be used to work out the move-out duration of the reflected wavefield. This is possible through supposing that the entire encroaching wavefront and reflector are sufficiently smooth to validate a local planar approximation, which then allows Snell's Law to be applied explicitly. On the other hand, the multi-stage FMM (Rawlinson & Sambridge, 2004a, 2004b) transmits wavefront via a layer until all points of a bounding interface are crossed. The reflected wavefront can then be trailed via reinitialising FMM beginning at interface back to an incident section. The conveyed wavefront is then trailed through reinitialising FMM up to an adjacent section. Repetitive application of this technique permit phases consisted of any quantity of reflection and refraction branches to be trailed, without the need for explicit application of Fermat's Principle or Snell's Law.

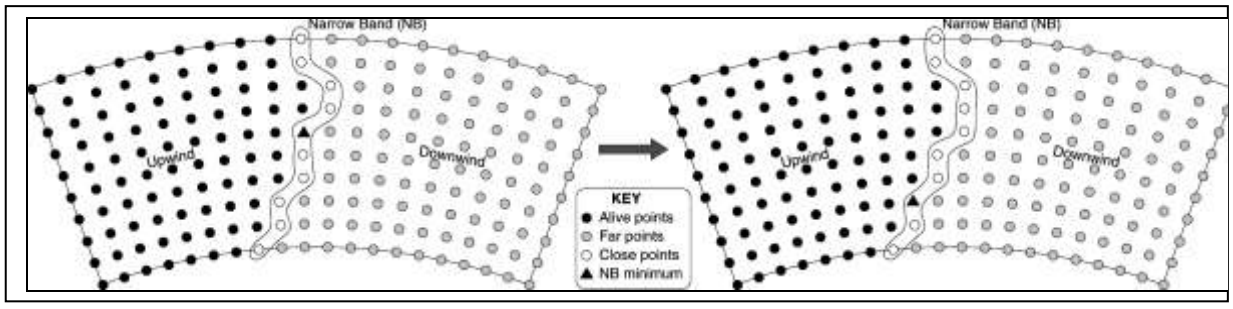

Figure 4.8: Theory of this narrow band technique for trailing this initial onset energy in unremitting media. Alive positions (upwind of the computational front) have accurate move-out duration (Rawlinson & Sambridge, 2004a, 2004b)

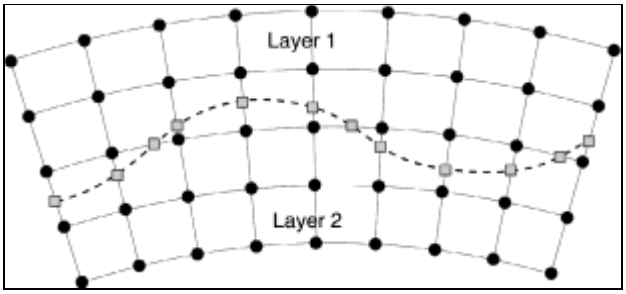

Figure 4.9: Two dimension displays on relationship between interface joins (grey squares) as well as speed joints (black nodes) via sectioned medium (Rawlinson, 2004a, 2004b)

FMM scheme (De Kool, 2006) solved move-out duration calculation at a range of scales in 3D spherical coordinates. It is able to trail several bouncing rays beginning at one boundary, for example, global PP phase, and P-S conversions at the boundaries. Sethian & Popovici, (1999); Chopp, (2001); Popovici & Sethian, (2002) and Rawlinson (2004a, 2004b) employ the following upwind operator scheme:

$$[\max(D_a^{-r}T,-D_b^{+r}T,0)^2\max(D_c^{-\theta}T,-D_d^{+\theta}T,0)^2\max(D_e^{-\Phi}T,-D_f^{+\Phi}T,0)^2]^{0.5}_{i,j,k}=S_{i,j,k} \qquad 4.10.$$

Here above, equation 4.10, i, j, k represent grid augmentation changeable on all orthogonal coordinate scheme r, θ, Φ as well as integers which are changeable a, b, c, d, e, f that delineate order of correctness of upwind finite disparity operator applied on every one of the 6 scenarios. Here, r, θ, Φ, stand for globular coordinate scheme, first 2 gradient operators on all of 3 routes are given as follows:-

$$D_1^{-r}T_{i,j,k}=(T_{i,j,k}-T_{i-1,j,k})/\partial r$$
$$D_2^{-r}T_{i,j,k}=(3T_{i,j,k}-4T_{i-1,j,k}+T_{i-2,j,k})/2\partial r$$
$$D_1^{-\theta}T_{i,j,k}=(T_{i,j,k}-T_{i,j-1,k})r\partial\theta$$
$$D_2^{-\theta}T_{i,j,k}=(3T_{i,j,k}-4T_{i,j,k}+T_{i,j-2,k})/2r\partial\theta$$
$$D_1^{-\Phi}T_{i,j,k}=(T_{i,j,k}-T_{i,j,k-1})/r\cos\theta\partial\Phi$$
$$D_2^{-\Phi}T_{i,j,k}=(3T_{i,j,k}-4T_{i,j,k-1}+Ti,j,k_{-2})/2r\cos\theta\partial\Phi \qquad 4.11.$$

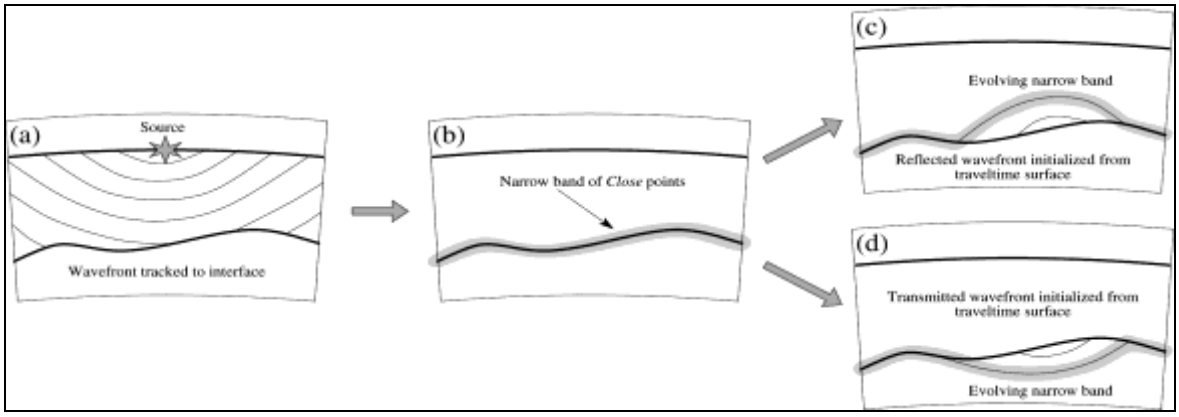

Figure 4.10: Theory explaining this Fast Marching technique. This incident wavefront is trailed to the entire positions on this wavefront, prior to re-starting of this Fast Marching technique (Rawlinson, 2004a, 2004b)

The kind of operator applied in equation 4.10 relies on the availability of the upwind traveltimes and the maximum order accepted. By default, a mixed order scheme may be applied which preferentially uses D_2 operators, but, reverts to D_1 if $T_{i-2,j,k}$, $T_{i,j-2,k}$, $t_{i,,j,k-2}$ is unavailable, for example, near a point source. Mixed order schemes applying higher order operator such as D3 are also applicable.

Equation 4.10 describes the finite difference scheme for updating the traveltime associated with a particular grid point. However, it does not specify the order in which points are to be updated. To gratify causality, entire arrangement ought to be consistent with the direction of information flow. That is, from smaller to large values of T. Fast Marching scheme attains this via systematically constructing traveltimes in a downwind fashion from known values upwind, using a narrow-band way (fig. 4.8). Close positions possess trial traveltime values that become alive when they are global minimum values of the entire close positions. When this occurs, the narrow band is locally evolved to retain the division of the traveltime time field into alive and far positions. As a result, the shape of the narrow band estimates the shape of the initial onset wavefront. The idea is to propagate the band throughout the grid until all positions become alive. The application of a heap-sort algorithm means that Fast Marching Technique possesses an

operation time (count) of O(NlogN) where N is the total number of grid positions. Hence, the computation cost and efficiency scales with grid size.

The dominant inaccuracy in FMM work out is accumulated in the origin neighborhood due to elevated wavefront curvature (Rawlinson & Sambridge, 2004b). Rawlinson & Sambridge, (2004b) illustrates that accuracy can be greatly increased without significant computation cost. This should be through introducing a refined grid in the origin vicinity, which is resampled to the global coarse grid. This is so because the narrow band reaches the refined grid boundary. The scheme is applicable in both three dimension and two dimension multi-stage versions. Typical values of the refined grid are amplification in resolution by a factor of either five or ten. Subsequently, a refined grid, extending fifty nodes away from the origin in each direction, is attained. When wave transmission transpires in a layered medium with undulating interfaces, the margin of each speed continuum might be rough. To deal with it, Rawlinson & Sambridge, (2004a&b) apply the adaptive triangular meshing system on the whole neighborhood of every interface to link interface nodes with adjoining speed nodes. Interface nodes should be delineated via the position of intersection between the interface surface as well as the grid lines of the speed mesh (figure 4.8). Wavefronts are then spread throughout the irregular grid using a first-order version of the equation 4.10 for triangular elements which is comparable to a plane wave estimation. In three dimensions, an adaptive tetrahedral mesh ends up being harder to execute. Hence, updates to interface or surrounding speed nodes are made through considering impinging plane waves from all possible amalgamations of adjoining alive speed as well as interface nodes. Here, right wavefront direction produces the minimum onset duration (De Kool, 2006). Thus, theory underlying the FMM way is illustrated in figure 4.9. A wavefront is trailed from origin until the entire interface nodes turn into alive. The entire alive positions are then reset to close and FMM is reinitialised into the incident section for a reflection. The scheme is reinitialised into the adjacent section for the case of refraction. This can be repeated any number of times to construct phases comprising any number of refraction or reflection branches. Conversions between P and S waves can be trailed simply through replacing the incident or adjacent speed field with the appropriate P or S wave-speed representation before reinitialisation of FMM. Beam routes for phase types are established a posteriori through integrating along the move-out duration field gradient from the sensor back to the origin.

A P phase converted to P phase cannot be trailed using FMM because it entails successive interactions with the same interface. It no longer represents the interface-intersecting global minimum onset inside the section. PP phases can be worked out through starting FMM from both the source and receiver and then trailing the consequential wavefronts to a common interface. Here, whole phase is attained through matching the entire move-out duration gradients from the two impinging wavefronts at the interface. Where the wavefronts are equal in magnitude and converse in sign corresponds to a valid reflection position. This approach also allows manifold later-onset reflections from one interface to be obtained if such phases exist. The limitation on getting these groups of later onset phases means that FMM ought to initiate beginning at origin up to sensor position. Consequently, this initiation escalates the working out duration.

Trailing wavefronts from point source using FMM within the representation volume can also be initialised from a long distant wavefront. It's accomplished by working out move-out duration beginning at far origin ending at border of entire representation. In some instance this is possible through applying a global reference model which is acceptable. Initialisation of distant wavefront beginning at border of the model is established in the same manner as from an interface. The alive grid positions are set to close and the narrow band evolves from the position with minimum move-out duration. Thus, P, PcP and PkiKP phases can be trailed via the local model using these approaches in distant tomography (Graeber et al., 2002 and Rawlinson et al., 2006b).

4.3 Inverse theory for Invert3d; LU Decomposition for Matrix Inversion

In linearized systems, one aspires to work out Ax=b for numerous dissimilar vectors b. Gaussian elimination with pivoting is one of the many techniques which are efficient and accurate in solving linearized systems. The majority of the effort in this technique is exhausted on the matrix A. Since the matrix of A is big, shun redoing the procedures of Gaussian eradication in matrix A belonging to each dissimilar vectors b. It should be established through entire LU disintegration that on effect documents entire steps of the Gaussian eradication. In general, whole major thought of entire LU disintegration is to document entire steps applied on Gaussian

eradication in matrix A on entire positions wherever 0 ought to be formed. Consider a simple matrix A shown in equation 4.12a below for purposes of ease in demonstration:-

$$A = \begin{matrix} 1 & -2 & 3 \\ 2 & -5 & 12 \\ 0 & 2 & -10 \end{matrix} \qquad 4.12a.$$

The initial procedure of Gaussian elimination should be deducting twice entire initial row from whole subsequent row two. So as to account for whatever has been completed, place entire multiplier, 2, at exact position it has been applied to create 0, that is, entire subsequent row two, initial column. So as to make it clear that it is a record of the step and not an element of matrix A, have it enclosed using parentheses. There exists a zero in the lower left corner, so there is no need of eliminating any portion. Account for these details with a zero (0). So that we eradicate entire row three, column two, deduct minus two times whole row two from entire row three. Documenting the -2 on the point it was applied, the matrix becomes:-

$$\begin{matrix} 1 & -2 & 3 \\ (2) & -1 & 6 \\ (0) & (-2) & 2 \end{matrix} \qquad 4.12b.$$

Allow U to occupy upper triangular matrix produced, and allow L to take up lower triangular matrix with documented information and ones in the diagonal, that is:-

$$L = \begin{matrix} 1 & 0 & 0 \\ 2 & 1 & 0 \\ 0 & -2 & 1 \end{matrix} \qquad 4.13$$

and

$$U = \begin{matrix} 1 & -2 & 3 \\ 0 & -1 & 6 \\ 0 & 0 & 2 \end{matrix} \qquad 4.14.$$

Then the resultant property is as follows:-

$$LU = \begin{pmatrix} 1 & 0 & 0 \\ 2 & 1 & 0 \\ 0 & -2 & 1 \end{pmatrix} \begin{pmatrix} 1 & -2 & 3 \\ 0 & -1 & 6 \\ 0 & 0 & 2 \end{pmatrix} = \begin{pmatrix} 1 & -2 & 3 \\ 2 & -5 & 12 \\ 0 & 2 & -10 \end{pmatrix} = A \qquad 4.15.$$

Thus, A is in fact the multiplication of L and U. At this point, L should be lower triangular as well as U as upper triangular. The matrix A is expressed as multiplication of simpler matrices.

This is the disintegration of matrix A which is referred to as LU decomposition. Pivoting is included while using LU to solve linearized equations. As a result, the LU disintegration for matrix A is composed of 3 parts P, L and U as follows:-

$$PA=LU \tag{4.16.}$$

Thus the pivot matrix P should be the identity matrix, having matching rows exchanged as entire rows of A are exchanged in the pivoting. That is:-

$$P = \begin{matrix} 1 & 0 & 0 \\ 0 & 0 & 1 \\ 0 & 1 & 0 \end{matrix} \tag{4.17.}$$

Hence, P matrix above would be entire pivot if the rows two and three of A are exchanged via pivoting. To use pivoting to work out Ax=b we initial pivot all sides of Ax=b through multiplying via entire pivot matrix:-

$$PAx=Pb=d \tag{4.18.}$$

Exchanging LU for PA one attains:-

$$LUx=d \tag{4.19.}$$

This delineate y=Ux, that should be unknown since x is unknown. Applying forward-substitution, effortlessly work out for y as follows:-

$$Ly=d \tag{4.20.}$$

And then using back-substitution, effortlessly workout for x as given below:-

$$Ux=y \tag{4.21.}$$

In Invert3d routine written in Fortran 90 language, this works as follows using luinv (subdim, mati) sub-routine which is also written in Fortran 90 language:

```
! Calculate the model perturbation
r1mat=0.0
DO i=1, subdim
DO j=1, npi
r1mat (i) =r1mat (i) +a (j, i)*gamma (j)
ENDDO
```

```
ENDDO
r2mat=0.0
DO i=1, subdim
DO j=1, subdim
r2mat (i) =r2mat (i) +mati (I, j)*r1mat (j)
ENDDO
ENDDO
dm = 0.0
DO i=1, npi
DO j=1, subdim
dm (i)=dm(i)+a(I,j)*r2mat(j)
ENDDO
dm (i)=dm9i)+a(I,j)*r2mat(j)
ENDDO
dm (i)=-dm(i)
ENDDO
DEALLOCATE (a, gamma, dtrav)
DEALLOCATE (ga, mati)
IF (asds.EQ.1) THEN
DEALLOCATE (dem, smv)
ENDIF
END SUBROUTINE
```

Consequently, one can work out for any other vectors of b without repeating the LU procedure. This is a big saving since the matrices involved are large within actual application packages.

5. MATERIALS AND METHODS

5.1 Materials

The materials have been divided into: (a) secondary data and (b) primary data. The primary data sub divisions include: (i) equipment, (ii) field data and (iii) software. They are described as follows:

5.1.1 Secondary data

The secondary data used was raw micro-seismic data acquired using a network of fifteen seismological stations collected by Ibs-von Seht et al., (2001). The data covers period of eight months; from November 1997 to June 1998. From a data of seven hundred and twenty one events, only four hundred and ninety six were considered as good enough for tomographic process.

5.1.2 Primary data

The primary data used was raw micro-seismic data acquired using a network of forty seismological stations collected by Roecker et al., (2017). The data covers period of two years; from January 2013 to December 2014. This network covered northern Tanzania and southern Kenya well known as crafti project. From a data consisting of the entire set of crafti events, only a sub-set containing six hundred and ninety events whose ray paths covered Magadi was considered as good enough for this work's tomographic process.

5.1.2.1 Equipment

40 Guralp – model CMG-3T seismometers were installed and measured the seismic signal by the high resolution digitizer. Data from these sensors was recorded by the Quanterra Recorder, model Q330. The best installation sites were chosen based on areas with low ambient noise, dry, in a dug-hole for stable year-round temperature and good bedrock. All sensors were covered by a pvc buckets for extra temperature insulation and stabilizing debris round the sensors. Data was

collected for two years at the sampling rate of 40 and 200 samples per second. The data was downloaded to a processing PC for analysis.

5.1.2.2 Field data

Field data was raw micro-seismic waveforms. This data of passive events contained unfiltered ambient noise from nearby sources. Before this data was used, ambient noise from nearby sources was filtered to make the data fit for further processing.

5.1.2.3 Software

Softwares were used to accomplish the entire travel time seismic tomography process in seven major steps. These steps included location, relocation, seismicity map, forward problem, inversion, 2D slicing and slices' display. The steps are discussed as follows:

5.1.2.3.1 Location and 1D inversion

Seisan software was used to execute the initial phase picks. A starting 1D velocity model was created. The P-velocity values were taken from laboratory values for various rocks known to exist in the study area at varying depths and used as the starting 1D velocity model for the events location process.

5.1.2.3.2 Relocation

Relocation of events was done in two fold. First by seisan software and then by tomo3d routine and the two results compared. Seisan was used to relocate events through establishing final 1D inversion model and replacing the velocity model in the first location with it. Once this finished, a fresh location was done and improved hypocenters obtained.

Relocation in tomo3d routine was achieved through establishing three dimensions P-velocity model using the final one dimension inversion result. Then, the 3D model was improved by running several iterations in the inversion process using observed data. The improved 3D model was then used in tomo3d to carry out source inversion works.

5.1.2.3.3 Seismicity of study area

Seismicity of study area was created using excel spreadsheet, Google Earth, QGIS and ArcGIS softwares. This was possible by first creating a comma delimited excel file (csv) and importing to both QGIS and ArcGIS softwares. This imported data was then used to create a point shapefile to represent events. Fault lines in the study area were extracted from updated Google Earth software. This data was imported in QGIS and ArcGIS and then used to create line shapefile. The lake Magadi and Little Magadi were extracted from updated Google Earth software and then this data imported to QGIS and ArcGIS and then it was used to create polygon shapefile. When all required items were ready, the line shapefile was overlaid on the polygon shapefile and point shapefile representing events overlaid on the line shapefile and made a seismicity map. This map was then refined by adding labels to the features it contained, a north arrow, scale, title, grid in degrees and a border line.

5.1.2.3.4 3D Forward problem

The 3D forward problem was accomplished using fm3d sub-routine controlled by the tomo3d parent-routine. This enabled generation of the predicted travel times using the starting 3D velocity model before inversion could take place. All this data was stored in arrivals.dat file which later is renamed mtimes.dat to represent starting model travel times. This mtimes.dat file is a requirement before inversion is executed.

5.1.2.3.5 3D Inversion

The 3D inversion was achieved using invert3d sub-routine controlled by the tomo3d parent-routine. This enabled the adjustment of the starting 3D velocity model to fit the observed data. Six iterations were run to ensure that uncertainties (misfits) were reduced to as low as possible to make the final 3D velocity model acceptable based on available data.

5.1.2.3.6 Slicing the final 3D P-velocity model

Gmtslice sub routine of generic mapping tool (GMT) was used to slice the final 3D P-velocity model E-W and N-S directions ready for display. The display was done by generic mapping tool (GMT) scripts. These scripts were plotew and plotns.

5.1.2.3.7 Slices' display and final 1D velocity model

Two dimension slices generated by gmtslice sub-routine were displayed by generic mapping tool scripts. These scripts were plotns and plotew. This was possible by conversion of gmtslice output from grid2dvew.z format to grid2dvew.grid format using xyzgrid sub-routine in generic mapping tool which is then displayed using grdimage sub-routine. The interfaces, ray paths, sources and receivers in intew.xy, raysew.xy, sourcesew.xy and receiversew.xy data files are overlaid on the two dimension image by psxy sub-routine in generic mapping tool software.

The final 1D velocity model was displayed through the use of the excel spreadsheet display option. Grapher was very vital in enhancement of the visualization by clearly showing the variation in distribution of hypocenters and aspects of velocity.

5.2 Methods

5.2.1 General

Raw micro-seismic data for Magadi trough was examined. The events were filtered to remove the noise. Phase picking was done to enable the location and determination of travel times. Amplitudes were established to aid in calculation of the event sizes. Hypocenters were identified through automatic event location. The collect and select out-put files were created. They were later developed and converted to data.cnv formats for use in the velest programs. This was meant to fit the observed data apart from giving the most probable and reliable subsurface parameters. Initial near true guess crustal models were made. They were later perturbed by the velest program in the process of fitting them to new values. These new values were adjusted until they matched the observed micro-seismic data. Inversions were run repeatedly in order to get the best velocity variation with depth. Finally, plot scripts were edited in order to display the results. The 1D final velocity model was constrained further by output of works done by Mulumbu, (2015). This was used as starting model for the 3D inversion. Constant gradient Cubic B-spline was used to interpolate the starting 1D into a 3D starting model with velocity varying only with depth.

5.2.1.1 Fieldwork

Fieldwork was carried out for a period of two weeks. The major task was to ascertain the geology of the study area through observation. It was very necessary for us to check and confirm that the sites chosen during desk study were really suitable for installations of equipment. All unsuitable sites were relocated to reliable site based on easy access to good bedrock for holes, relatively quite areas and of good security for installation of equipment.

5.2.1.2 Analysis of data

Raw micro-seismic data in form of waveforms were downloaded bi-annually from the Guralp equipment to PC for a period of two years. Then seisan software was used to display the data and quality control and analysis in order to exclude any existing ambient noise in the data before further analysis and processing.

On successful completion of quality checks, acceptable starting 1D velocity model was created and then the events were located. In order to improve on hypocenter parameters the events were relocated using both seisan and tomo3d software packages after improving the velocity model to a more reliable one. Travel times data from well located hypocenters were then used for the final 3D inversion process to get the crustal structure of Magadi area.

5.2.1.3 Interpretation of data.

The hypocenters and epicenters of well located events were characterized based on the distribution both laterally and vertically. The meaning of such distribution was vital in understanding the magmatic and tectonic dynamics of the study area. The seismicity map for the epicenters was presented as a two dimension horizontal plane while the hypocenters were displayed in form of two dimension vertical section. These displays were meant to enhance the visual impression of the results.

On the part of 3D inversion, the results were displayed in form of two dimension slices sliced from final three dimension velocity model. The key aspect taken to consideration during the interpretation was if any velocity variation existed and the geological/geophysical meaning of such variation.

5.2.2 Phase picks and location analysis

An overview of the way phase picks and location is done using seisan has been summarized by Ottermoller (Ottermoller et al., 2008-11). In this study, waveforms of the events were displayed. They were inspected for the noise which causes inaccurate analysis if allowed in events location. Then appropriate and reliable filter was used to filter out noise with a range between one and five hertz (1-5Hz). The phase onset points for both p and s phases on the waveforms were then precisely identified. They were picked alongside maximum amplitude determination. This was possible via picking the lowest and highest points of the largest amplitude of the waveforms. Coda points were also picked by placing the cursor on the point where there is complete attenuation of the waveform amplitudes. This was followed by pressing c-key while pressing down the control key. The location button on the seisan waveform display menu was pressed to determine the location parameters. The residuals between the observed and calculated move-outs were then keenly analyzed for each event. Phase picking was re-done severally to ensure that the residuals were suppressed to allowed minimums of less than 0.05 seconds. Once, all the events had been re-located severally to ensure the residual minimum value mentioned was achieved, then the x y z coordinates were recorded on excel sheets. This data was saved as comma delimited (csv) for further processing.

5.2.3 Creating input files

The process for both collect and select files is the same. Reliable range of input parameter values was appropriately chosen. This composed of data in the database to be used, type of base, start and end time of data. Apart from fault plane solution, earthquake felt, magnitude types, distance IDs, event IDs, magnitude limits, latitude and longitude limits, the input parameter values also included depth limits, RMS limits and number of stations limits. The hypocenter errors, latitude limit, longitude limit, and depth limit were vital in the parameterization. Though of lesser importance, minimum number of polarities, hypocenter agencies, magnitude agencies, station codes, components, distance range, phase, polygon, use of all header lines, look for wave form file names, gap range, phases and volcanic subclasses were also not excluded.

All the above were determined and re-determined severally to get reliable values by selecting their respective numbers in order to change existing parameter values. Once the values were

acceptable, the enter-key was pressed twice to allow automatic creation of out-put files called either collect.out or select.out depending on the initial command of either collect or select, respectively. These files were input data in the inversion process but had to be converted to data.cnv format first before being accepted into the velest program.

5.2.4 Creating velest control files

First, once velmenu options display is on the seisan display window, the parameter control file option which is the first option is chosen by typing 1 on the command line and pressing enter-key. A notepad file is displayed with options for interactive input of reliable values as per the data being used for the inversion. For this work, the set data was put at 771 while the subsets of data were put at 118, 222 and 471 with each yielding a different inversion output result at a time. The depth shift was put at 0.900 for stations with average height above the sea level of about 900 meters; the average station height above sea level for Magadi stations was 757 meters. The number of shots was put at zero. This was so because no shot was used. The inversion was to be run in a continuous mode hence the mode was set at 0 to achieve this. The maximum epicentral distance was set between hundred and two hundred kilometers with velocity and depth adjustments set at 0.2 and 5, respectively. In order to achieve the use of move-out duration in the inversion, number of phases (nsp) was set at 2 to get the dissimilarity between the onsets of p and s phases. The p velocity s velocity ratio of 1.74 with a minimum velocity guess model of 1. In addition to this, the inversion ratio was set at 1 which ensured that every inversion was of type A invert for all hypocenters and model.

5.2.5 Creating station files

The velmenu command option 3 allows for creation of a list of seismological stations used during the seismic data acquisition. The station file is highly interactive. Hence, elimination and addition of stations can be achieved through interactive editing of the station. The editing is then saved to effect the changes during the inversion.

5.2.6 Creating guess model files

In the seisan software, the velmenu command option 5 is executed to create inversion control files. The number of layers created, depends on the conditions which are prevailing in the area of

study. Their respective initial velocity values assigned is improved by using values from a long seismic line survey using high magnitude explosives to achieve greater depths into the subsurface. These values which can be attained through refractive survey lines tend to be near true values. They are then highly dumped to ensure that they are not perturbed or adjusted so much during the inversion in order to attain high degree of accuracy of the inversion out-puts. The amount of sections used in the representation files is specified on the starting row for easy identification by the routine during the inversion process using the seisan software. Here, the thicknesses of the layers increased with depth to deeper areas of the subsurface.

5.2.7 Creating 1D inversion out-put files

In the velest menu, the A command option is chosen to execute the action of velest program. Automatic format conversion is done to suit the requirement of the velest program. In this conversion, the stationx.hyp format is converted to station.sta format, while, select.out format for the seismic data input is converted to the data.cnv format which is acceptable by the velest program. In the process of the inversion, the option is given to either relocate velest input with hyp or not to, in this inversion, relocating velest input with hyp was chosen in order to enable the comparison between the computation of velest and hyp. Many inversion runs are carried out to increase the suitability of the out-put. In this work, both 3 iterations and 13 iterations were used to ensure good determination of their effectiveness. The first thirteen iterations were taken to achieve convergence of entire inversion process to universal smallest solution with RMS having a value which is less than 5.

5.2.8 Display of epicenters, hypocenters and inversion out-puts

The epicenter and hypocenter display is achieved through the use of EPIMAP, Google-Map and HYP. They are enabled and executable in seisan. Here, internet access is required to display the information on Google maps. However, for this research work, display of epicenter comes first by creating an excel sheet having the epicentral coordinates and saving in comma delimited format. This file is then imported into QGIS or ArcGIS and evenly displayed event epicenters are then displayed on this GIS display window. Grapher was used, apart from tomo3d, to display the hypocenters and their variation in the selected study area. First, the x y and z values of all events are recorded on a new sheet in Grapher and saved. This sheet is then used to plot the z values and show their distribution using the Grapher software. The gradational colors are used to show the

shallow events and also the deep events. A legend is given to show the contrast in the variation of depths through use of varying colors. And finally, the display of the change in velocity with depth, from a point on the surface downwards was achieved via the use of the Microsoft Excel graphs. Here, values from the invers.out file were recorded in excel and then graphs plotted to show the variation of velocity with depth using one dimension (1D) inversions which later was a means of constraining the 3D travel-time seismic tomography.

5.2.9 Developing 3D seismic tomography

A new Fast Marching Method Tomographic inversion scheme (FMM) was used. It has been designed for the three dimension seismic inversion of local earthquake datasets. The essential novelty of the method should be the application of the framework based Eikonal solver, called entirely fast marching method (Rawlinson et al., 2004a&b) to solve the forward problem of move-out duration forecast. In 2006, De Kool and others developed a multi-stage FMM on three dimensions globular coordinates. It accepts phases including all amount of refraction plus reflection divisions. They are then trailed in non-homogeneous sectioned mass having undulating edges (De Kool, 2006).

A variety of onsets, comprising reflection manifold, transformed waves, confined event phases plus long distant phases could be worked out via complex formation like subduction regions. Thus, work out effectiveness plus strength of entire multi-stage Fast Marching technique enable it to be very appropriately applicable in huge Tomographic challenges. This iterative non-linear inversion technique accepts speed, boundary depth plus origin position factors to be inverted. But for this study, only velocity parameters were inverted for. Each stratum is separately delineated by a three dimension even framework of speed nodes, having cubic B-splines applied in illustrating a smoothly changeable speed field. Similarly, each stratum margin is separately delineated by a two dimension framework of boundary depth nodes, with cubic B-splines applied in producing a smoothly changeable surface.

The subsurface inversion technique comparable to that applied by Rawlinson and others was used to work out the inverse challenge of modifying representation factors to superiorly gratify data observations conditioned by regularization constraints (Rawlinson et al., 2006b). Both

damping and smoothing are applied producing suppressed result non-uniqueness. Several inversions were carried out having dissimilar degrees of damping plus smoothing aimed at making out entire representation possessing smallest adjustments plus coarseness which still gratifies the recorded observations within allowable levels. This multi-stage technique plus subspace technique were used iteratively so that this non-linear character of entire present inverse challenge is dealt with.

5.3.0 Location of sites used for installation of seismometers (sensors)

A map developed to display the portable stations which were used during the 1997-1998 study is shown by figure 5.1 below. It represented the fifteen mobile seismological stations used and had covered an area of about 5000km^2. These sensors included digital lennart pcm fifty eight hundred schemes documenting data in a magnetic tape with sampling frequency of 100Hz and anti-alias cut-off of 25Hz. The 2013-2014 crafti project stations composed of 40 Guralp seismometers. They were distributed all over northern Tanzania and southern Kenya. Figure 1.3 shows their location.

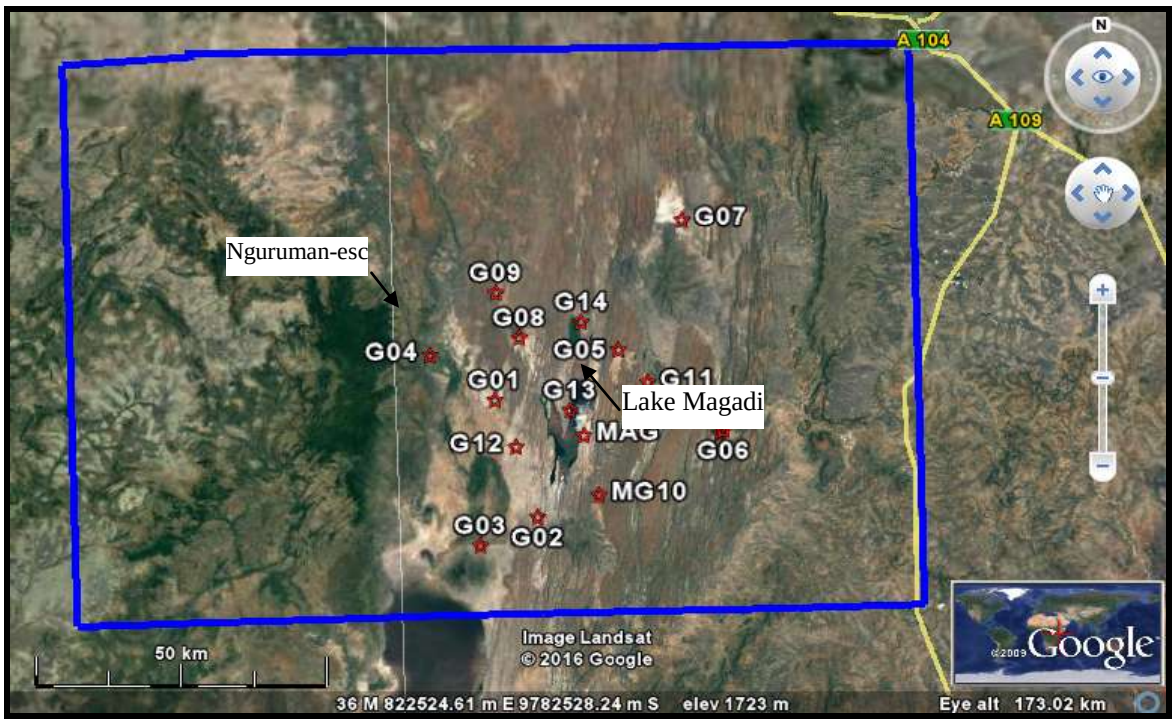

Figure 5.1: Red stars-mobile seismological stations, blue line-study area (coord: 1.1 ^{0} S to 2.2 ^{0} S and 35.5 ^{0} E to 36.8 ^{0} E)

5.4.0. Study flow-chart

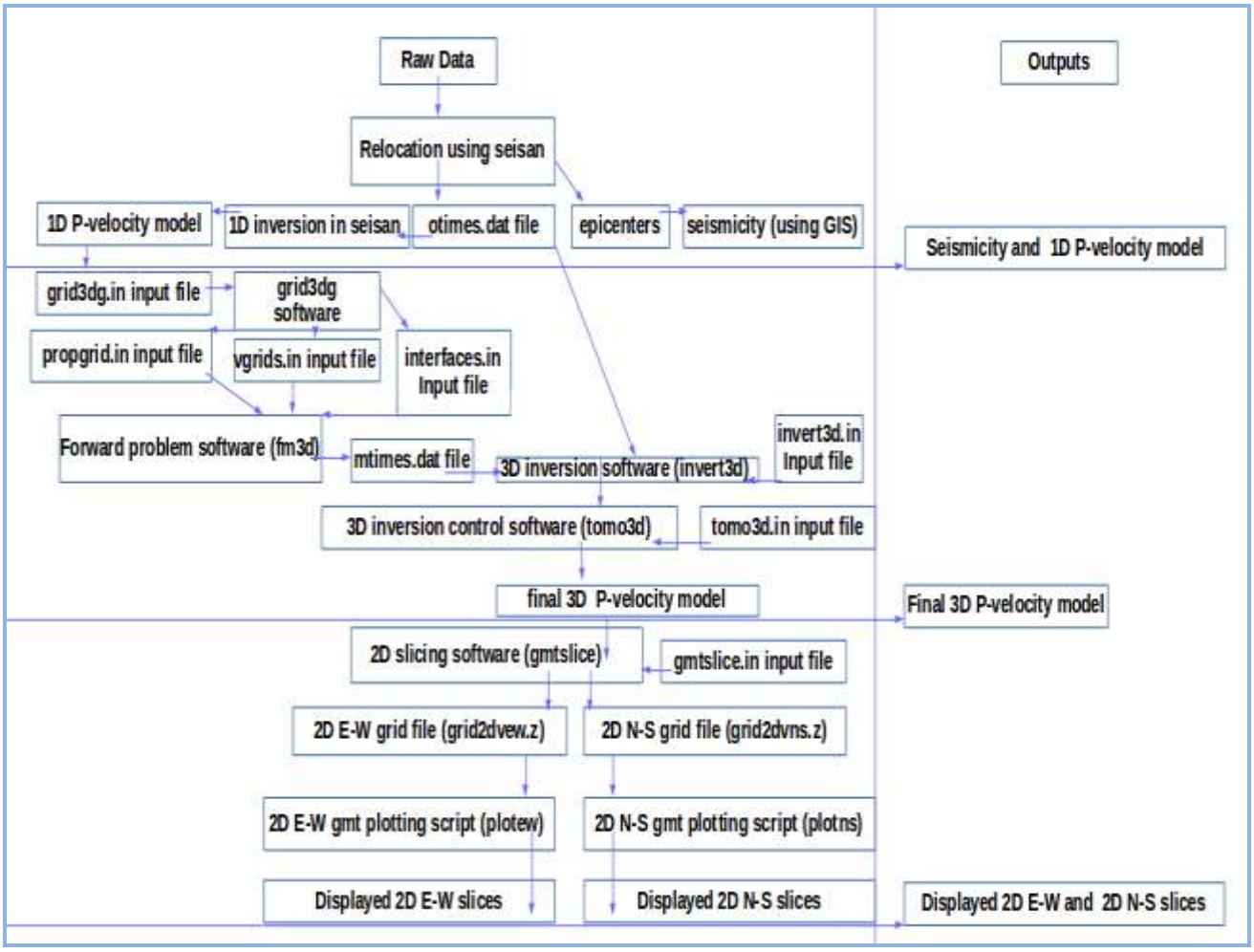

Figure 5.2: Study flow-chart

Figure 5.2 above shows flow chart for this study. First, at the initial stage, raw-data (waveforms) were processed using seisan software. There were three outputs from seisan software: epicenters which were used to develop seismicity map, final 1D inversion model (one of the inputs in to the initial 3D velocity model apart from apriori information) and observed travel times (otimes.dat) including their uncertainties.

Then, grid3dg.in file (parameters) constrained using final 1D velocity model and apriori information from near surface weathered crustal layers in form of low velocity zone (Mulumbu, 2015) was used as input into grid3dg software in order to produce three fm3d input files: propgrid.in, vgrids.in and interfaces.in representing 3D propagation grid, 3D velocity grid and 3D interfaces grid respectively.

Furthermore, initial 3D velocity representation was applied to relocate earthquakes before using them in the 3D inversion process. Further, the fm3d software was used to track wavefronts in 3D propagation grid and subsequently produced computed traveltimes (mtimes.dat) with vgrids.in file as the initial 3D velocity model.

Finally, an inversion loop was created. This was possible by ensuring invert3d software adjusted the initial 3D velocity model. Then, newer 3D velocity model was developed. Better mtimes.dat was established and subsequently adjusted to further better level till observed traveltimes were well fitted by the final 3D velocity model (3D invmo). The entire loop process (iterations) was controlled by tomo3d software. The final 3D velocity model was then sliced using gmtslice software. The grid2dvew.z and grid2dvns.z files were produced. They were displayed using gmt-plotting-scripts.

6. DATA PROCESSING, SEISMIC MAPPING AND DATA INPUTS-3D INVERSION

6.1 DATA PROCESSING

6.1.1 Importing data and automatic registration

The raw waveform data was imported into the Seisan software. Its windows display shown in figure 6.1. The necessary folders were created through the MAKEREA command. Once the command was executed, a 1-5 letter base name was requested and written in upper case. The start time and end time were given. In the process both WAV and REA were created. The waveform files were automatically registered through opening the folder with the waveforms, listing the files using the DIRF command and executing the AUTOREG command. An example of the DIRF command output is as follows in table 6.1.

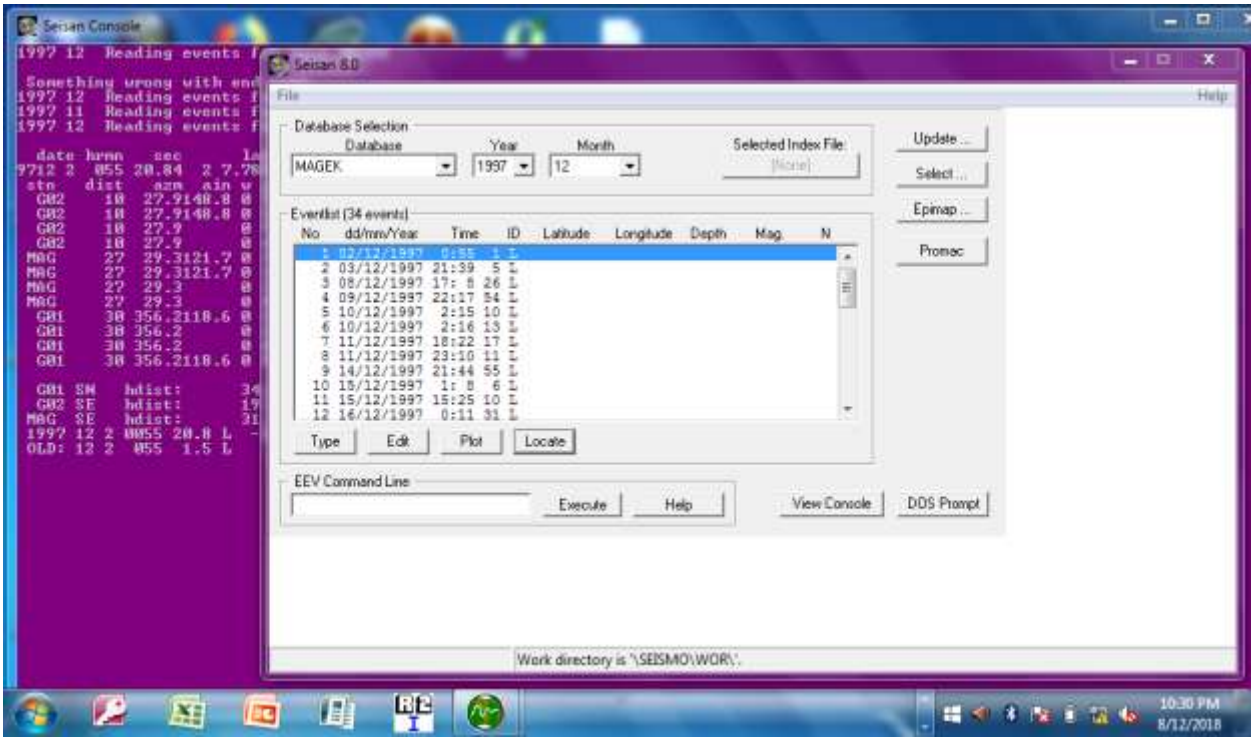

Figure 6.1: Windows seisan display of 1997-1998 events list

Table 6.1: An example of DIRF command output

Number	S-File
#1	98060709.M58
#2	98060720.M24
.	.
#1177	98061320.M03
#1178	98061323.M38

Such steps give access to the waveforms and this was possible through the use of CD, DIR, DIRF and MULPLT commands in Seisan.

6.1.2 Checking for data quality

All the waveforms were analyzed to check if there were data quality concerns in the recordings. Available components were: vertical (Z), north-south (N) and east-west (E). The necessity of using azimuth in event location for events which had two components only was also determined.

6.1.3 Merging of components and events Registration

The SEISEI command was used to merge separate component entities like vertical and the two horizontals components together. This was possible if the three components which were to be merged were for the same event. Events were registered in the database using Autoreg.

6.1.4 Displaying the waveforms

In order for the waveform to be displayed, the MULPLT command was executed after the DIRF command listed the S-files. When MULPLT command was executed, the file number was inserted. Different plot options were given. Default option, "0", was chosen. Low filter option was inserted and when this option was entered, all the waveforms in the first file were displayed (fig. 6.2). The same procedure was carried out for all the other consecutive files.

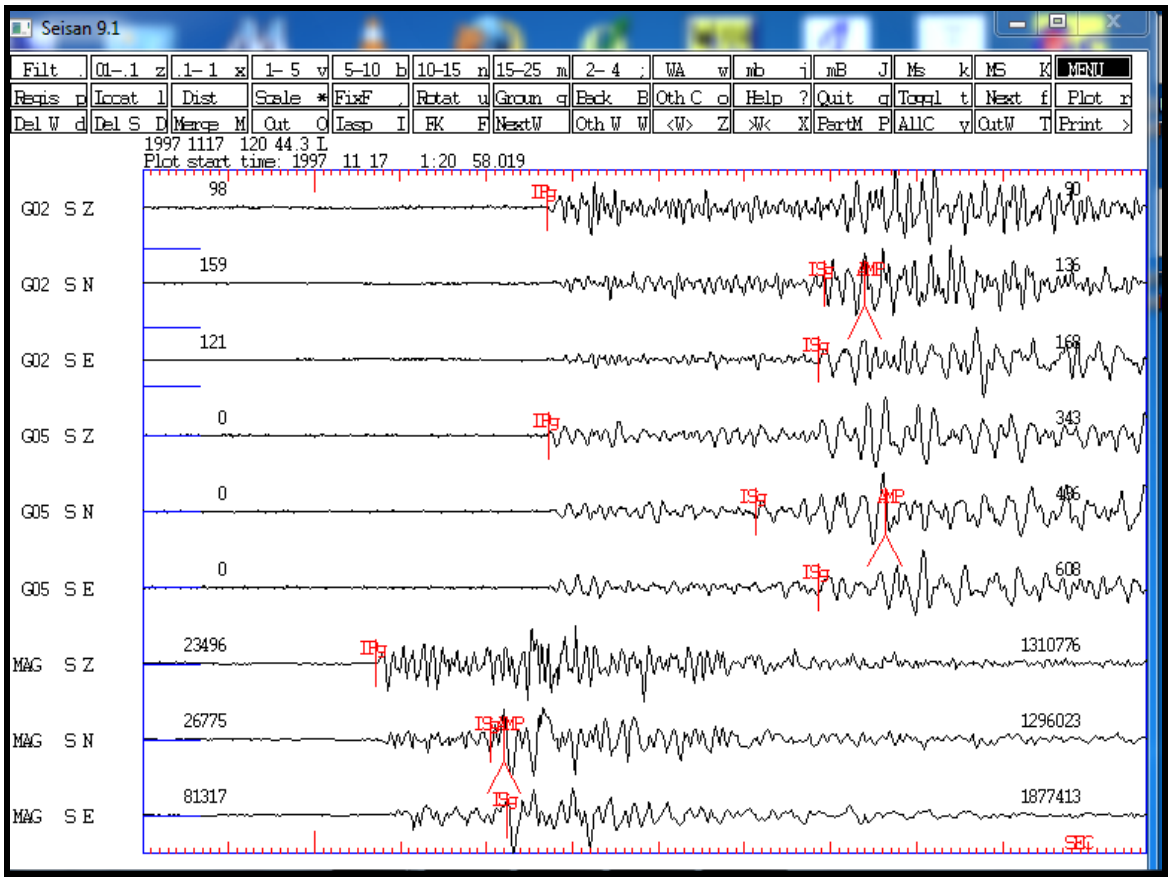

Figure 6.2: Example of displayed analyzed waveforms

6.1.5 Filtering, phase picking process and magnitude determination

The filters which were available in the seisan software menu were: 0.01-0.1 Hz, 0.1-1 Hz, 1-5 Hz, 5-10 Hz, 10-15 Hz, 15-25 Hz and 2-4 Hz. The 1-5 Hz low pass filter was helpful on entire micro seismic information processing. This was so because it was used to filter more than half of all the waveforms considered in the whole exercise. The 25 Hz high pass filter was used for the rest of the high frequency noise. The letter z or v and other alphabetical letters alongside the filters represented keyboard buttons which were pressed to execute them. Practically, this meant that most of the signals were controlled by noise ranging between 1 Hz to 5 Hz and few by 25 Hz. When the filter was applied, the phase arrivals became sharp and easily picked unlike unfiltered waveforms which still had ambient noise. P-phase and S-phases arrivals were singled out on the vertical and the two horizontal components respectively. Travel times were found by finding entire disparity of entire onset duration between the P-phase and S-phase. Distance of the

event source was manually given by the product between the travel time and the average velocity estimate for the study area.

Most of this work was done automatically by the seisan software by using the LOCAT command. The phase picking process was repeated over and over again till about 631 events were fully covered and finished. Magnitudes were calculated using the software by clicking at the bottom and top ends of the highest amplitudes of the waveforms of the horizontal components. Options menu for the different types of amplitude determination appeared and first option was chosen for all the waveforms under consideration. Furthermore, yes (y) or no (n) options were availed every time the amplitudes were to be determined. In order to effect the amplitude determination permanently, the yes (y) options were chosen and the amplitudes were fully registered on the horizontal components of the waveforms. Similarly, this was done for all the waveforms under consideration in the study.

6.2.0 Developing an Initial Model using Apriori Information

6.2.1. Standard Rock Velocities

The initial guess model was developed through the analysis and examination of a variety of the literature values obtained by different field tests carried by scientists or engineers while carrying out tests or execution of a myriad of laboratory tests on the rock materials. The velocity estimates for the primary waves variation for the least dense materials like water, ice and clay range from values as low as 300 meters per second to a high of 900 meters per second. The densest materials like gabbros, granite and diorites range from 5000 meters per second to 8000 meters per second. It has also been established that the P velocity and S velocity have a correlation or relation such that the S velocity are one and half or twice the P velocity values. Hence, the velocity estimates for the secondary waves for the least dense material is 0 meters per second for fluids to about 450 meters per second for clay materials. The densest materials like gabbros, granite and diorites range from 3000 meters per second to about 5000 meters per second.

6.2.2 Velocity estimates using velmenu command

In order to use this command, collect.out file was prepared first. Execution of the command in seisan was done by typing the word collect on the MS-DOS command prompt and clicking on

the enter key. Base name request could appear and after providing the five character base name, start and end time of processed micro-seismic data under consideration was asked for. This was provided and (y) option chosen in order to continue with process and then come up with the collect.out files which were part of the outputs. Subsequently, the velmenu command in seisan was executed. File names for the processed earthquake data were given as input data in form of collect.out files. This process yielded velest menu which gave ten options. These options were as follows:-

VELEST MENU

i. Generate velest command file (velest.cmn)

ii. Modify/transform velest control folder

iii. Generate sensor pick folder

iv. Modify/transform station select file <selstat.lis>

v. Generate representation file

vi. Modify/transform representation file

vii. Execute velest

viii. Modify inversion result file

ix. Change velest result to Nordic format and construct diff-file

x. End

The first option was utilized in the creation of the velest command files. They were also referred to as the velest.cmn files. Such files were used together with the station select files and the model file to come up with the velocity estimates. They were in the velest.out and velout.smp files. To develop station select files and model file, third and fifth options on the velest menu were used. In addition to all this, the velest menu provided an option for editing all the created files. This was very crucial in case there were amendments to be made for all created files through the use

of velmenu command. The key amendments made were in the apriori information where a variety of initial model values were given to represent the various field situations.

6.2.3 Seismic Refraction Mapping and Data Inputs-for 3D Inversion

Mulumbu's survey (Mulumbu, 2015) involved using critically refracted arrivals assuming a flat layer model to determine the velocity including the width of the weathering layer at each station. The thicknesses and speed obtained are useful in delineating the extent of the low velocity layer suitable for determining static corrections necessary in a reflection survey devoid of anomalous effects of the low velocity layer. The data was collected using 1C-24 channel geophones of 10Hz at an interval of 3 km. The length of the spread was 108m long with a sledge hammer as a source of seismic waves. Data was recorded in SEG-Y format then transcribed to 2D/3D Vista seismic processing software for initial onset picking. Picked initial onset durations were put into spreadsheet where layers were picked and speeds worked out using time intercept method. In this study, near surface low velocity 300m/s to 900m/s from work done by Mulumbu (2015) were used. This was together with available final 1D velocity inversion result for restraining entire initial representation for three dimensions seismological tomography. It was possible via using the First Marching Method (FMM). Results were used for the final interpretations aimed at addressing the research objectives. Data inputs for 3D inversion included interfaces.in, Vgrids.in, propgrid.in, sources.in, receivers.in and frechet.in. In addition, ak135.tbl and ak135.hed input files are standby. They are included if teleseismic sources are incorporated in local seismic data. The iterative use of the multistage Fast Marching technique plus entire subspace inversion technique accounted for entire non-linear link to travel-times, wave-speeds and interfaces depth perturbations with damping parameter (epsilon) of ten plus smoothing parameter (eta) of five. The inversion also included damping regularization which penalized result representations that were strongly adjusted from the original (starting) representation. A total of 12321 nodes described the entire three dimensions velocity continuum.

7. RESULTS

The results of the analysis are divided into six parts. These parts include: (1) seismicity of Magadi area, (2) 1D P-velocity model, (3) hypocenter locations-raypaths (source-receiver), (4) 2D slices of the final 3D P-velocity model, (5) Magadi Crustal Structure evolution, and (6) Short term Crustal Structure changes. They are presented as well as described as follows:

7.1 Seismicity of Magadi area

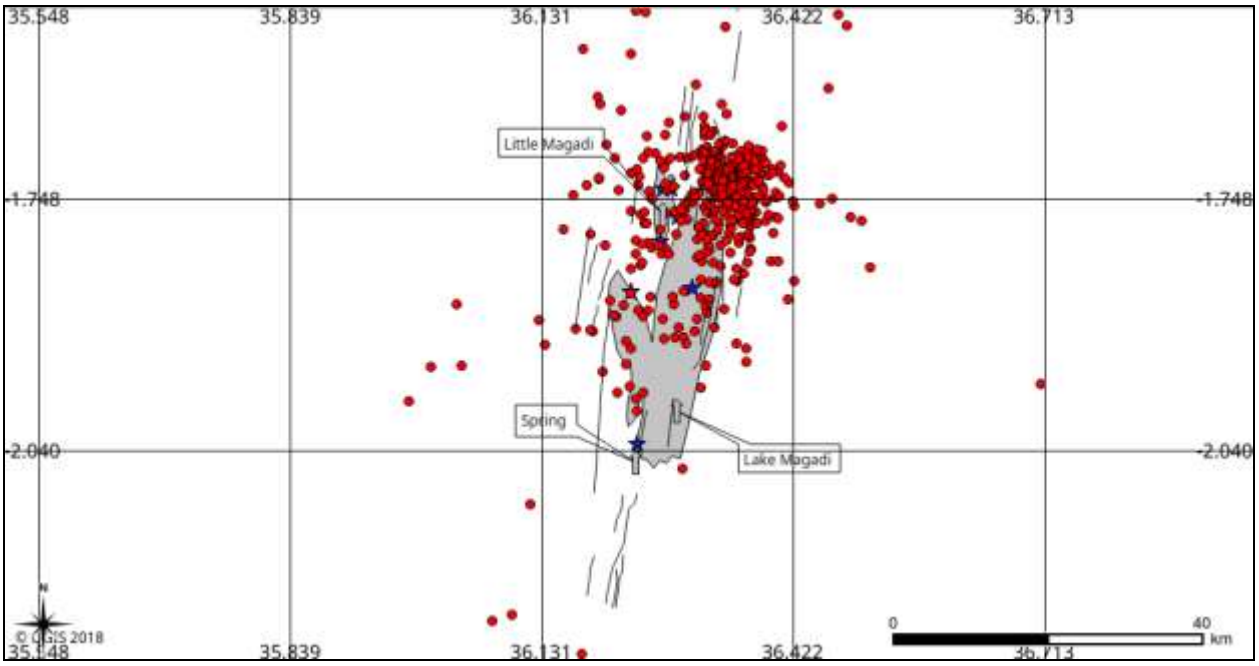

Figure 7.1: Seismicity of Magadi area

The seismicity of Magadi area, fig. 7.1 (shown above), shows the result after plotting the magadi events' epicenters with increased accuracy based on six digit decimal points. The outcome combined both Crafti and Ibs-von Seht data sub-sets for Magadi area. On the north eastern part of the lake, the epicenters are densely clustered together. The earthquake occurrence is highest within this zone and drastically reduces as one move further away. This region is covered by coordinates; 1.4000^0 S to 1.7900^0 S and 36.3000^0 E to 36.5300^0 E. Hence, the total area covered for this region is approximately 1135.3 square kilometers. These events have depths to the focal

point (hypocenter) ranging from a shallow of 0 kilometers below ground level to deepest of 27 kilometers below ground level. Nearly the whole of this zone is highly active as compared to the other zones which are relatively slightly active based on the number of events occurring on these zones.

On the northern region of the lake, the earthquake cluster is relatively densely clustered and has the second highest events occurrences after the north eastern region. The earthquake occurrence is higher in this zone but not similar to that of the north eastern region in terms of cluster density; the occurrence reduces drastically as one move further away to the west. This area is covered by coordinates; 1.4000^0 S to 1.7900^0 S and 36.0000^0 E to 36.3000^0 E. Here, the total area covered is estimated at about 14808.8 square kilometers. These events have depths to the hypocenters ranging from a shallow of 0 kilometers below ground level to deepest of 16 kilometers below ground level. Nearly half of this region is moderately active as compared to the rest of the zones.

The north western part of the lake has a few events occurring close to the lake; no event clusters occur at all. The earthquake occurrence is low-to-moderate in this region and there are a few occurrences as one move further away from the lake. This area is covered by coordinates; 1.4300^0 S to 1.7900^0 S and 35.8000^0 E to 36.1600^0 E. This north-south and east-west distances cover an area of about 1640.2 square kilometers. Here, events have depths to the hypocenters ranging from a shallow of 5 kilometers below ground level to deepest of 27 kilometers below ground level. This region is moderately active in comparison to the northern and north eastern of Lake Magadi.

In contrast to the rest of the north eastern region, the western side of Lake Magadi has nearly sparse distribution of earthquake occurrences. The earthquake occurrence is moderate in this region and becomes very low as one move further away from Lake Magadi to the west. Coordinates covering this area are: 1.7900^0 S to 1.9600^0 S and 35.8000^0 E to 36.1700^0 E. The area of this region is about 796.1 square kilometers. The maximum hypocentral depth is 24 kilometers below ground level and a minimum of 3 kilometers below ground level. This region also is moderately active in comparison to the rest of the zones.

In the south western side of Lake Magadi the earthquake occurrences is evident. The earthquake incidence is moderate in this region and becomes very low as one move further away from Lake Magadi to the extreme end of south west part. Coordinates covering this area are: 1.9000^0 S to 2.1400^0 S and 35.8000^0 E to 36.1700^0 E. The area for this region is about 1123.9 square kilometers. The maximum hypocentral depth is 12 kilometers below ground level and a minimum of 7 kilometers below ground level. This region also is moderately active in comparison to the rest of the zones.

The southern portion of Lake Magadi just like the western and south western portions has moderate earthquake occurrences. The occurrences escalate as one move further away from Lake Magadi to the extreme end of part south part and even on to Lake Natron. Coordinates covering this area are: 1.9600^0 S to 2.2000^0 S and 36.1600^0 E to 36.5100^0 E. The area for this region is about 1063.1 square kilometers. The maximum hypocentral depth is 22 kilometers below ground level and a minimum of 17 kilometers below ground level. This region also is moderately active in comparison to the northern and north eastern portions of Lake Magadi.

The south eastern part of Lake Magadi is also moderately active. The earthquake occurrences diminish as one move further away from Lake Magadi to the extreme end of part south eastern part. Coordinates covering this area are: 1.9000^0 S to 2.2000^0 S and 36.5100^0 E to 36.8000^0 E. The area for this region is about 1101.1 square kilometers. The maximum hypocentral depth is 27 kilometers below ground level and a minimum of 12 kilometers below ground level.

And finally, the eastern part of Lake Magadi like most of the other zones is also moderately active. The earthquake occurrences diminish as one move further away from Lake Magadi to the extreme end of the eastern part. Coordinates covering this area are: 1.7900^0 S to 1.9600^0 S and 36.1700^0 E to 36.8000^0 E. The area for this region is about 1377.0 square kilometers. The maximum hypocentral depth is 25 kilometers below ground level and a minimum of 14 kilometers below ground level.

7.2 1D P-Velocity Model

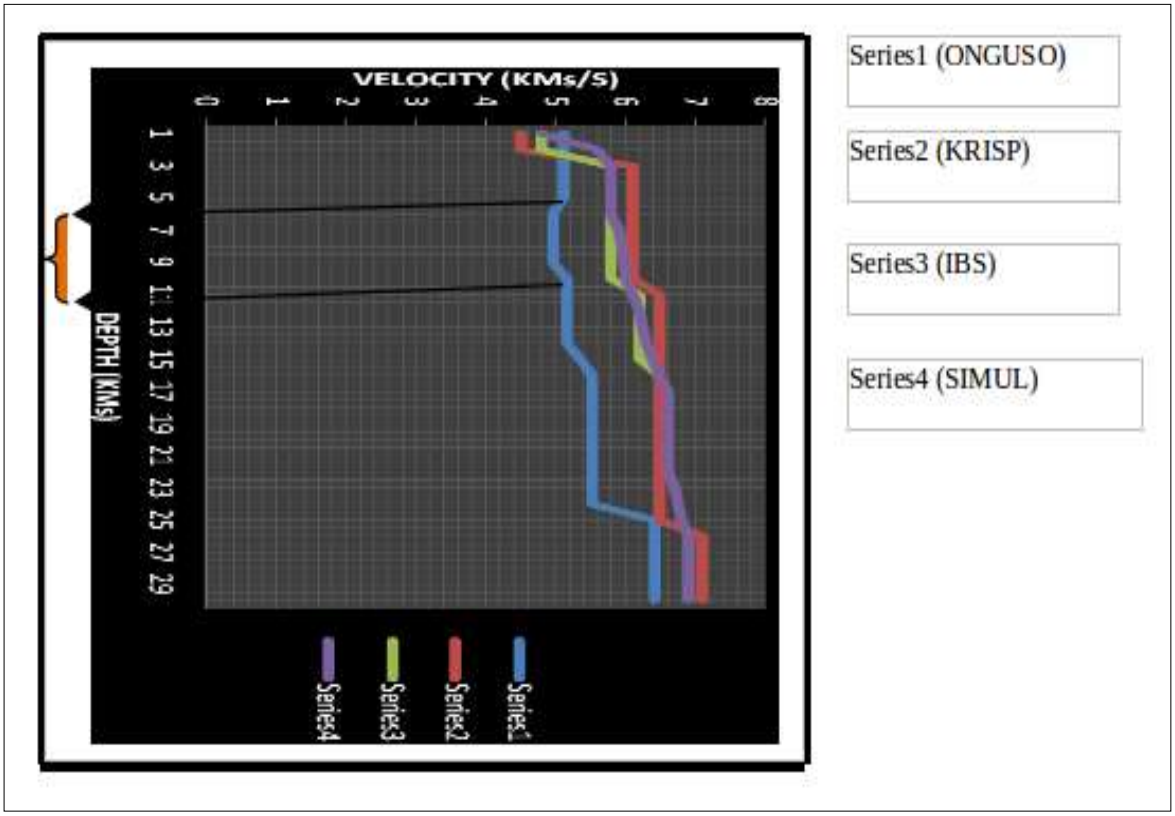

Figure 7.2: 1D P-velocity-depth functions for point 1.8572^0 S and 36.15^0 E

The 1D P-velocity inversion model results above (fig. 7.2) shows P-velocities varying as a function of depth only. In figure 7.2, there is significant difference between series1 (ONGUSO) and previous studies 1D P-velocity depth models. There are two major reasons which explain the observed difference. The first one is the fact that a sub set of the Ibs-von Seht data sub set was used to run the 1D inversion, hence, the ray-path coverage in some sections of the inversion grid was inadequate unlike using a complete set of evenly distributed data where ray-path coverage improved significantly. The other major reason for observed difference is lack of access to gravity data and drill-hole lithology logs for this research work which is very important in constraining the 1D inversion unlike previous studies 1D P-velocity depth models where access to both gravity and drill-hole lithology logs was adequate.

The four (4) 1D models have ignored entire low velocity for first 100 meters of weathered materials. The velocities range from a minimum of 4.4 kilometers per second to a maximum of

5.2 kilometers per second at a depth of 0 kilometers deep. The reasons for these observations include inability of the Velest software to resolve the near surface velocity contrast to finer details; the chosen point falls on outcropping high velocity bedrock, and improperly constrained starting P-velocity model.

The high P-velocity for all of the rest of the models (except Series1 (this work)) gradually increases at a depth of between 0 kilometers deep to a depth of 3 kilometers attaining a velocity of about 6 kilometers per second then remains constant for the next about 8 kilometers for Series 2 (KRIS) and Series 3 (IBS). However, Series 4 remains constant only for the next 3 kilometers up to a depth of 6 kilometers deep then it increases from 5.8 kilometers per second to 6 kilometers per second instead of remaining constant. Series 1 (this work) remains with a constant velocity from surface up to a depth of 5 kilometers deep. It declines in velocity at a depth of 5 kilometers to 9 kilometers from 5.2 kilometers per second to 4.8 kilometers per second with a velocity difference in comparison to the rest of the models ranging from a low of 0.2 kilometers per second to a high of about 0.8 kilometers per second; thought to be probable magma intrusion. Below this depth, a gradual increase in velocity is evident for all the models.

This increase starts from a depth of about 11 kilometers deep to about 30 kilometers deep. Series 2, 3 and 4 increase in velocity from about 6.2 kilometers per second at the vertical extent of 11 kilometers to a high of 7.1 kilometers per seconds at 30 kilometers deep. In contrast, Series 1 (this work) maintains a velocity difference of about 0.1 to 0.9 kilometers per second, though it too increases in velocity from 5.2 kilometers per second at 11 kilometers deep to a high of 6.7 kilometers per second at 30 kilometers deep.

This work's 1D P-velocity model maintains a velocity difference of about 0.1 to 0.8 kilometers per second from the start to the end. There are reasons which can be a possible explanation for this observation. These reasons include: the design of the initial starting 1D P-velocity model, high level of perturbation and adequate amount of the constraining seismic travel time data.

7.3 2D Seismic hypocenters locations and ray-path to receiver (source-receiver)

The illustration below, (fig. 7.3), shows the distribution of some of the hypocenters for the Magadi events. This output was possible through utilization of Generic Mapping Tool (GMT) output files from 3D Fast Marching Method (FMM) (Rawlinson et al., 2004a, 2004b, and De Kool, 2006) results of Generic Mapping Tool slices of the 3D inversion output overlaid on each other (overlaying great circle receivers file, and sources file on ray-paths file).

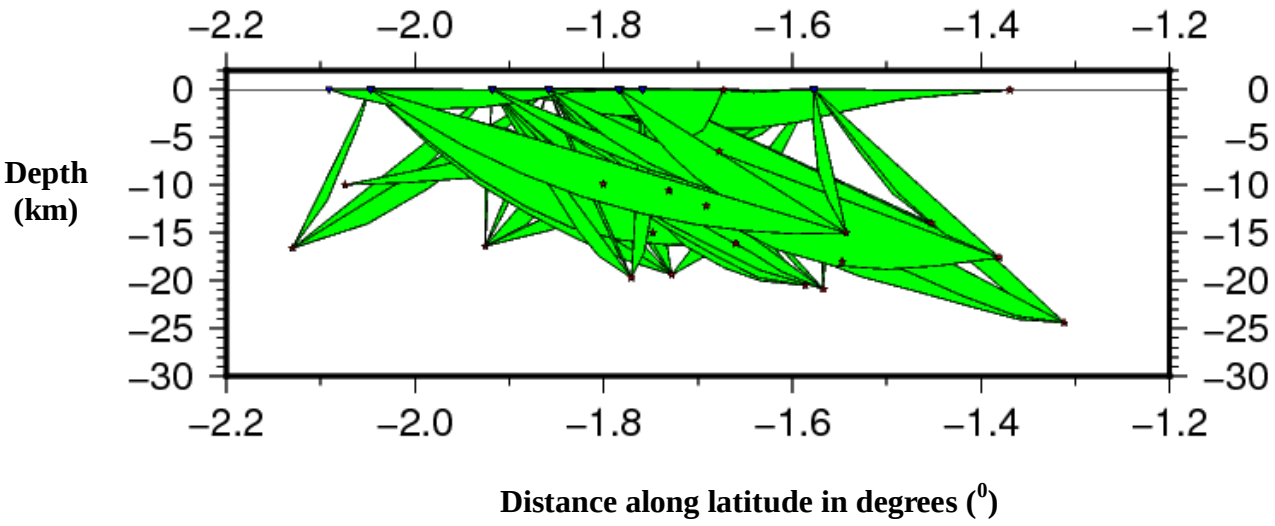

Figure 7.3: Hypocenter locations and ray-paths (source to receiver)

The source depths distribution output covered an area whose coordinates include: northing ranging between 1.20^0 S and 2.2^0 S while depth ranges between 0.0 kilometers and 27 kilometers. The various portions of image show distinct depth distribution. In the lower left end of the map, the depth range between 17 kilometers to 10 kilometers. This meant that the degree of faulting activity is mainly occurring at near surface crustal layers and diminishes with depth. Hence, the deepest part of this region will be expected to be stable and have low signs of faulting activities. This portion is then followed by the lower right part of the image which shows slightly deeper source depth of 27 kilometers as compared to the lower left of the above display. However, when the upper left was scrutinized, there was a difference in depths of the micro-events; all events were shallow. In this part, the faulting processes tend to be at greater depths due to deeper hypocenters than the upper right of wave-tracking display, (fig. 7.3). This then implies that the

faulting process changes from occurring in the shallower layers of the Magadi crust as is evidenced in the upper right to deeper layers; 25 kilometers and below.

The ray-tracing by fm3d sub-routine is two-types. The first type is the direct shooting of ray from the source to receiver in a straight line. This type of ray-tracing is evident to both the left hand side and the right hand side (fig. 7.3) apart from the center. The second ray-tracing type is the bending of rays near the source origin in an attempt to improve the curvature of the ray and then a final straightening as the ray moves out of the refined source grid and enters the course grid of the velocity continuum. According to figure 7.3 above, the deeper sources tend to have a smoother curvature. This is very evident with deep events, left hand side about 17 kilometers deep event. And to the extreme right hypocenter about 25 kilometers, compared to the shallower sources where the curvature tend to have sharp corners. This is to the left hand side depth of about 12 kilometers and to the extreme right, shallow depth of about 0 kilometers (fig. 7.3).

7.4. 3D travel-time seismic tomography results

FMM has architecture limitations since only 2D GMT plotting scripts are available. Hence, it is not possible to visualize 3D Voxell block for the final 3D inversion model. The results of 3D travel-time tomography process in form of 2D slices show complex interface structure which varies with depth; 3 to 13 km and 35.6^0 E to 36.2^0 E laterally as shown on figure 7.4. Beyond 15 km, the velocity remains fairly constant possibly due to the reduction of the rays coverage meant to constrain the velocity contrast. The velocity remains fairly constant to the right hand side, 36.2^0 E to 36.8^0 E and the left hand side, 35.2^0 E to 35.4^0 E. The lateral units have not been changed from degrees to kilometers because FMM package was designed to use degrees as the fixed units laterally unlike depth units which are in kilometers. The high velocity zone tends to have nearly oval shape. The velocity of 5 to about 5.5 kilometers per second pinches out as one moves toward the surface at 35.2^0 E to 35.4^0 E. Furthermore, at depth of about 3 kilometers to 10 kilometers, an oval shaped high velocity intrusive body is evident. However, as you move to depths of about 14 kilometers to 30 kilometers, laterally to the right of 36.2^0 E and left of 35.4^0 E, the velocities remain fairly constant. This final seismic tomography solution model, which was obtained after six iterations of the non-linear technique, with dicing reduced from 15 to 10, was meant to enable quick image plotting, as given in figure 7.4 below. Six iterations were

chosen. The reason being after performing 9 iterations and comparing the results, there was no significant change in root mean square on subsequent iterations after the sixth iteration. Hence, convergence had been achieved after the sixth inversion iteration.

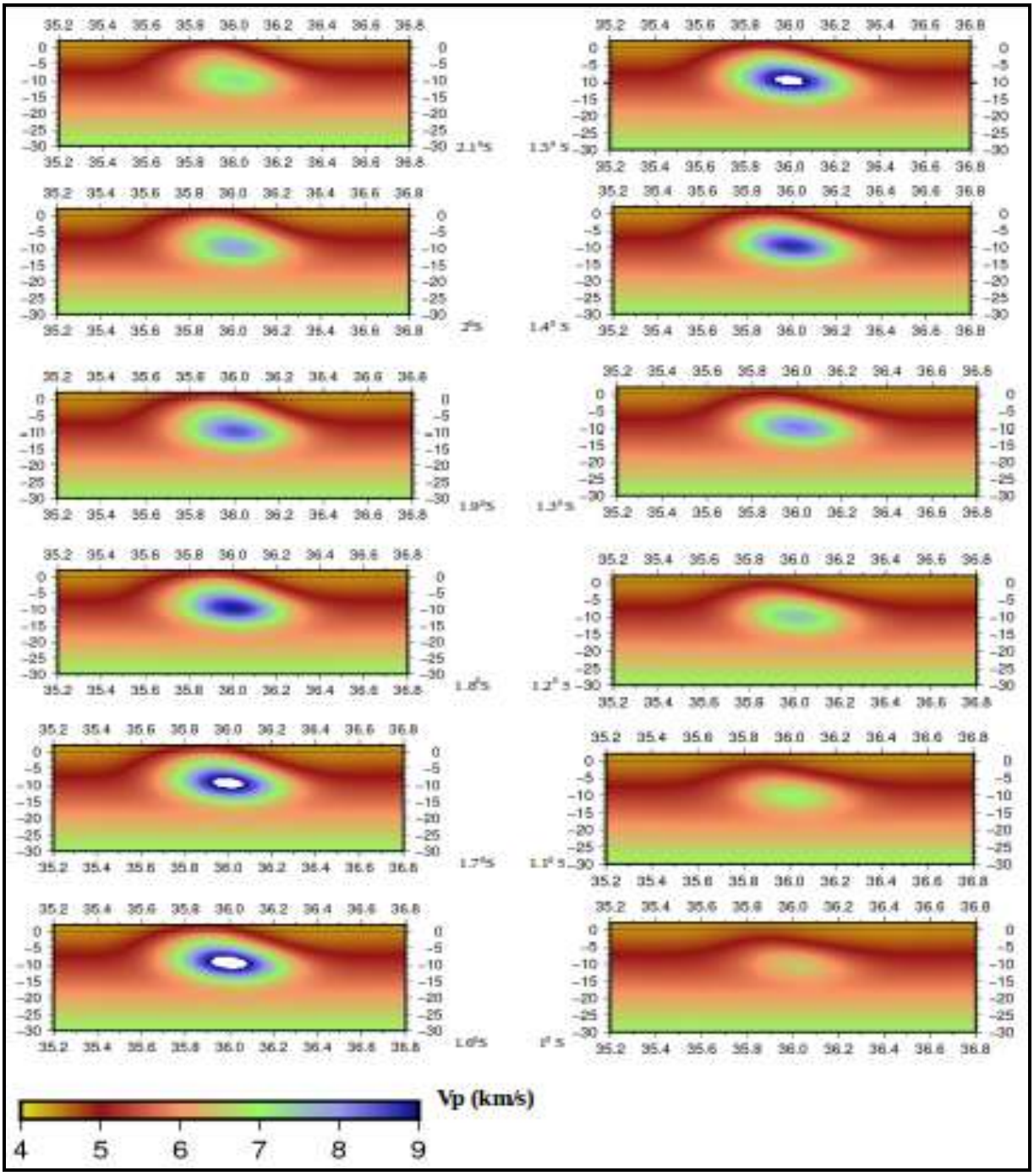

Figure 7.4: This work's 2D slices (1997-1998), E-W direction, vertical scale in kilometers (km) and horizontal scale in degrees (^{0})

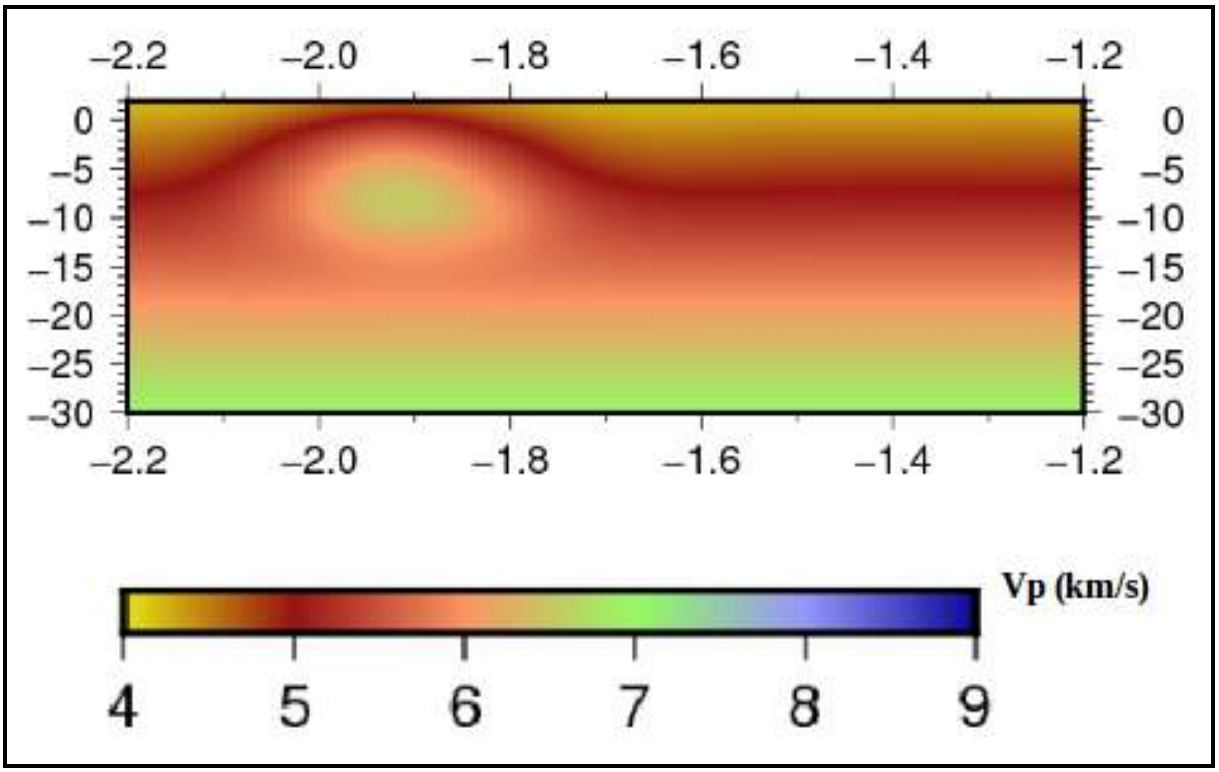

Figure 7.5: This work's 2D slice (1997-1998), N-S direction, at 36.2^0 E, scale units Vp (km/s)

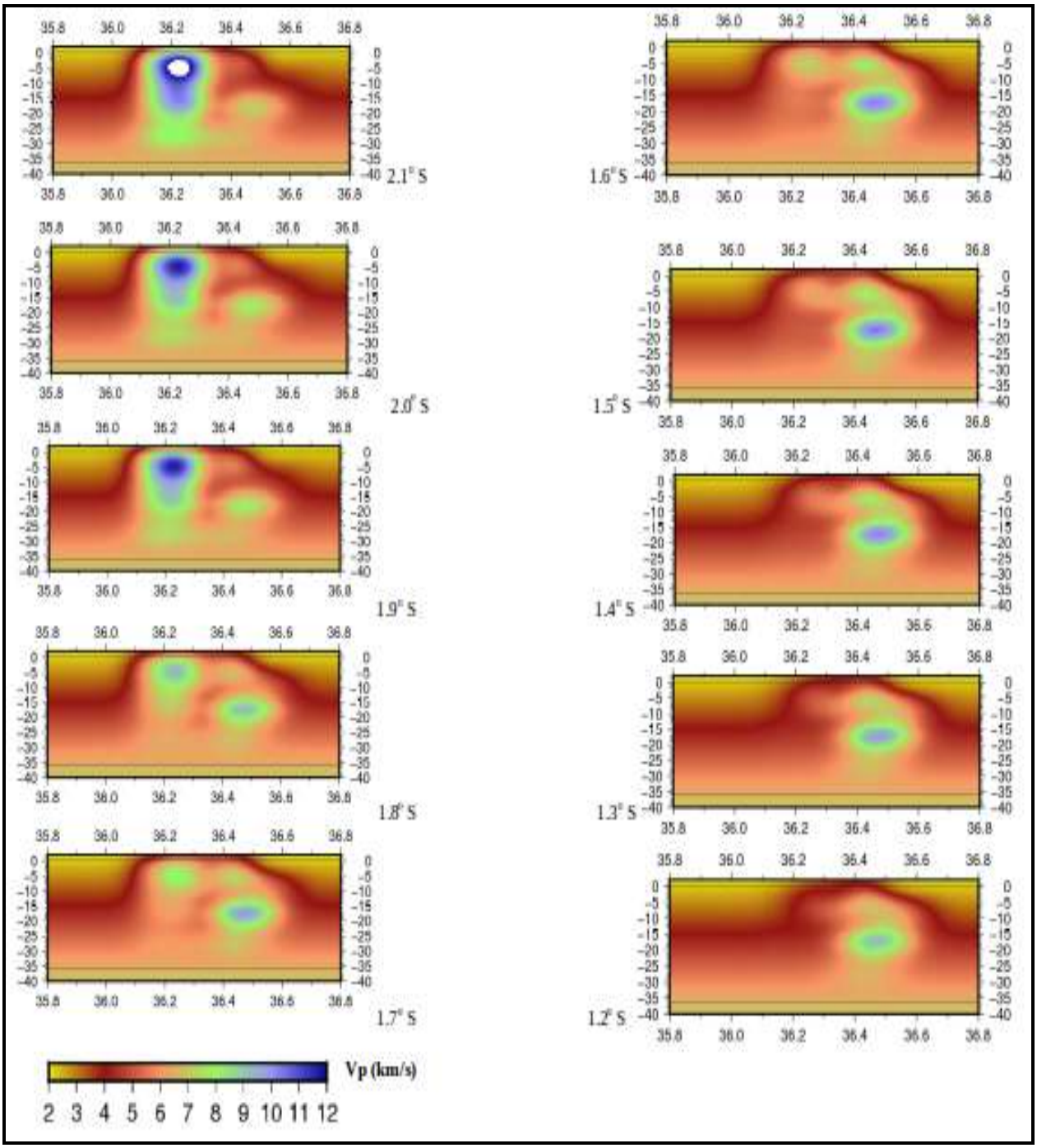

Figure 7.6: This work's 2D slices (2013-2014), E-W direction, velocity scale units Vp (km/s)

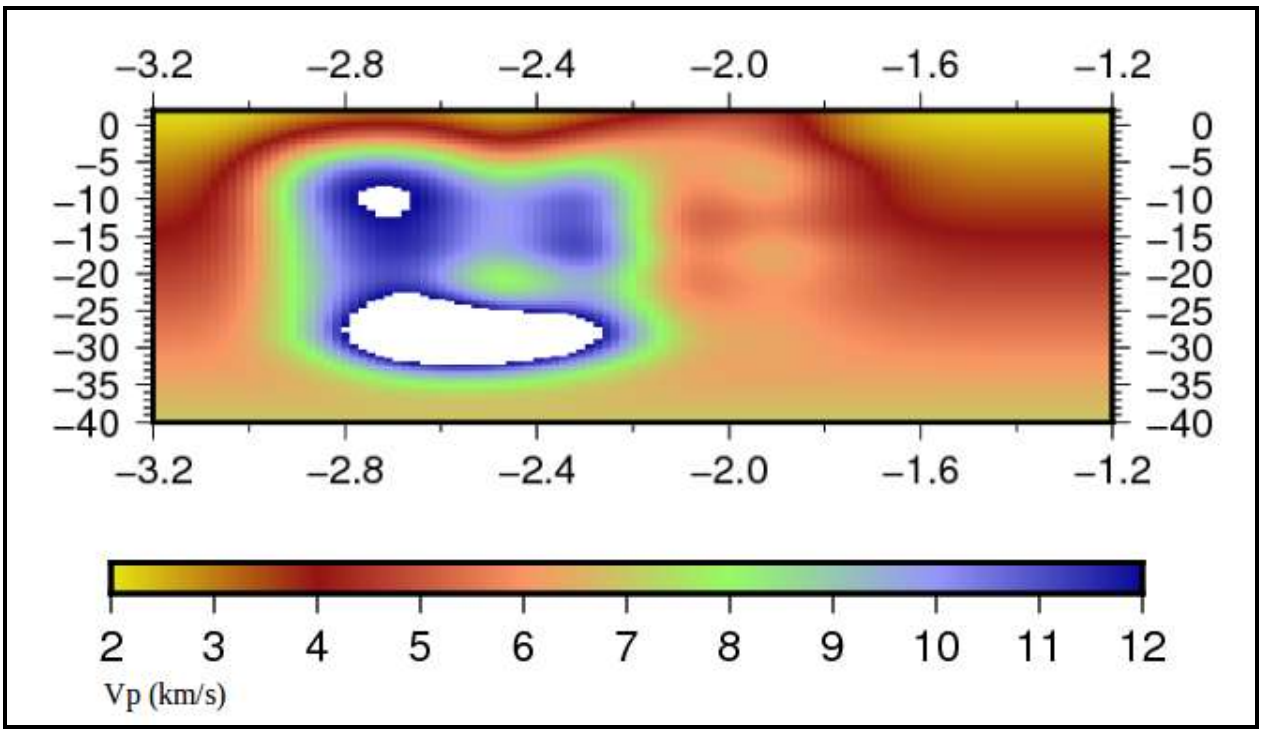

Figure 7.7: This work's 2D slice (2013-2014), N-S direction, at 36.2^0 E, scale units Vp (km/s)

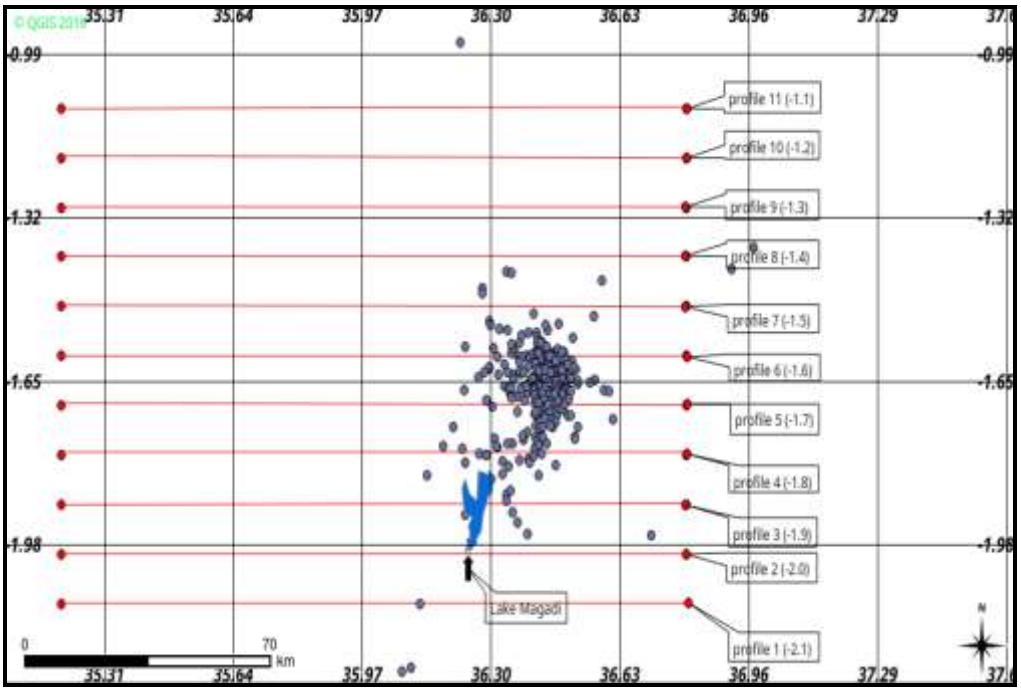

Figure 7.8: Profile lines where 2D slices were taken, latitude and longitude units in degrees (^{0})

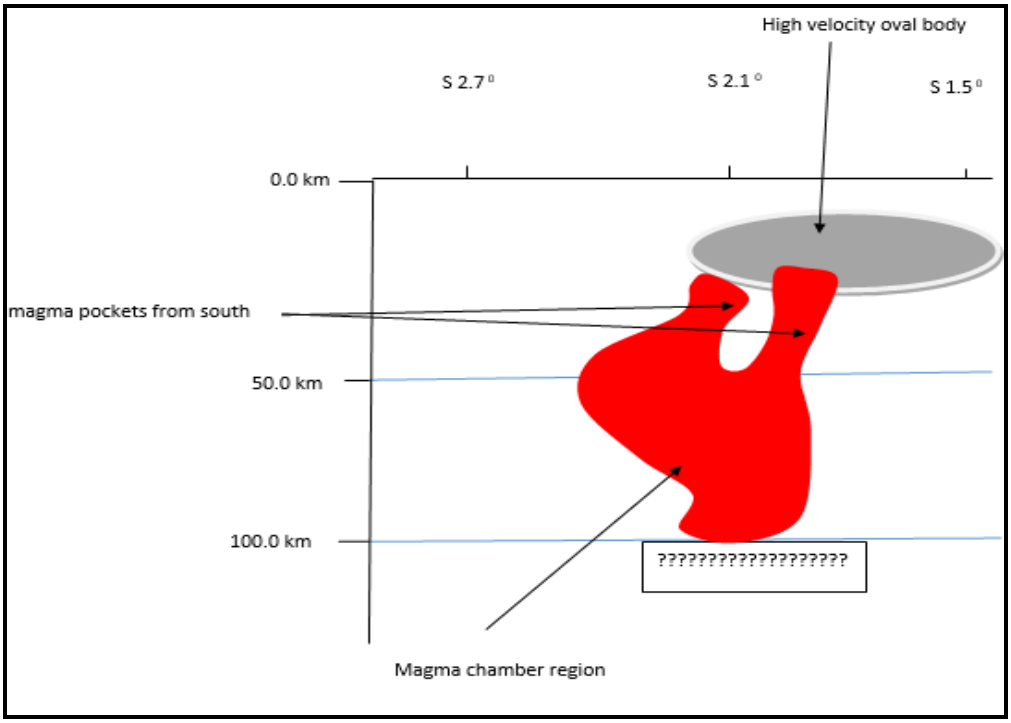

Figure 7.9: Sketch of positive P-velocity anomaly & probable magma intrusion flow path

A slice through final 3D P-velocity inversion result, this work (1997-1998), N-S direction, at longitude 36.20^0 E, (fig. 7.5), shows velocity varying both with depth and laterally. At a depth between 0-to-5 kilometers, and 2.2^0 S to 1.1^0 S, velocity range between 5.5 kilometers per second to 6.2 kilometers per second. At below the point 2.2^0 S and above 1.1^0 S velocities are fairly constant at between 4.2 kilometers per second to about 4.5 kilometers per second. In the layer with depth ranging between 5 and 10 kilometers deep, and laterally between 2^0 S and 1^0 S, a zone exist with a higher velocity of about 6.7 kilometers per second and nearly oval shape. The rest of the portions; below 2^0 S and above 1^0 S, the velocity remains fairly constant at a range of between about 5.3 kilometers per second to about 5.7 kilometers per second.

The last two layers: depth range 10-to-20 and 20-to-30 kilometers deep, the velocity is fairly constant. Depth range of between 10-to-20 kilometers deep, velocity is about 6 kilometers per second and is the same laterally. However, velocity increases, as one moves from second last layer; depth range of between 10-to-20 kilometers to the last layer; depth range of between 20 kilometers deep to 30 kilometers deep, to about 7.0 kilometers per second which is constant throughout this bottom-most layer. Figures 7.1 and 7.3 show zones which have been perfectly constrained by the data (adequate ray-coverage) and those which have been poorly constrained after the completion of the ray tracing using the dynamic up and down narrow-band of the fm3d routine in the fast marching method package, and discussed as follows.

In the north south direction, 1.7^0 S and 2.1^0 S, is well covered by the rays, hence, perfectly constrained. However, zones 1.2^0 S to 1.65^0 S and 2.1^0 S to 2.2^0 S have few rays to none at all, hence, poorly constrained by the data. In addition, in the E-W slice, 35.2^0 E to 35.4^0 E is poorly constrained by data; covered by few ray paths, 35.6^0 E to 36.2^0 E is perfectly constrained by the data; adequately covered by ray paths. While the right hand side portion; 36.2^0 E to 36.8^0 E has low number of ray paths covering it, hence, poorly constrained by the data. Such variations are as a consequent of software type and available data; apart from the difference in software architecture of FMM as a contributing factor. 499 rays-paths were rejected by fm3d software and marked as inconsistent out of the possible 1998 ray-paths which were available for the inversion process. These factors made this work's 3D inversion models to differ greatly from the other models.

Few rays covered a maximum depth of 29 kilometers deep, while most of the depths to the hypocenters range between 0 kilometers to 19.5 kilometers deep. This means that the zone between 20 kilometers to 30 kilometers is fairly to poorly constrained by the data unlike the zone between 0 kilometers deep and 19 kilometers deep within 35.6^0 E to 36.2^0 E laterally which is relatively perfectly constrained by the data; has adequate ray paths coverage.

This work (2013-2014) final 2D slice results were obtained in E-W direction. First slice was sliced at longitude 35.80^0 E to 36.80^0 E, latitude 1.2^0 S (fig. 7.6). The velocity varies both with depth and laterally and form globules. At a depth between 0-to-15 kilometers, 1.2^0 S and 36.2^0 E to 36.6^0 E, velocity range between 5.0 kilometers per second to 7.2 kilometers per second. Two elongated globules (sausage-like) are evident. At a depth of 15 to 25 kilometers, the shapes of the globules change from being elongated to oval. This change accompanied with increase in velocity from a range of 5.0 to 7.2 kilometers per second to a range of 8.0 to 11.0 kilometers per second. At below 36.2^0 E, above 36.6^0 E and below 25 kilometers, velocities are fairly constant laterally but increase with depth. These regions with fairly constant velocity are believed to be zones which were poorly constrained by the observed data (very inadequate ray-paths coverage).

Close observations show that as one move from 1.2^0 S to 1.6^0 S, the initially faint and elongated globules become more clear and oval in shape. At 1.7^0 S, the number of globules increases to four and the laterally region with good ray-paths coverage changes to a range of 36.1^0 E to 36.6^0 E from a range of 36.2^0 E to 36.6^0 E. These four globules have velocities ranging from 5.0 kilometers per second to 11.0 kilometers per second. The rest; above 36.6^0 E, below 36.1^0 E and below 30 kilometers deep, velocities are constant and only increases with depth. Moving from 1.7^0 S to 2.1^0 S, globules at 36.45^0 E & 20 kilometers deep, 36.45^0 E & 5 kilometers deep and 36.3^0 E & 20 kilometers deep grow faint. In the contrary, globule at 36.25^0 E & 5 kilometers deep which was initially faint, become stronger. And finally, rays covered a maximum depth of 34.9 kilometers deep, while most of the depths to the hypocenters range between 0 kilometers to 25 kilometers deep. This means that the zone between 25 kilometers to 35 kilometers is fairly to poorly constrained by the data unlike the zone between 0 kilometers deep and 25 kilometers deep within 36.1^0 E to 36.6^0 E laterally which is relatively perfectly constrained by the data.

7.5 Magadi Crustal Structure Evolution

This study confirms the existence of high velocity anomaly, the position of this high velocity intrusive body is shifted both laterally and in depth. According to figure 7.4, east west direction, the anomaly lies between 35.8^0 E to about 36.4^0 E laterally and about 4 kilometers to about 12 kilometers in depth. With time, the high velocity anomaly which is originally huge oval shaped body changed to form three smaller oval shaped bodies and a low velocity zone in between them, as supported by figure 7.6. The high absolute velocity zones which take oval to globule shape probably represent mafic intrusions from the bottom of crust-top of mantle which contrast with pockets of low absolute velocity zones indicative of small magma injections or intrusions from the deep seated repository at the upper mantle area on to the shallower crust.

In the north south orientation, figure 7.5 shows an oval body with high P-wave velocity. This high velocity range from about 6.5kilometers per second to about 8 kilometers per second. This oval body covers from about 2.0^0 S to about 1.8^0 E orientations along the latitude. Along the depth, it covers from about 4 kilometers to about 12 kilometers; about 8 kilometers thick. According to figure 7.7, the originally oval bodies shown by figure 7.5 broke, changed and deformed into two smaller oval bodies with the top one being almost sausage-like to globular in shape. They have high P-wave velocity ranging from about 6.5 kilometers per second. There exist two oval shaped low velocity zones to the left side of the two high velocity oval bodies. These low P-wave velocity zones range in velocity from about 3 kilometers per second to 4 kilometers and is believed to have undergone melting due to the intruding small magma chambers. These changes, as per figure 7.7, cover sections with latitude about 2.1^0 S to about 1.8^0 S and depth from about 3 kilometers to about 8 kilometers and about 15 kilometers to about 20 kilometers for the top and bottom oval bodies respectively.

7.6 Short term Crustal Structure changes

The study area has undergone short term crustal structure changes. These changes are very evident from the comparison between figure 7.4 and figure 7.6 for slices in the east west orientation and similarly for figure 7.5 and figure 7.7 for slices in the north south orientation. In

the east west orientation, figure 7.4 shows an oval body with high P-wave velocity believed to be mafic intrusions. This high velocity range from about 6.5kilometers per second to about 8 kilometers per second. This oval body covers from about 35.8^0 E to about 36.4^0 E orientations along the longitude. Along the depth, it covers from about 4 kilometers to about 12 kilometers; about 8 kilometers thick.

According to figure 7.6, the originally oval bodies shown by figure 7.4 broke, changed and deformed into three smaller oval bodies. These oval bodies change in shape from oval shape to sausage-like or globular shape as one moves further south and further north as shown by figure 7.6. They have high P-wave velocity ranging from about 6.5 kilometers per second to about 9 kilometers per second. A central zone is generated in between the three smaller oval bodies with lower P-wave velocity believed to be conduits through which the small magma bodies are injected or intruded into the crust. This lower P-wave velocity range from about 3 kilometers per second to 4 kilometers and the country rock surrounding it is believed to have undergone partial melting due to the intruding small magma chambers. These changes, as per figure 7.6, cover sections with longitude about 36^0 E to about 36.6^0 E and depth from about 3 kilometers to about 16 kilometers. In the north south direction, figure 7.5 displays an oval body with high P-wave velocity. This high velocity varies from about 6.5kilometers per second to about 8 kilometers per second. The oval body covers some sections of figure 7.5 from about 2.0^0 S to about 1.8^0 E orientations along the latitude. Along the depth, it covers a section of figure 7.5 from about 4 kilometers to about 12 kilometers; about 8 kilometers in terms of thickness.

According to figure 7.7, the originally oval bodies shown by figure 7.5 broke, changed and deformed into two smaller oval bodies with the top one being almost sausage-like to globular in shape. They have high P-wave velocity ranging from about 6.5 kilometers per second. There exist two oval shaped low velocity zones to the left side of the two high velocity oval bodies. These low P-wave velocity zones range in velocity from about 3 kilometers per second to 4 kilometers and is believed to have undergone melting too due to the intruding small magma chambers. These changes, as per figure 7.7, cover sections with latitude about 2.1^0 S to about 1.8^0 S and depth from about 3 kilometers to about 8 kilometers and about 15 kilometers to about 20 kilometers.

8.0 DISCUSSION

In this study, the seismicity map developed for the Magadi area shows varying distribution of events. The north eastern parts of Lake Magadi, the epicenters are densely clustered together. The earthquake occurrence is highest within this zone and drastically reduces as one move further away. This region is covered by coordinates; 1.4000^0 S to 1.7900^0 S and 36.3000^0 E to 36.5300^0 E. Hence, the total area covered for this region is approximately 1135.3 square kilometers. These events have depths to the focal point (hypocenter) ranging from a shallow of 0 kilometers below ground level to deepest of 34.9 kilometers below ground level. Nearly the whole of this zone is highly active as compared to the other zones which are relatively slightly active based on the number of events occurring on these zones. On the northern region of the lake, the earthquake cluster is relatively densely clustered and has the second highest events occurrences after the north eastern region. The earthquake occurrence is higher in this zone but not similar to that of the north eastern region in terms of cluster density; the occurrence reduces drastically as one move further away to the west. This area is covered by coordinates; 1.4000^0 S to 1.7900^0 S and 36.0000^0 E to 36.3000^0 E. Here, the total area covered is estimated at about 14808.8 square kilometers. These events have depths to the hypocenters ranging from a shallow of 0 kilometers below ground level to deepest of 16 kilometers below ground level. Nearly half of this region is moderately active as compared to the rest of the zones.

The north western part of the lake has a few events occurring close to the lake; no event clusters occur at all. The earthquake occurrence is low-to-moderate in this region and there are a few occurrences as one move further away from the lake. This area is covered by coordinates; 1.4300^0 S to 1.7900^0 S and 35.8000^0 E to 36.1600^0 E. This north-south and east-west distances cover an area of about 1640.2 square kilometers. Here, events have depths to the hypocenters ranging from a shallow of 5 kilometers below ground level to deepest of 34.9 kilometers below ground level. This region is moderately active in comparison to the northern and north eastern of Lake Magadi. In contrast to the rest of the north eastern region, the western side of Lake Magadi has nearly sparse distribution of earthquake occurrences. The earthquake occurrence is moderate in this region and becomes very low as one move further away from Lake Magadi to the west. Coordinates covering this area are: 1.7900^0 S to 1.9600^0 S and 35.8000^0 E to 36.1700^0 E. The

area of this region is about 796.1 square kilometers. The maximum hypocentral depth is 24 kilometers below ground level and a minimum of 3 kilometers below ground level. The deeper events within the clusters are few. Hence, the deeper extent has negligible effect on cluster of earthquakes.

In the south western side of Lake Magadi the earthquake occurrences is evident. The earthquake incidence is moderate in this region and becomes very low as one move further away from Lake Magadi to the extreme end of south west part. Coordinates covering this area are: 1.9000^0 S to 2.1400^0 S and 35.8000^0 E to 36.1700^0 E. The area for this region is about 1123.9 square kilometers. The maximum hypocentral depth is 12 kilometers below ground level and a minimum of 7 kilometers below ground level. This region also is moderately active in comparison to the rest of the zones. The southern portion of Lake Magadi just like the western and south western portions has moderate earthquake occurrences. The occurrences escalate as one moves further away from Lake Magadi to the extreme end of part south part and even on to Lake Natron. Coordinates covering this area are: 1.9600^0 S to 2.2000^0 S and 36.1600^0 E to 36.5100^0 E. The area for this region is about 1063.1 square kilometers. The maximum hypocentral depth is 22 kilometers below ground level and a minimum of 17 kilometers below ground level. This region also is moderately active in comparison to the northern and north eastern portions of Lake Magadi.

The south eastern part of Lake Magadi is also moderately active. The earthquake occurrences diminish as one move further away from Lake Magadi to the extreme end of part south eastern part. Coordinates covering this area are: 1.9000^0 S to 2.2000^0 S and 36.5100^0 E to 36.8000^0 E. The area for this region is about 1101.1 square kilometers. The maximum hypocentral depth is 27 kilometers below ground level and a minimum of 12 kilometers below ground level, whereas, the eastern part of Lake Magadi like most of the other zones is also moderately active. The earthquake occurrences diminish as one moves further away from Lake Magadi to the extreme end of the eastern part. Coordinates covering this area are: 1.7900^0 S to 1.9600^0 S and 36.1700^0 E to 36.8000^0 E. The area for this region is about 1377.0 square kilometers. The maximum hypocentral depth is 25 kilometers below ground level and a minimum of 14 kilometers below ground level.

Similarly, the distribution of hypocenters is varying just like the seismicity distribution. The northings range between 1.20^0S and 2.2^0 S for depth between 0.0 kilometers and 27 kilometers. At our lower left end of the hypocenter locations (fig. 7.3), there is a depth range between 17 kilometers to 10 kilometers. This means that the degree of faulting activity is mainly occurring at near surface crustal layers and diminishes with depth. Hence, the deepest part of this region will be expected to be stable and have low signs of faulting activities. This portion is then followed by the lower right part of the image which shows slightly deeper source depth of 34.9 kilometers as compared to the lower left of the above display. However, when the upper left was scrutinized, there was no difference in depths of the micro-events; all events were shallow. In this part, the faulting processes tend to be greater depths due to deeper hypocenters than the upper right of wave-tracking display, (fig. 7.3). This implies that the faulting process changes from occurring in the shallower layers of the Magadi crust as is evidenced in the upper right to deeper layers; 25 kilometers and below.

The seismologic composition result of entire Magadi lithosphere is represented by the crustal section in spherical coordination. The layer is defined using velocity grid 12 nodes in either direction (x, y, z) with a node separation of 1.0909 km in depth (z) direction. The interface grid set at 0.0 kilometers deep and 30.0 kilometers to 35.0 kilometers deep has same number of grid nodes of 12 nodes as above in latitude and longitude. The 3D constant gradient starting model has absolute velocity varying in depth and constrained by early near surface active source velocity models (Mulumbu, 2015) and a final 1D P-velocity model velest output (fig. 7.2). The velocity variation for this 1D result gradually increases from a low of 5.0 kilometers per second to a high of about 6.7 kilometers per second except at a depth of between 5.0 kilometers to about 9 kilometers where velocity decrease from 5.0 kilometers per second to about 4.7 kilometers per second. The constrained 1D starting model in grid3dg.in file is converted to 3D starting absolute velocity model by use of the cubic B-spline which evenly interpolates into a three dimensions (x, y, z) with a subspace dimension of 50; E-W, N-S and depth (Rawlinson et al., 2001, 2004a, 2004b and De Kool, 2006) and produced as a vgrids.in file into same folder which has the observed local earthquakes travel-times dataset file together with propgrid.in and interfaces.in files.

The observed local earthquakes travel-time dataset was inverted using same inversion scheme as that used by De Kool, (2006) and Rawlinson et al., (2001, 2004a, 2004b). Due to FMM architecture limitations, only 2D GMT plot scripts are available; there is lack of 3D plotting scripts. Hence, not possible to visualize 3D Voxell block for the final 3D inversion model. This lead to production of 2D slices oriented to the N-S and E-W directions. Three initial 3D P-velocity models were used to constrain the 3D inversion process; 0.3 kilometers per second to 7.5 kilometers per second, 4.4 kilometers per second to 7.0 kilometers per second and 4.8 kilometers per second to 7.2 kilometers per second. It was found out that the FMM could not resolve to finer details the shallower low velocities representing the weathered zone which has a mean thickness of about 0.07 kilometers. Hence, the low velocities identified by Mulumbu 2015 for the near surface crust (70 meters from surface) were ignored in the 3D inversion from which 2D slices were obtained; E-W including N-S two dimensions portions.

East-West cross-section on latitude 2.1^0 S through final solution model in this work (1997-1998) is shown by figure 7.4. The complex interface structure varies in depth; 0 to 15 km within the central part of figure 7.4. Beyond 15 km, the velocity remains fairly constant possibly due to the reduction of the rays coverage meant to constrain the velocity contrast. The velocity remains fairly constant to both the right hand side, which is, from 36.2^0 E to 36.8^0 E and the left hand side, that is, 35.2^0 E to 35.4^0 E. The high velocity zone tends to have nearly oval shape. The velocity of 5.0 to about 5.5 kilometers per second pinches out as one moves towards the surface at 35.6^0 E to 35.9^0 E laterally. This final seismic tomography solution model was achieved via convergence after six iterations of the non-linear scheme. The dicing was reduced from 15 to 10. This was meant to enable quick image plotting as given in figure 7.4. Noteworthy features are highlighted as shown in figure 7.4. The most evident crustal anomaly is a strong West-to-East positive absolute velocity contrast in the south Magadi displayed by figure 7.4 at 35.7^0 E to 35.9^0 E laterally and about 3 kilometers to 10 kilometers deep. This feature extends further northward and east west directions. A slice through the inversion result, along north south direction, at longitude 36.20^0 E as highlighted by figure 7.5, shows velocity varying both with depth and laterally. At a depth between 0-to-5 kilometers, and 2.1^0 S to 1.7^0 S, velocity range between 5.0 kilometers per second to 5.5 kilometers per second. On left hand side of 2.1^0 S including the right hand side of 1.7^0 S velocities are fairly constant at between 4.0 kilometers per second to

about 4.6 kilometers per second. In the layer with depth ranging between 5 and 10 kilometers deep, and laterally between 2.0^0 S and 1.8^0 S, a zone exist with a higher velocity of about 7.0 kilometers per second and has nearly oval shaped intrusive body. The rest of the portions; to the left hand side of 2.1^0 S and the right hand side of 1.7^0 S, the velocity remains fairly constant at a range of between about 4.3 kilometers per second to about 5.6 kilometers per second unlike the other last two layers.

The last two layers: depth range 10-to-20 and 20-to-30 kilometers deep, the velocity is fairly constant. Depth range of between 10-to-20 kilometers deep, velocity is about 6.0 kilometers per second and is the same laterally. However, velocity increases, as one moves from second last layer with depth range of between 10-to-20 kilometers to the last layer which has depth range of between 20 kilometers deep to 30 kilometers deep, to about 7.0 kilometers per second which is constant throughout this bottom-most layer laterally. Similarly, the most evident crustal anomaly is a strong north-to-south high absolute velocity anomaly in the central Magadi as given in figure 7.5. This feature takes an oval shape in terms of its geometry. We strongly believe that these high velocity anomalies are mafic intrusions from the bottom of crust-top of mantle zones (Ibs-von Seht et al., 2001 and Roecker, 2017). Nevertheless, the extremely low velocity near surface zones of 0.3 to about 1.3 kilometers shown by Mulumbu, (2015), were not well resolved to finer details by the FMM package and thus weathered low velocity layers were interpreted using works by Mulumbu, (2015) and other researchers in the area of study.

This work (2013-2014) 2D slices results were obtained in E-W direction from the final 3D velocity model. First slice was sliced at longitude 36.20^0 E to 36.60^0 E, latitude 1.2^0 S (fig. 7.6). The velocity varies both with depth and laterally and form globules. At a depth between 0-to-15 kilometers, 1.2^0 S and 36.2^0 E to 36.6^0 E, velocity range between 5.0 kilometers per second to 7.2 kilometers per second. Two elongated globules (sausage-like) are evident. At a depth of 15 to 25 kilometers, the shapes of the globules change from being elongated to oval. This change accompanied with increase in velocity from a range of 5.0 to 7.2 kilometers per second to a range of 8.0 to 11.0 kilometers per second. At below 36.2^0 E, above 36.6^0 E and below 25 kilometers, velocities are fairly constant laterally but increase with depth. These regions with

fairly constant velocity are believed to be zones which were poorly constrained by the observed data (very inadequate ray-paths coverage).

Close observations show that as one move from 1.2^0 S to 1.6^0 S, the initially faint and elongated globules become more clear and oval in shape. At 1.7^0 S, the number of globules increases to four and the laterally region with good ray-paths coverage changes to a range of 36.1^0 E to 36.6^0 E from a range of 36.2^0 E to 36.6^0 E. These four globules have velocities ranging from 5.0 kilometers per second to 11.0 kilometers per second. The rest; above 36.6^0 E, below 36.1^0 E and below 30 kilometers deep, velocities are constant and only increases with depth.

Moving from 1.7^0 S to 2.1^0 S, globules at 36.45^0 E & 20 kilometers deep, 36.45^0 E & 5 kilometers deep and 36.3^0 E & 20 kilometers deep grow faint. In the contrary, globule at 36.25^0 E & 5 kilometers deep which was initially faint, become stronger. And finally, rays covered a maximum depth of 34.9 kilometers deep, while most of the depths to the hypocenters range between 0 kilometers to 25 kilometers deep. This means that the zone between 25 kilometers to 35 kilometers is fairly to poorly constrained by the data unlike the zone between 0 kilometers deep and 25 kilometers deep within 36.1^0 E to 36.6^0 E laterally which is relatively perfectly constrained by the data; has adequate ray paths coverage.

2D P-velocity model sections for this research (fig. 7.4 & 7.5) show a region of elevated positive anomalies between 3.5^0 E and 36.2^0 E. In the N-S directions, this region is within coordinates 2.1^0 S and 1.5^0 S. The velocities are 6.6 kilometers per second and above and thought to be mafic intrusive body. Ibs-von Seht et al., (2001), identified a similar region of elevated absolute velocity in this area from similar inversion of local earthquake dataset for absolute velocity variation only (fig. 7.10 profile 5) as shown below. The current image resolution is slightly reduced due to reduction in path coverage to enable quick image display using the generic mapping tool shell scripts and also eliminate bad data-set. This helps to confirm the existence of anomalies in the immediate environs. It has been confirmed by early workers and current research that this region has pockets of low velocity regions (15 kilometers deep -50 kilometers horizontally, 20 kilometers deep 5 kilometers horizontally, 15 kilometers deep 30 kilometers horizontally, and 15 kilometers deep 65 kilometers horizontally) and others have either intrusive

bodies or rotated up-lifted footwall crustal slabs which occurred during faulting process (Roecker, et al. 2017 and Ibs-von Seht et al., 2001).

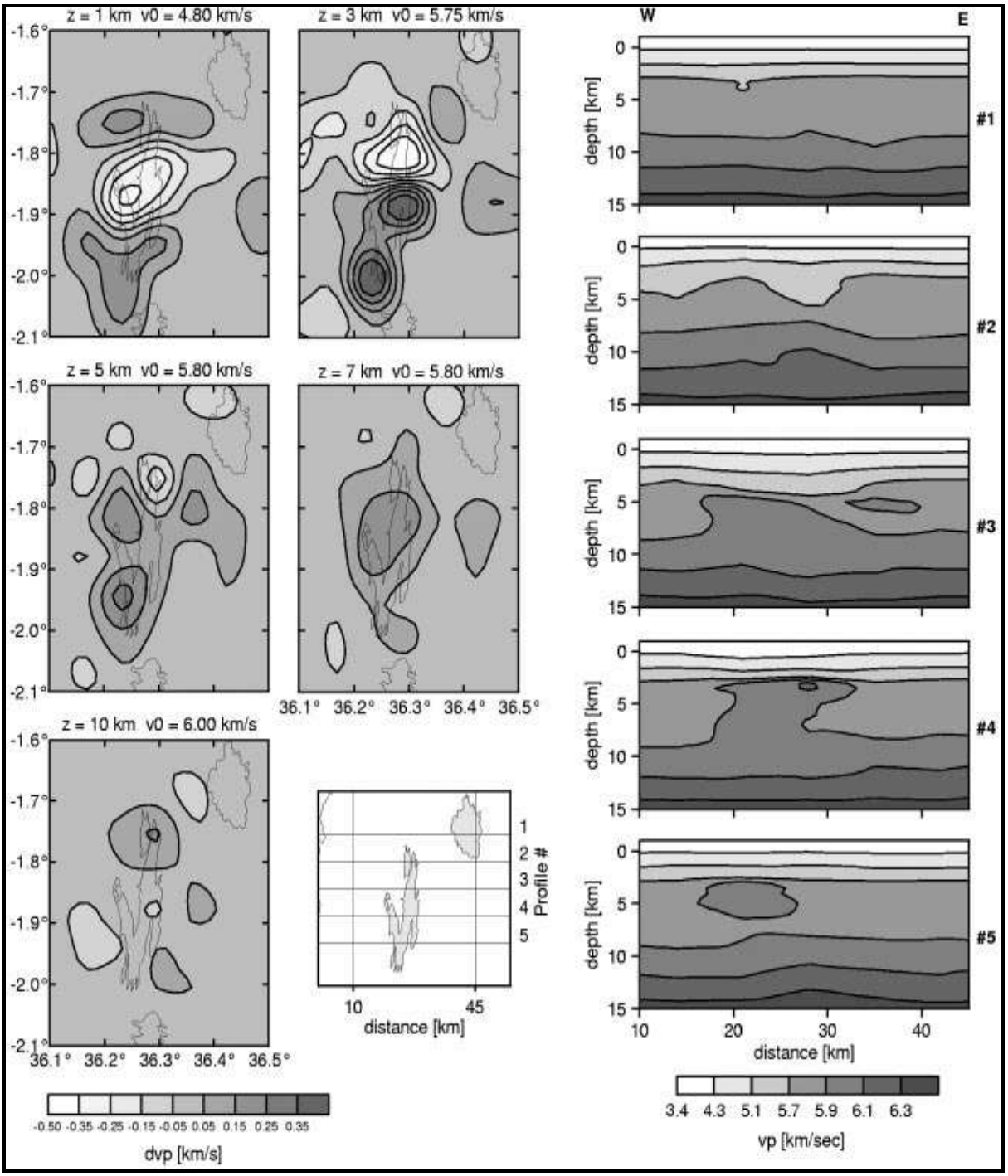

Figure 7.10: Ibs-von Seht et al., (2001) E-w slices of the 3D P-velocity model

Furthermore, on entire upper right and the upper left of figure 7.4, there exists a prominent homogeneous crustal zone with speed changing only with depth. This possibly implies a zone covered by sediments whose degree of compaction and lithification increases with depth. The pattern of anomalies on entire top shallower crust, figure 7.4, should be rather dissimilar from the one of deeper crust. Specifically, prominent speed dissimilarity recognized at shallower crust is no longer there. There exist horizontally uniform higher velocity zone at a depth of about 3 kilometers and below. There are differences between figure 7.4 and Ibs-von Seht et al., (2001) work-profile 5 sliced at 1.97^0 S. These differences include relatively high data coverage, and the geometry of the high velocity intrusion is oval shaped unlike Ibs-von Seht et al., (2001) work where the high velocity intrusive body is not perfectly oval shaped. The other difference is the facts that fifth slice of Ibs-von Seht et al., (2001) work closer to 2.1^0 S, is more resolved than in figure 7.4. On the other hand, the two investigations (this work and Ibs-von Seht et al., (2001) work) are similar in that same intrusive body of nearly same geometry is delineated by both although the positions vary both laterally and in depth. This is possible if figure 7.4 is compared to profile number five (5) in works done by Ibs-von Seht et al., (2001) which is clearly shown in figure 7.10.

When figure 7.11 which is shown below is considered, the first layer between 0 to 5 kilometers deep, the velocity is 5.2-to-5.7 kilometers per second with slightly lower velocity of about 5 kilometers per second or less than 5 kilometers per second on the center and to the right hand side near surface. At a depth of between 6 kilometers to 25 kilometers, velocity is constant at about 6.2 kilometers per second with pockets of higher velocities of between 6.5 kilometers per second and 6.8 kilometers per second and low velocity subducting zone having velocity of about 5.8 kilometers per second. Beyond 26 kilometers, velocity remains constant at 8-to-9 km/s. According to Roecker, et al. (2017), considerable features developed include the low P and S wave-speeds underlying mostly this entirety of the fissure region. There are also relatively high wave-speeds tabular feature positioned alongside the western periphery of the Natron rift zone. And relatively low parameters of V_p/V_s all over this top crust, along with the correlations of V_p/V_s with both V_p and V_s on many zones.

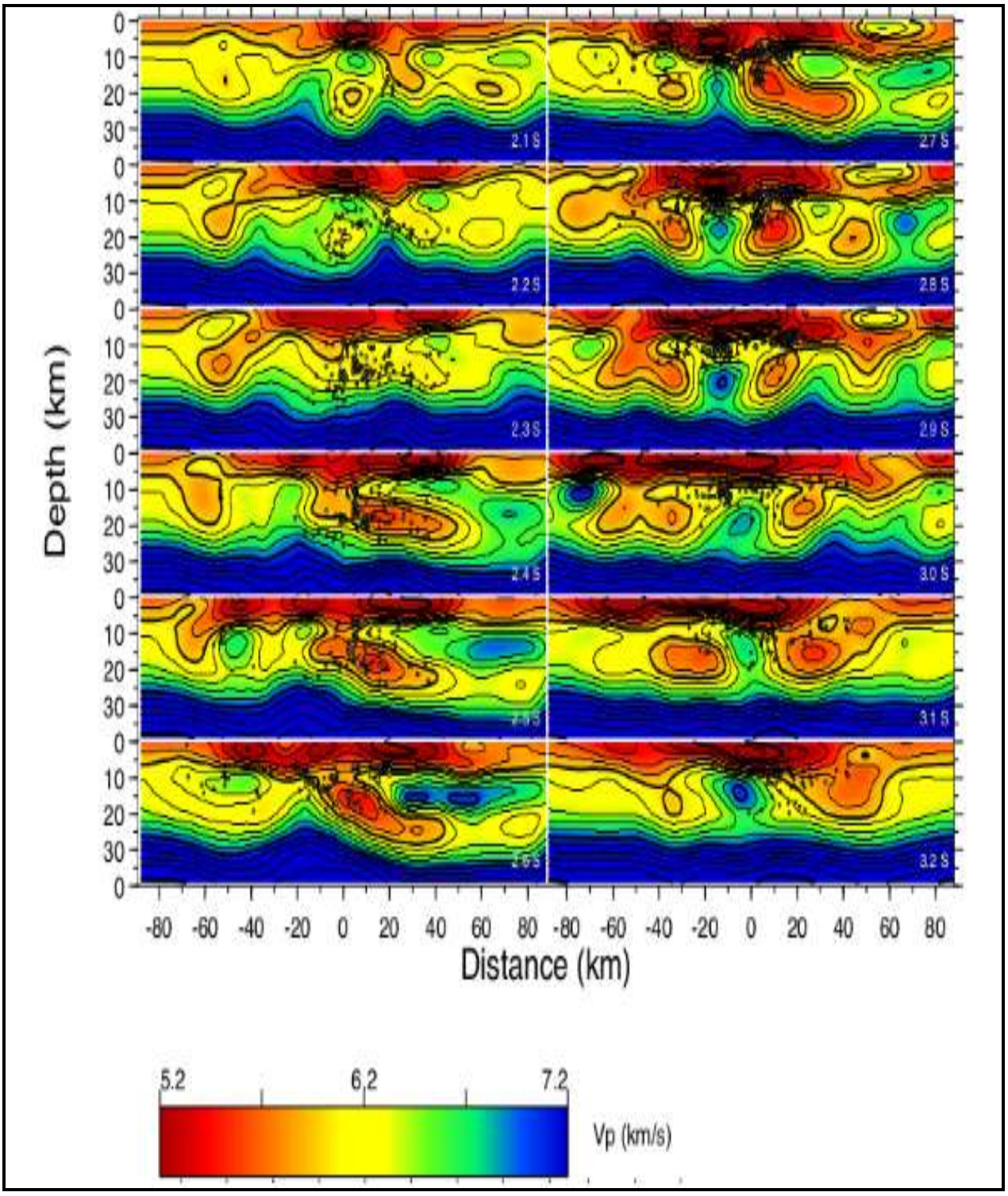

Figure 7.11: Crafti 2D slices from final 3D seismic ambient noise-gravity tomography (Roecker, 2017), at 2.1^0 S, units in kilometers (km), (lateral centre 0 km corresponds with 36^0 E)

The basic deduction of the low V_p including V_s wave-speeds on this top 4-5 kilometers in this middle section of representation should be the wide succession of sediments on this Natron including Magadi fissure basin (Ebinger, 1997 and Birt et al., 1997). Using deductions of surface modification trends (Calais et al., 2008 and Biggs, 2009, 2013) one might anticipate to observe expressions of entire dynamic eruptive activity which controls these zones in depths less than 5 km. Therefore, the lower V_p including V_s in the depths underneath entire fissure basins can be deduced as the proxy for escalated thermal parameters linked to rising molten rock. On the contrary to entire low wave-speeds bodies underneath entire fissure, outstanding elevated wave-speeds tabular bodies alongside entire west part of rift most probably cannot entail molten materials. Instead, huge wave-speeds gradient in entire east part of these features are deduced as manifestation at depth of limiting fault in entire west part of the key fissure, including elevated wave-speeds body as uplifted plus rotated footwall of these regular faults.

Thus, entire low V_p including V_s regions in the upper crust underneath the Magadi rift valley is suggested to stand for small chambers hosting molten lava (15 kilometers deep -50 kilometers horizontally, 20 kilometers deep 5 kilometers horizontally, 15 kilometers deep 30 kilometers horizontally, and 15 kilometers deep 65 kilometers horizontally) beginning at lower crust including upper mantle making its way into earth surface. However, the small pockets themselves cannot be a long-term repository of magma. Instead, they are probably hosting the gaseous "froth" which comprises huge quantity of CO_2, perhaps including some water, at the top of deeper-seated crystal-rich molten rock mush which intermittently refills shallower pocket before extruding the materials. In addition, these CO_2 seems to permeate neighboring media, significantly reducing V_p/V_s at zones in footwall part of limiting faults, consistent with fault regions as channels for molten rock degassing (Lee et al., 2016). The high wave-speeds tabular bodies are believed to be rotated and uplifted footwall crustal slabs derived from the past faulting processes in the Magadi rift valley with contrasting relative velocity.

On comparing figures 7.4, 7.11 and 7.6 slices at latitude 2.1^0 S, shallower crust 0 to 5 kilometers has a relative velocity contrast of between 1.2km/s to about 0.2km/s. The central part of the shallower crust has only one high velocity intrusive body at 35.8^0 E laterally and 5 kilometers deep as in figure 7.4. Similarly, for figure 7.11, there exist three high velocity intrusive bodies

(5.0 kilometers laterally 10.0 kilometers deep, 40.0 kilometers laterally 10.0 kilometers deep and 70.0 kilometers laterally 10.0 kilometers deep). And in the work by Roecker (2017) six low velocity zones (pockets) are evident (63.0 kilometers laterally 19.0 kilometers deep, 25.0 kilometers laterally 17.5 kilometers deep, 5.0 kilometers laterally 4.0 kilometers deep, 5.0 kilometers laterally 20.0 kilometers deep, 35.0 kilometers laterally 4.0 kilometers deep, and -50.0 kilometers laterally 16.0 kilometers deep). The interpretations for the two contrasting features; elevated as well as low speed anomalies in figures 7.4, 7.11 plus 7.6 are high velocity intrusive bodies and small magma pockets respectively. To the right and left of the shallower crust in figures 7.11 plus 7.6, the velocity tends to gradually increase unlike figure 7.4 where velocity tend to be constant into right and left of shallower crust. This is due to possibly reduced resolution caused by inadequate path coverage and constraints. Lower left and right as per figure 7.4, 7.11 and 7.6, the velocity increases to about 7.0 km/s for both cases. However, pockets of low velocity zones are evident in figures 7.11 and 7.6 due to possible magma intrusion from the upper mantle small magma chambers (15 kilometers deep -50 kilometers horizontally, 20 kilometers deep 5 kilometers horizontally, 15 kilometers deep 30 kilometers horizontally, and 15 kilometers deep 65 kilometers horizontally for figure 7.11). The main magma repository is thought to be at about 49.0 kilometers deep (Roecker, et al., 2017) and about 45.0 kilometers deep for this work. Generally, the central part of the shallower crust has remained the same for both figures 7.4, 7.11 and 7.6 where the low velocity begin at the start and pave way for high velocity bodies as depth increases. At depths of between 6 kilometers to about 20 kilometers in figure 7.11, six small magma pockets, (15 kilometers deep -50 kilometers horizontally, 20 kilometers deep 5 kilometers horizontally, 15 kilometers deep 30 kilometers horizontally, and 15 kilometers deep 65 kilometers horizontally), are evident. But, originally, they were absent as per figure 7.4 and also as per Ibs-von Seht et al., 2001 work (slice along profile number 5) replacing old high velocity zones. The major advantage of the results of figure 7.11 is that the inversion had excellent data coverage for the entire section; seismic refraction, wide-angle and gravity data sets, unlike figures 7.4 plus 7.6 which have 30 percent of the sections poorly covered by data. In terms of geological correlation to the subsurface; depth of 0 to 0.1 kilometers with velocities between 0.3 to about 1.3 kilometers per second correlate well with weathered rocks according to Mulumbu (2015) and further interpreted as highly weathered alkali trachytes intercalated with trona beds, silts and clays while high velocity anomaly represent mafic rock intrusion. The rest of

the velocities are interpreted as follows: 4.0 to 5.0 kilometers per second represent halite, trona beds, anhydrite or weathered alkali basalts, 5.2 to 5.5 kilometers per second represent gneissic materials or dolomites, while 5.5 to 6.5 kilometers per second represent fresh alkali basalts or fresh dolomitic materials. Those velocities which are higher than 6.5 kilometers per second but less than 8.2 kilometers per second probably stand for fresh peridotite rocks existing near the upper mantle and closer to asthenosphere where there are high internal magma movements.

The study area has undergone short term crustal structure changes. These changes are very evident from the comparison between figure 7.4 and figure 7.6 for slices in the east west orientation and similarly for figure 7.5 and figure 7.7 for slices in the north south orientation. In the east west orientation, figure 7.4 shows an oval body with high P-wave velocity. This high velocity range from about 6.5kilometers per second to about 8 kilometers per second. This oval body covers from about 35.8^0 E to about 36.4^0 E orientations along the longitude. Along the depth, it covers from about 4 kilometers to about 12 kilometers; about 8 kilometers thick.

According to figure 7.6, the originally oval bodies shown by figure 7.4 broke, changed and deformed into three smaller oval bodies. These oval bodies change in shape from oval shape to sausage-like or globular shape as one moves further south and further north as shown by figure 7.6. They have high P-wave velocity ranging from about 6.5 kilometers per second to about 9 kilometers per second. A central zone is generated in between the three smaller oval bodies with lower P-wave velocity. This lower P-wave velocity range from about 3 kilometers per second to 4 kilometers and is believed to have undergone melting due to the intruding small magma chambers. These changes, as per figure 7.6, cover sections with longitude about 36^0 E to about 36.6^0 E and depth from about 3 kilometers to about 16 kilometers.

In the north south direction, figure 7.5 displays an oval body with high P-wave velocity. This high velocity varies from about 6.5kilometers per second to about 8 kilometers per second. The oval body covers some sections of figure 7.5 from about 2.0^0 S to about 1.8^0 E orientations along the latitude. Along the depth, it covers a section of figure 7.5 from about 4 kilometers to about 12 kilometers; about 8 kilometers in terms of thickness.

According to figure 7.7, the originally oval bodies shown by figure 7.5 broke, changed and deformed into two smaller oval bodies with the top one being almost sausage-like to globular in shape. They have high P-wave velocity ranging from about 6.5 kilometers per second. There exist two oval shaped low velocity zones to the left side of the two high velocity oval bodies. These low P-wave velocity zones range in velocity from about 3 kilometers per second to 4 kilometers and is believed to have undergone melting too due to the intruding small magma chambers. These changes, as per figure 7.7, cover sections with latitude about 2.1^0 S to about 1.8^0 S and depth from about 3 kilometers to about 8 kilometers and about 15 kilometers to about 20 kilometers.

Finally, work by Lee et al. (2016) support the current observations of high internal magmatic movements. This has lead to magma injection into the shallower crust which forms zones (pockets) of smaller magma chambers with low velocities. It replaced some of the old high velocity zones due to partial melting of the country rock when magma injection occurs. Due to such magmatic activities, conduits which transfer CO_2 and other fluids have developed leading to increased CO_2 emissions apart from increased occurrence of hot springs as well as increased seismicity. The CO_2 emissions correlate well with zones of both major and minor faults within the Magadi crust. These faults mainly orient themselves in the general north south direction. However, a few orient themselves in the North West south east direction or north east south west direction (Lee et al., 2016).

9. CONCLUSION AND RECOMMENDATIONS

9.1 CONCLUSION

9.1.1 Seismicity

We strongly support the fact that Magadi is moderately seismically active. Most of the earthquakes occur to the north east of Lake Magadi. The rest of Lake Magadi region (North, North West, West, South West, South, South East and East) have relatively low seismicity.

9.1.2 Hypocenter distribution

The source depths distribution output covered an area whose coordinates include: northing ranging between 2.2^0 S and 1.2^0 S while depth ranges between 0.0 kilometers and 30 kilometers. The various portions of 2D hypocenter slice show distinct depth distribution. In the lower left end of the 2D hypocenters slice, the depth range between 17 kilometers to 11 kilometers. This portion is then followed by the lower right part of the slice which shows slightly deeper source depth of 19.5 kilometers as compared to the lower left. The central, upper right and left have hypocenters with depth range between 0 kilometers to about 10 kilometers deep.

9.1.3 Magadi Crustal Structure evolution

The study confirms the existence of oval shaped high velocity anomaly which later deforms and changes to sausage-like bodies (globules). The position of this high velocity intrusive body is initially shifted both laterally and in depth. Subsequently, three high velocity globules and one low velocity zone become evident after inversion of 2013 and 2014 seismic data sub-set from crafti project. In addition, there are zones which are occupied by constant absolute velocity increasing only with depth. Therefore, it is evident that the Magadi crust has undergone small scale crustal structure changes over a period of four years (1997, 1998, 2013 and 2014) whereby small magmatic injections have intruded into zones which were initial high absolute velocity zones and causing them to become low velocity zones.

9.1.4 Short term Crustal Structure changes

The study area has undergone short term crustal structure changes. These changes are very evident from the comparison between the 2D slices in the east west orientation and similarly for 2D slices in the north south orientation. The originally oval bodies broke, changed and deformed into smaller oval bodies. These shapes change as one moves further south and further north. The oval bodies have high P-wave velocity ranging from about 6.5 kilometers per second to about 8 kilometers per second. A zone is generated in between the smaller oval bodies or on the left side of the smaller oval bodies with lower P-wave velocity. This lower P-wave velocity range from about 3 kilometers per second to 4 kilometers and is believed to have undergone melting due to the intruding small magma chambers.

9.2 Research Limitations

This study entailed comparison of two crustal structures as mentioned before; 1997-1998 and 2013-2014 crustal structures. The existing limitations are due to inadequate data coverage for the years 1999 to 2012. These years could not be adequately covered in terms of data due to the fact that installing adequate permanent or temporary sensors for long periods of time is very costly and such finances were not available. Consequently, the study was based on available data sub sets for 1997, 1998, 2013 and 2014.

9.3 RECOMMENDATIONS

Magadi being an area along the rifting system, with time the area is bound to evolve, continuous scientific studies should be carried out at close intervals. Recommendations are as follows:

To begin with, array coverage in the area is poor and need to be enhanced to enable improved resolution. Secondly, 3D Seismic tomography studies should be carried out continuously at intervals of 15 years in order to understand the crustal structure changes of the study area in terms of velocity structure, lithology and crustal thickness over time. And thirdly, there should be continuous monitoring of events in order to establish the trends so that deductions can be made on magmatic patterns and sequences in the Magadi area.

REFERENCES

Achauer, U., 1991. A study of the Kenya Rift using delay-time tomography analysis and gravity modeling: Tectonophysics, v. 208, p. 197-207

Achauer, U., 1994. New ideas on the Kenya rift based on the inversion of the combined data-set of the 1985 and 1989/90 seismic tomography experiments: Tectonophysics v. 236, p. 305-329.

Aggarwal, Y.P., and Molnar, P., 1971. A micro-earthquake survey in Kenya. Bull. Seism Soc. Am., vol. 61, No. 1, pp. 195-201.

Agnew, D.C., 2002. History of seismology, in International Handbook of Earthquake and Engineering Seismology, Part A, ed. W.H. Lee, San Diego: Academic press, 3-11.

Aki, K., 1974. Three-dimensional seismic-velocity anomalies in the crust and upper-mantle, under the U.S.G.S California seismic array: EOS, Trans. AM. Geophys Union, vol. 56, pp. 1145

Aki, K., and Lee, W.H.K., 1976. Determination of the three-dimensional velocity anomalies under a seismic array using first P arrival times from local earthquakes 1.A homogeneous initial model. J. Geophys. Res. Vol. 81, pp. 4381-4399.

Aki, K., Christoffersson, A., and Husebye, E.S., 1977. Determination of the three-dimensional seismic structure of the lithosphere. J. Geophys. Res. Vol. 82, pp. 277-296.

Akinola, A.K., 2010. Investigation into the Tectonic Lineaments and Thermal Structure of Lake Magadi, southern Kenya Rift using Integrated Geophysical methods, M.S.c Thesis submitted to International institute for Geo-information Science and Earth Observation. ENSCHED, the Netherlands.

Baker, B.H., 1963. Geology of the area south of Magadi, Kenya geol. Surv Rept, 61.

Baker, B.H., 1958. Geology of the Magadi Area, Kenya geol. Surv Rept, 42.

Baker, B.H., and Wohlenberg, J., 1971. Structure and evolution of the Kenya Rift Valley, Nature, 229, 538-542

Baker, B.H., and Mitchell, J.G., 1976.Volcanic stratigraphy and geochronology of Kedong-Olorgesailie area and the evolution of the South Kenya rift. Journal of the Geological Society 132, 467-484.

Baker, B.H., Mohr, P.A., and Williams, L.A.J., 1972. Geology of the Eastern Rift System of Africa, Geol. Soc. Am. Spec. Pap., 136, 1-67.

Bath, M., 1979. Introduction to seismology, 428pp., Birkhauser Verlag. Basel.

Benz, H.M., Zandt, G., and Oppenheimer, D.H., 1992. Lithospheric structure of northern California from teleseismic images of the upper mantle. J. Geophys. Res. Vol. 97, pp. 4791-4807.

Biggs, J., 2013. Surface deformation and stress interactions during the 2007-2010 sequence of earthquake, dyke intrusion and eruption in northern Tanzania, Geophys. J. Int., 195(1), 16-26.

Biggs, J., 2009. InSAR observations of 2007 Tanzania rifting episode reveal mixed fault and dyke extension in an immature continental rift, Geophys. J. Int., 179, 549–558.

Birt, C.S., Maguire, P.K.H., Khan, M.A., Thybo, H., Keller, G.R., and Patel, J., 1997. The influence of pre-existing structures on the evolution of the southern Kenya Rift Valley-evidence from seismic and gravity studies, in Structure and Dynamic Process in the Lithosphere of the Afro-Arabian Rift system, eds Fuchs, K., Altherr, R., Muller, B. & Prodehl, C., Tectonophysics, 278, 211-242

Bishop, T.P., Bube, K.P., Cutler, R.T., Langan, R.T., Love, P.L., Resnick, J.R., Shuey, R.T., Spindler, D.A., and Wyld, H.W., 1985. Tomographic determination of velocity and depth in laterally varying media. Geophysics vol. 50, pp. 903-923.

Bleibinhaus, F., and Gebrande, H., 2006. Crustal structure of the Eastern Alps along the TRANSALP profile from wide-angle seismic tomography. Tectonophysics vol. 414, pp. 51-69.

Bois, P., La Porte, M., Laverge, M., and Thomas, G., 1971. Determination of automatic seismological measurements. Geophys. Prospect. Vol. 19, pp. 42-83.

Bosworth, W., Lambiase, J., and Keisler, R., 1986; A new look at Gregory's Rift: the structural style of continental rifting, EOS, Trans. Am. geophys.Un. vol. 67, pp. 577, 582, 583

Bregman, N.D., Bailey, R.C., and Chapmans, C.H., 1989. Crosshole seismic tomography. Geophysics, vol. 54, pp. 200-215.

Bruneton, M., Pederson, H.A., and Farra, V., 2004. Complex lithospheric structure under the central Baltic Shield from surface wave tomography. J. Geophys. Res. 109, B10303, doi:10.1029/2003JB002947.

Calais, E., D'Oreye, N, Albaric, J., Deschamps, A., Delvaux, D., Deverchere, J., Ebinger, C., Ferdinand, R., W., Kervyn, F., Macheyeki, A.S., Oyen, A., Perrot, J., Saria, E., Smets, B., Stamps, D.S., and Wauthier, C., 2008. Strain accommodation by slow slip and dyking in a youthful continental rift, East Africa. Nature, 456(7223), pp. 783-787.

Chopp, D.L., 2001. Some improvements of the fast marching method: SLAM Journal on Scientific Computing, vol. 23, pp. 230-244.

Clowes, R.M., Zelt, C.A., Amor, J.R., and Ellis, R.M., 1995. Lithospheric structure in the southern Canadian Cordillera from a network of seismic refraction lines. Can. J. Earth Sci. vol. 32, pp. 1485-1513.

Crossley, R., 1979. The Cenozoic stratigraphy and structure of the western part of the Rift valley in southern Kenya. Journal of the Geological Society, vol. 136 (4), pp. 393-405.

Crossley, R., and Knight, R.M., 1981. Volcanism in the western part of the rift valley in southern Kenya, Bulletin of Volcanology 44 (2), 117-128

Darbyshire, F.A., Bjarnason, I.J., White, R.S., and Florenz, O.G., 1998. Crustal structure above the Iceland mantle plume, imaged by the ICEMELT refraction profile. Geophys.J.Int. vol. 135, pp. 1131-1149.

Darbyshire, F.A., and Lebedev, S., 2009. Rayleigh wave phase-velocity heterogeneity and multilayered azimuthal anisotropy of the Superior Craton, Ontario. Geophys. J. Int. vol. 176, pp. 215-234.

De Hoop, M.V., van der Hilst, R.D., and Shen, P., 2006. Wave-equation reflection tomography: annihilators and sensitivity kernels. Geophys. J. int. vol. 167, pp. 1332-1352.

De Kool, M., 2006. a practical grid based method for tracking multiple refraction and reflection phases in 3D heterogeneous media: Geophysical Journal International, vol. 167, pp. 253–270.

Dziewonski, A.M., Hager, B.H., and O'Connell, R.J., 1977. Large-scale heterogeneities in the lower mantle. J. Geophys. Res. Vol. 82, pp. 239-255.

Ebinger, C., 1997. Rifting Archaean lithosphere; the Eyasi-Manyara-Natron rifts, East Africa, J. Geol. Soc. London, vol. 154(6), pp. 947-960.

Farra, V., and Madariaga, R., 1988. Non-linear reflection tomography. Geophys. j. vol. 95, pp. 135-147.

Forsyth, D.W., and Li, A., 2005. Array analysis of two-dimensional variations in surface wave phase velocity and azimuthal anisotropy in the presence of multipathing interference. In: Levander, A., Nolet, G. (Eds), Seismic earth: Array Analysis of Broadband Seismograms. AGU Geophysical Monograph Series, Washington, DC, pp. 81-97.

Friederich, W., and Wielandt, E., 1995. Interpretation of seismic surface waves in regional networks: joint estimation of wavefield geometry and local phase velocity. Method and numerical test. Geophys. J. int. 120, pp. 731-744.

Glahn, A., and Granet, M., 1993. Southern Rhine Graben: small-wavelength tomographic study and implications for the dynamic evolution of the graben. Geophys. J. Int. 113, pp. 399-418.

Graeber, F.M., Houseman, G.A., and Greenhalgh, S.A., 2002. Regional teleseismic tomography of the western Lachlan Orogen and the Newer Volcanic Province, southeast Australia. Geophys.J.Int. 149, pp. 249-266.

Hicks, G., and Pratt, R.G., 2001. Reflection waveform inversion using local descent methods: estimating attenuation and velocity over a gas-sand deposit. Geophysics, vol. 66, pp. 598-612.

Hole,J.A.,1992. Nonlinear-high-resolution-three-dimensional-travel-time-tomography.J. Geophys. Res. 97, PP. 6553-6562.

Hollnack, D., and Stangl, R., 1998. The seismicity related to the southern part of the Kenya Rift. Journal of African Earth Sciences 26(3), PP. 477-495.

Humphreys, E.D., and Clayton, R.W., 1990. Tomographic image of the Southern California Mantle. J. Geophys. Res. Vol. 95, pp. 19725-19746.

Ibs-von Seht, M., Blumenstein, S., Wagner, R., Hollnack, D., and Wohlenberg, J., 2001. Seismicity, seismotectonic and crustal structure of the southern Kenya Rift-new data from Lake Magadi area: Geophysical journal Int., v.146, pp.439-453

Ichangi, D.W., and Maclean, 1991.Archean volcanic facies in the Migori segment, Nyanzian greenstone belt, Kenya: stratigraphy, geochemistry and mineralization. Journal of African earth sciences, vol. 413, pp. 277-290

Jones, B.F., Eugster, H.P., and Rettig, S.L., 1977. Hydrochemistry of the Lake Magadi basin, Kenya: Geochemica et Cosmochimica Acta, v.41, pp.53-72, doi:10.1016[77]90186-7.

Kanasewich, E., Burianyk, M.J.A., Ellis, R.M., White, D.J., Lote, T., Forsyth, D.A., Luetgert, J.A., and Spence, G.D., 1994. Crustal velocity structure of the Omineca Belt, southwestern Canadian Cordillera. J. Geophys. Res. 99, pp. 2653-2670.

Kianji, G.K., 2004. Investigations on Seismicity of Kenya using the University of Nairobi Seismic Network M.S.c Dissertation Pp 77.

Kianji, G.K., 2002, Investigations on the Seismicity distribution in the Magadi area Southern Kenya Rift, Research work, University of Nairobi. P1-5

KRISP, 1985. Large-scale variation in lithospheric structure along the Kenya rift. Nature, 354, pp. 223-227.

KRISP, 1991-94. Large-scale variation in lithospheric structure along and across the Kenya rift. Nature, 354, pp. 223-227.

Korenaga, J., Holbrook, W.S., Kent, G.M., Kelemen, R.S., Detrick, R.S., Larsen, H.C., Hopper, J.R., and Dahl-Jensen, T., 2000. Crustal structure of the southeast Greenland margin from joint refraction and reflection tomography. J. Geophys. Res. 105, v. 21, pp. 591-614.

Kuria, Z.N. 2011. Seismotectonics of active faults; Magadi fault system, southern Kenya Rift. PhD Thesis, University of Twente, Netherlands.

Kuria, Z.N., Woldai, T., Barongo, J.O., and van der Meer F.D. 2010. Active fault segments as potential earthquake sources: inferences from integrated geophysical mapping of the Magadi fault system, southern Kenya Rift. Journal of Africa Earth Sciences, v. 57, pp. 345-359.

Lambiase, J.J. and Bosworth, W., 1995. Structural controls and sedimentation in continental rift, Geological society, London, special publication v.80

Lee Gall, B., Nonnotte, P., Rolet, J., Benoit, M., Guillou, H., Mousseau-Nonnotte, M., Albaric, J., and Deverchere, J., 2008. Rift propagation at craton margin: distribution of faulting and volcanism in the North Tanzanian Divergence (East Africa) during Neogene times. Tectonophysics, v. 448 (1-4), pp. 1-19.

Lee Gall, B., Tiercelin, J.J., Richert, J.P., Gente, P., Sturchio, N. C., Stead, D., and Le Turdu, C., 2000. A morphotectonic study of an extensional fault zone in a magma-rich rift: the Baringo Trachyte Fault System, central Kenya Rift. Tectonophysics, v. 320, pp. 87-106.

Lee, H., Kattenhorn, S.A., Mana, S., Turrin, B.D., Fischer, T.P., Kianji, K.G., Dindi, E., and Stamps, D.S., 2016. Tectonic degassing of mantle-derived CO_2 along faults in the East African Rift, Nature Geoscience, v. 9, pp. 145–149.

Lerner, E.K.L., and Cengage, B.W.L.G., 2003. Faults and Structures, World of earth science

Li, A., and Burke, K., 2006. Upper mantle structure of southern Africa from Rayleigh wave tomography. J. Geophys. Res. 111, doi:10.1029/2006JB004321.

Louden, K.E., and Fan, J., 1998. Crustal structures of Grenville, Makkovik, and southern Nain provinces along the Lithoprobe ECSOOT Transect: regional seismic refraction and gravity models and their tectonic implications. Can. J. Earth Sci. v. 35, pp. 583-601.

Maguire, P.K.H., and Long, R.E., 1976. The structure of Western flank of Gregory rift (Kenya). Part1. The crust: Geophysical Journal of the Royal Astronomical society, v.44, pp.661-675.

Matheson, F.J., 1966. Geology of the Kajiado area, Kenya geol. Surv Rept, No. 70, pp. 51.

Mathu, E.M, and Nyambok, I.O. 1993. A re-evaluation of the geology and tectonics of the major granitoid plutons around Kakamega town. In N. Opiyo (Ed.). 5th Conference on the Geology of Kenya. Geological Society of Kenya, Nairobi, Kenya, pp. 63-68.

Mathu, E.M., and Davis, T.C., 1996. Geology and the Environment in Kenya. Journal of African Earth Sciences, Vol. 23: pp 511-539.

McCaughey, M., and Singh, S.C., 1997. Simultaneous velocity and interface tomography of normal-incidence and wide-aperture seismic traveltime data. Geophys.J.Int. v. 131, pp. 87-99.

McMechan, G.A., 1983. Seismic tomography in boreholes. Geophys.J.Royal Astr.Soc. v. 74, pp. 601-612.

McMechan, G.A., 1987. Cross-hole tomography for strongly variable media with applications to scale model data. Bull.Seismol.Soc.Am. vol. 77, pp. 1945-1960.

Mjelde, R., Digranes, P., Shimamura, H., Shiobara, H., Kodaira, S., Brekke, H., Egebjerg, T., Sorenes, N., and Thorbjornsen, S., 1998. Crustal structure of the northern part of the Voring Basin, mid-Norway margin, from wide-angle seismic and gravity data. Tectonophysics, v. 293, pp. 175-205.

Morgan, R.P.L., Barton, P.J., Warner, M., Morgan, J., Price, C., and Jones, K., 2000. Lithospheric structure north of Scotland. I.P-wave modelling, deep reflection profiles and gravity. Geophys.J.Int. vol. 142, pp. 716-736.

Morozov, I.B., Smithson, S.B., Hollister, L.S., and Diebold, J.B., 1998. Wide-angle seismic imaging across accreted terranes, southeastern Alaska and western British Columbia. Tectonophysics, vol. 299, pp. 281-296.

Muirhead, J.D., Kattenhorn, S.A., Lee, H., Mana, S., Turrin, B.D., Fischer, T.P., Kianji, K.G., Dindi, E., and Stamps, D.S., 2016. Evolution of upper crustal faulting assisted by magmatic volatile release during early-stage continental rift development in the East African Rift. The Geological Society of America.

Mulumbu Elly B., 2015. 2D controlled source seismic mapping of the Low Velocity Layer (LVL) in Magadi Basin, Kenya.

Nicholas, D.E., 1996. Maximum-energy travel-times calculated in the seismic frequency band: Geophysics, vol 61, pp. 253-263.

Ngecu, W. M., 1993. Stratigraphy and sedimentology of the Archean Greenstone Belt of Western Kenya. Paper published in the Proceedings of the 5th Conference on the Geology of Kenya.

Nyambok, I.O. 1992. Magadi: Geology of the Kedong Valley. In Kenya from space.CREDU, France. East African Educational Publisher, Nairobi. Pp. 140-143.

Oncescu, M.C., Burlacu, V., Anghel, M., and Smalbergher, V., 1984. Three-dimensional P-wave velocity image under the Carpathian Arc. Tectono-physics, v. 106, pp. 305-319.

Officer, C.B., 1958. Introduction to the theory of sound transmission: McGraw-Hill Book Co.

Opiyo, A.N., and Muhongo, S. 1999. Geology and mineral resources of east Africa: Journal of Africa Earth Sciences Vol.29, Issue 2.pp281-282.

Ottemoller, L. 2008-11, SEISAN: the earthquake analysis software. For WINDOWS, SOLARIS, LINUX and MACOSX Version 8.2, Department of Earth Science, University of Bergen, Norway

Pedersen, H.A., Coutant, O., Deschamps, A., Soulage, M., and Cotte, N., 2003. Measuring surface wave phase velocities beneath small broadband arrays: test of an improved algorithm and application to the french alps. Geophys. J. Int. vol. 154, pp. 903-912.

Plomerova, J., Babuska, V., Kozlovskaya, E., Vecsey, L., and Hyvonen, 2008. Seismic anistropy: a key to resolve fabrics of mantle lithosphere of Fennoscandia. Tectonophysics, vol. 462, pp. 125-136.

Podvin, P., and Lecomte, I., 1991. finite-difference computation of travel-times for velocity-depth models with strong velocity contrast across layer boundaries-a massively parallel approach: Geophys.J.Int., v. 105, pp. 271-284.

Popovici, A.M., and Sethian, J.A., 2002. 3-D imaging using higher order fast marching travel-times: Geophysics, v. 67, pp. 604-609.

Pratt, R.G., and Shipp, R.M., 1999. Seismic waveform inversion in the frequency domain. Part 2. Fault delineation in sediments using crosshole data. Geophysics, vol. 64, pp. 902-914.

Pratt, R.G., and Goulty, N.R., 1991. Combining wave-equation imaging with traveltime tomography to form high-resolution images from cross-hole data. Geophysics, vol. 56, pp. 208-224.

Pratt, R.G., and Worthington, M.H., 1988. The application of diffraction tomography to cross-hole seismic data. Geophysics, vol. 53, pp. 1284-1294.

Prodehl, C., Fuchs, K., and Mechie, J., 1997. Seismic-refraction studies of the Afro-Arabian rift system-a brief review. Tectonophysics, vol. 278 (1-4), pp. 1-13.

Prodehl, C., Jacob, A.W.B., Thybo, H., Dindi, E., and Stangl, R., 1994. Crustal structure on the northeastern flank of the Kenya rift. Tectonophysics, vol. 236 (1-4), pp. 271-290.

Rawlinson, N., and Kennett, B.L.N., 2008. Teleseismic tomography of the upper mantle beneath the southern Lachan orogen. Aust. Phys. Earth Planet. Inter. Vol. 167, pp. 84-97.

Rawlinson, N., Reading, A.M., and Kennett, B.L.N., 2006b, Lithospheric structure of Tasmania from a novel form of teleseismic tomography. J. Geophys. Res., 111, B02301 doi:10.1029/2005JB003803.

Rawlinson, N., and Urvoy, M., 2006. Simultaneous inversion of active and passive source datasets for 3-D seismic structure with application to Tasmania. Geophys. Res. Lett. 33, doi:10.1029/2006GL028105.

Rawlinson, N., and Sambridge, M., 2004b, multiple reflection and transmission phases in complex layered media using multistage fast marching method: Geophysics, v. 69, p. 1338-1350.

Rawlinson, N., and Sambridge, M., 2004a, Wave-front evolution in strongly heterogeneous layered media using the fast marching method: Geophysical Journal International, v. 156, pp. 631-647.

Rawlinson, N., Houseman, G.A., Collins, C.D.N., and Drummond, B.J., 2001, New evidence of Tasmania's tectonic history from a novel seismic experiment, Geophys. Res. Lett., v. 28, p. 3337–3340.

Riahi, M.A., and Juhlin, C., 1994. 3-D interpretation of reflected arrival times by finite-difference techniques. Geophysics, vol. 59, pp. 844-849.

Roecker, S., 2017. Subsurface Images of the Eastern Rift, Africa, from Joint Inversion of Body waves, Surface Waves, and Gravity, Investigating the Role of Fluids in Early-Stage Continental Rifting, Science, 20117(11-26) pp. 11-26,

Saltzer, R.L., and Humphreys, E.D., 1997. Upper mantle P wave velocity structure of the eastern Snake River plain and its relationship to geodynamic models of the region. J. Geophys. Res. V. 102, pp. 11829-11841.

Sethian, J.A., and Popovici, A.M., 1999. 3-D travel-time computation using the fast marching method: Geophysics, vol. 64, pp. 516-523.

Sethian, J.A., 1999. Level set methods and fast marching methods: Cambridge University Press.

Smith, M., 1994. Stratigraphic and structural constraints on mechanisms of active rifting in the Gregory Rift, Kenya, in Crustal and Upper Mantle Structure of the Kenya Rift, eds Prodehl, C., Keller, G.R. & Khan, M.A., Tectonophysics, vol. 236, pp. 3-22.

Smith, M., and Mosley, P., 1993. Crustal heterogeneity and basement influence on the development of the Kenya Rift, East Africa, Tectonics, vol. 12 (issue 2), pp. 591-606

Staples, R.K., White, R.S., Brandsdottir, Menke, W., Maguire, P.K.H., and McBride, J.H., 1997. Faroe-Iceland Ridge experiment. 1. Crustal structure of northern Iceland . J. Geopyys. Res. Vol. 102, pp. 7849-7866.

Song, Z.M., Williamson, P.R., and Pratt, R.G., 1995. Frequency-domain acoustic-wave modelling and inversion of cross-hole data. Part II. Inversion method, synthetic experiments and real-data results. Geophysics, vol. 60, pp. 796-809.

Steck, L.K., Thurber, C.H., Fehler, M., Lutter, W.J., Roberts, P.M., Baldridge, W.S., Stafford, D.G., and Sessions, R., 1998. Crust and upper mantle P wave velocity structure beneath Valles caldera, New Mexico: results from the Jemez teleseismic tomography experiment J. geophys. Res. 103, 24301-24320.

Tongue, J.A., Maguire, P.K.H., and Young, P.A.V., 1994. An earthquake study in the Lake Baringo basin of the central Kenya Rift, eds prodehl, C., Keller, G.R. & Khan, M.A., Tectonophysics, v. 236, pp. 151-164.

Tongue, J.A., Maguire, P.K.H., and Young, P.A.V., 1992. Seismicity distribution from temporary earthquake recording networks in Kenya, Tectonophysics, vol. 204, pp. 71-79

Tongue, J.A., 1990. Tomographic study of local earthquake data from the Lake Bogoria region of the Kenya Rift Valley. Depart of Geology, University of Leicester, Leicester LEI7RH, UK.

VanDecar, J.C., and Snieder, R., 1994. Obtaining smooth solutions to large, linear, inverse problems. Geophysics, vol. 59, pp. 818-829.

Vidale, J., 1988. Finite-difference calculation of travel-times: Bull.Seis.Soc.Am., vol. 78, pp. 2026-2076.

Wang, B., and Braile, L.W., 1996. Simultaneous inversion of reflection and refraction seismic data and application field data from the northern Rio Grande rift. Geophys.J.Int. v. 125, pp. 443-458.

Wang, Y., and Pratt, R.G., 1997. Sensitivities of seismic travel-times and amplitudes in reflection tomography. Geophys.J.int. vol. 131, pp. 618-642.

Wang, Y., White, R.E., and Pratt, R.G., 2000. Seismic amplitude inversion for interface geometry: practical approach for application. Geophys.J.Int. vol. 142, pp. 162-172.

Weeraratne, D.S., Forsyth, D.W., Fischer, K.M., and Nyblade, A.A., 2003. Evidence for an upper mantle plume beneath the Tanzanian craton from rayleigh wave tomography. J. Geophys. Res. 108, doi:10.1029/2001JB001225.

Zelt, B.C., Ellis, R.M., Zelt, C.A., Hyndman, R.D., Lowe, C., Spence, G.D., and Fisher, M.A., 2001. Three-dimensional crustal velocity structure beneath the Strait of Georgia, British Columbia. Geophys.J.Int. vol. 144, pp. 695-712.

Zelt, C.A., Ellis, R.M., and Zelt, B.C., 2006. 3-D structure across the Tintina strike-slip fault, northern Canadian Cordillera, from seismic refraction and reflection tomography. Geophys.J.Int. vol. 167, pp. 1292-1308.

Zelt, C.A., and White, D.J., 1995. Crustal structure and tectonics of the southeastern Canadian Cordillera. J. Geophys. Res. 100, 24255-24273.

ftp://quake.geo.berkeley.edu/outgoing/installation/bi_guide.ps.gz as at 1/12/14

http://www.google/magadi Kenya images as at 21/7/2014

http://www.google/magadi/kenya/images as at 21/7/2014